



ScuDo
Scuola di Dottorato ~ Doctoral School
WHAT YOU ARE, TAKES YOU FAR



Doctoral Dissertation
Doctoral Program in Metrology (32nd cycle)

Novel devices and methods for quantum resistance and impedance metrology

Martina Marzano

* * * * *

Supervisors

Massimo Ortolano, Supervisor
Luca Callegaro, Co-supervisor

Doctoral Examination Committee:

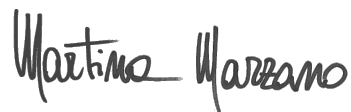
Dr. Blaise Jeanneret, Referee, Federal Institute of Metrology
Prof. Marian Kampik, Referee, Silesian Technical University
Dr. Yolanda Álvarez Sanmamed, Centro Español de Metrología
Dr. Davide Calonico, Istituto Nazionale di Ricerca Metrologica
Dr. Emanuele Enrico, Istituto Nazionale di Ricerca Metrologica

Politecnico di Torino
9 January 2020

This thesis is licensed under a Creative Commons License, Attribution - Noncommercial-NoDerivative Works 4.0 International: see www.creativecommons.org. The text may be reproduced for non-commercial purposes, provided that credit is given to the original author.

I hereby declare that the contents and organisation of this dissertation constitute my own original work and does not compromise in any way the rights of third parties, including those relating to the security of personal data.

Commercial equipment, instruments, and materials are identified in this dissertation in order to specify the experimental procedure adequately. Such identification is not intended to imply recommendation or endorsement by the author or by the host institutions, nor is it intended to imply that the materials or equipment identified are necessarily the best available for the purpose.

A handwritten signature in black ink that reads "Martina Marzano". The script is cursive and fluid, with the first name and last name clearly distinguishable.

Martina Marzano
Turin, December 20, 2019

Acknowledgements

I am particularly thankful to my supervisor, Massimo Ortolano, for the planning of my work during these years and for supporting me continuously. Moreover, I want to thank him for being a mentor and a guide in the scientific research.

I am also grateful to my co-supervisor, Luca Callegaro, for all the fruitful discussions. Thanks to Alessandro Cultrera, Vincenzo D'Elia and Mai Tran for their collaboration during the years of research in INRiM.

I would like to offer my special acknowledgements to the NIST colleagues I met in Gaithersburg: Mattias Kruskopf, Alireza Panna, Shamith Payagaya, Charles Perera, Dinesh Patel, Albert Rigosi, Hanbyul Jin and Randolph Elmquist.

Finally, I would like to thank Daniele, Silvia and all my loved ones to support me everyday in this journey.

Preface

This dissertation describes the work I performed in the laboratories of three National Metrology Institutes: at the Istituto Nazionale di Ricerca Metrologica (INRIM), Turin, Italy, and, as a guest researcher, at the National Metrology Institute of Japan (NMIJ), National Institute of Advanced Industrial Science and Technology (AIST), Tsukuba, Japan and at the National Institute of Standards and Technology (NIST), Gaithersburg, MD, US.

The thesis activities were mainly completed in the Laboratory of Impedance Metrology of the Quantum Metrology and Nano Technologies Division of INRIM.

In January 2017, I visited the NMIJ for a collaboration on the application of circuit analysis methods to quantum Hall array resistance standards (QHARS).

From 1 November 2018 to 31 April 2019, I visited the Fundamental Electrical Measurements group of the Quantum Measurement Division of the Physical Measurement Laboratory at NIST, working in particular in the Resistance Metrology Laboratory and in the Graphene Laboratory.

Chapter 1 of this dissertation shortly introduces the fundamentals of resistance and impedance metrology by defining the quantities of interest and their units in the International System of Units (SI). In particular, I discuss the definition and the realization of the units ohm, farad and henry from the quantum Hall effect (QHE) and describe the most common QHE devices employed in resistance and impedance metrology. I also present a short review of the main measurement techniques used to calibrate resistance and impedance standards in the SI.

Chapter 2 focuses on the electrical modelling of circuits with QHE elements, both with algebraic methods and with the SPICE circuit simulator. After an introduction to the modelling of a QHE element, I present a general method, interesting for metrological applications, to model the errors of complex measuring circuits. I also describe a SPICE macro-model of a QHE element that can be employed to perform SPICE analyses of circuits with QHE elements. This chapter includes also an example of application of the previously described QHE circuit analysis method. I developed the `QHARSmachine`, an implementation of the method in the Wolfram Mathematica environment. From experimental data and with a Monte Carlo evaluation of the uncertainty, the application estimates the error of a QHARS. During my stay at the NMIJ, I applied this method to a $1\text{ M}\Omega$ QHARS fabricated by

the Japanese metrology institute. This work is published in [1]. This method has been also applied to other networks. The SPICE analysis has been applied to pn-junction graphene QHARS by means of SPICE QHE device macro-models. Devices of different nominal resistance values were fabricated at NIST. The SPICE simulations provided forecasts of the final values of the resistance measurements in different configurations, thus reducing the measurement time and simplifying the measurement procedure. During the six months as guest researcher at NIST, I thus contributed to the design and realization of the measurements of these devices, whose results have been reported in [2]. Lastly, SPICE QHE macro-models have been employed to simulate the effect in the AC regime of the stray impedances of a QHE device interconnected to a measuring system. Devices with different designs were investigated, to understand the best configurations to minimise the stray parameters effect. Some of these devices were then fabricated at NIST. These two last applications are ongoing work and are not described in this dissertation.

Chapter 3 presents the design and implementation of a DC quantum Hall effect Kelvin resistance bridge for the direct calibration of four-terminal resistance standards operating at room temperature. I presented the bridge idea in [3] and I designed and performed a validation experiment in the NIST laboratories. The bridge is implemented with a graphene QHARS fabricated at NIST. The calibration result is compared with that obtained from the NIST resistance scale. The relative deviation between the two methods is of about few parts in 10^9 with a standard uncertainty of comparable magnitude. The results of the experiment are presented in [4].

Chapter 4 describes a four terminal-pair fully-digital impedance bridge operating in a 1 : 1 ratio configuration for the direct calibration of an 8 nF standard capacitor against a quantum Hall resistance standard at 1541 Hz. The evaluated uncertainty is of about 2×10^{-7} . This bridge is being implemented at INRIM in the framework of the project EMPIR 18SIB07 GIQS, *Graphene impedance quantum standard*, as a possible new Italian traceability chain of the farad. I present here the preliminary set-up, validation results and evaluation of the uncertainty sources. The final validation results and uncertainty budget will be reported in [5].

Contents

Preface	v
1 Introduction	1
1.1 Fundamentals of resistance and impedance metrology	1
1.1.1 Two-terminal elements	2
1.1.2 Multi-terminal elements	4
1.1.3 Multi-port elements	7
1.2 The International System of Units	11
1.2.1 Resistance and impedance units in the SI	12
1.3 Realization of the units from the quantum Hall effect	15
1.3.1 QHE devices	17
1.3.2 Quantum Hall Array Resistance Standards	24
1.3.3 Quantum Hall effect in the AC regime	25
1.4 Resistance and impedance calibration techniques in the SI	26
1.4.1 Resistance calibrations	28
1.4.2 Impedance calibrations	29
2 QHE circuit modelling	35
2.1 Circuit models of QHE elements	36
2.1.1 Ideal QHE device	36
2.1.2 Contact resistances	37
2.2 Analysis of a QHARS	38
2.3 Application: the QHARSmachine	39
2.3.1 Converter	40
2.3.2 Solver	40
2.3.3 Example: analysis of a 1 M Ω QHARS	42
2.3.4 Identification of the stray parameters	43
2.3.5 Results	49
2.4 Remarks	51
2.5 SPICE macro-model of a QHE element	51

3	Quantum Hall Kelvin Bridge	55
3.1	Motivations	56
3.2	Traditional Kelvin bridge	56
3.3	Quantum Hall Kelvin bridge: theory of operation	58
3.4	Bridge-on-a-chip: device description and characterization	59
3.5	Experimental setup	64
3.6	Error sources	66
3.6.1	Bias and drift	67
3.6.2	Voltmeter error	67
3.6.3	Lead and contact resistances	68
3.6.4	Leakage resistances	70
3.6.5	Imperfect quantization	72
3.7	Measurement procedure and model	73
3.8	Results	73
3.9	Further developments	79
4	Four-terminal-pair fully-digital impedance bridge	81
4.1	Principle of operation	82
4.2	Implementation	86
4.3	Uncertainty sources and budget	90
4.3.1	Crosstalk	90
4.3.2	High and low balances	91
4.3.3	Injection	91
4.3.4	Measurement model and uncertainty budget	92
4.4	Comparison with a transformer ratio bridge	93
4.4.1	Experimental set-up	93
4.4.2	Results	94
5	Conclusions	97
A	Mathematica notebooks	101
A.1	QHARSmachine	101
A.1.1	Initialization	101
A.1.2	Converter	102
A.1.3	Import of the stray parameters spreadsheet	102
A.1.4	Solver	103
A.2	Quantum Hall Kelvin bridge analysis	104
A.2.1	Initialization	104
A.2.2	Converter	105
A.2.3	Solver	105
	Bibliography	109

Chapter 1

Introduction

This chapter introduces the basics of electrical resistance and impedance metrology in the International System of Units (SI). Section 1.1 defines the concepts of resistance and impedance, and their role in the area of electrical measurements. Section 1.2 briefly reviews the evolution of electrical units until the most recent 2018 revision to the SI. Section 1.3 describes the phenomenology of the quantum Hall effect (QHE) and its application to the realization of resistance and impedance units in the SI. In particular, section 1.3.1 presents the main types of QHE devices employed in resistance and impedance metrology. Finally, section 1.4 explores the measurement techniques commonly adopted to calibrate resistance and impedance standards.

1.1 Fundamentals of resistance and impedance metrology

Resistance and impedance measurements play an important role in the spectrum of electrical measurements applied to different fields of science. For example, accurate impedance measurements are employed to characterize biological tissues, electromechanical appliances, electronic components or material samples [6]. Furthermore, electrical resistance and impedance are often the output quantities of sensors and transducers, adopted in all kind of scientific and engineering disciplines, such as medicine, biology, geology, food industry and material science (see [7] and references therein). Resistance and impedance metrology are the disciplines responsible for the realization in DC and AC of the units of resistance and impedance, ohm (Ω), farad (F) and henry (H), and of their scales.

Performing impedance measurements is challenging because stray resistances and impedances can affect the measurement. These result from the geometrical parameters of the system and from the interactions between different parts of the

circuit causing mutual stray impedances. Therefore, accurate impedance measurements require careful wiring techniques and a proper definition of the measurand, that is, the quantity of interest.

The main purpose of the impedance definition is to identify a closed surface, the measurement terminals, and a set of electrical boundary conditions to reject any stray effect from the connections and from the electromagnetic properties of the environment. Once these conditions have been fixed, the measurement result no longer depends on the environment and its changes. The definitions of resistance and impedance can be classified in two categories: *n-terminal* definitions and *n-terminal-pair* (or *n-port*) definitions.

Here, I only mention the definitions that are useful for the understanding of the topics covered in this dissertation.

1.1.1 Two-terminal elements

A *two-terminal element*, or *two-terminal network*, models a system where it is possible to define at any time t a voltage $v(t)$ across two terminals and a current $i(t)$ entering one terminal and exiting the other one (figure 1.1). Here, and in the following, we only consider *linear* and *time-invariant* elements [8].

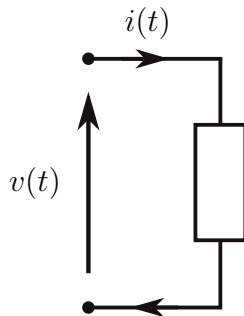


Figure 1.1: Two-terminal circuit element or two-terminal network, with associated current and voltage directions: $v(t)$ is the voltage across the two terminals; $i(t)$ is the current flowing from one terminal to the other.

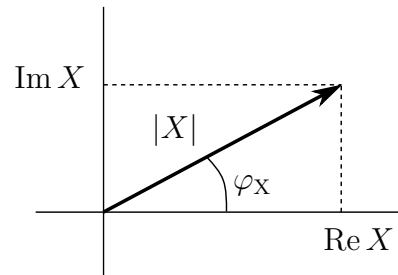


Figure 1.2: Graphical representation of a phasor X in the complex plane. $\text{Re } X$ and $\text{Im } X$ are its Cartesian coordinates, real and imaginary part, respectively; $|X|$ and φ_X are its polar coordinates, amplitude and phase, respectively.

An element obeying the Ohm's law $v(t) = Ri(t)$ is a *resistor*, and R is its *resistance*. Equivalently, Ohm's law can be represented as $i(t) = Gv(t)$, and $G = R^{-1}$ is the *conductance* of the element. The condition $G = 0$ defines an *open circuit*, such that $i(t) = 0$; conversely, $R = 0$ defines a *short circuit*, such that

$v(t) = 0$. Since resistors dissipate instantaneously the absorbed electric power, they are perfect dissipative elements.

An element satisfying the relation $q(t) = Cv(t)$ is an *ideal (pure) capacitor* with stored electric charge $q(t) = \int_{-\infty}^t i(\tau) d\tau$, and C is its *capacitance*.

An element satisfying the relation $\Phi(t) = Li(t)$ is an *ideal (pure) inductor* with magnetic flux linkage $\Phi(t) = \int_{-\infty}^t v(\tau) d\tau$, and L is its *inductance*.

Since capacitors and inductors do not dissipate the absorbed electric power, they are lossless elements. The energy is stored as electrostatic and magnetic energy, respectively.

According to the SI, the ohm (Ω) is the unit of resistance, the farad (F) is the unit of capacitance and the henry (H) is the unit of inductance (section 1.2.1).

In general, in the AC regime, the analysis of circuits composed of these elements would require the solution of systems of differential equations. The sinusoidal steady-state analysis is often employed to simplify the solution of electric circuits composed of linear and time-invariant elements driven by sinusoidal voltage or current sources at a fixed frequency f . We define a generic sinusoidal signal¹

$$x(t) = X_{\max} \cos(\omega t + \varphi) = \operatorname{Re} X_{\max} e^{j(\omega t + \varphi)}, \quad (1.1)$$

where $x(t)$ can be, for instance, q , v , or i , X_{\max} is the positive maximum amplitude, $\omega = 2\pi f$ is the angular frequency and φ is the phase. We can associate to this signal the *phasor*

$$X = X_{\max} e^{j\varphi}. \quad (1.2)$$

If ω is known, X uniquely identifies the signal $x(t) = \operatorname{Re} X e^{j\omega t}$ and viceversa. The phasor X can be graphically represented as a vector in the complex plane, as shown in figure 1.2, and can be identified either by its Cartesian coordinates, the real part $\operatorname{Re} X$ and the imaginary part $\operatorname{Im} X$, or by its polar coordinates, the amplitude $|X|$ and the phase φ_X . By means of phasors, systems of differential equations in sinusoidal steady-state are transformed into systems of complex linear algebraic equations. Moreover, the sinusoidal steady-state regime can be easily implemented with electronic signal generators and phasors can be accurately measured with vector instruments.

If a linear time-invariant two-terminal element is driven by a sinusoidal current signal

$$i(t) = I_{\max} \cos(\omega t + \varphi_I), \quad (1.3)$$

with associated phasor

$$I = I_{\max} e^{j\varphi_I}, \quad (1.4)$$

¹We adopt here, and in the following, the engineering convention that complex exponential signals rotate counterclockwise.

the voltage $v(t)$ across the element is

$$v(t) = V_{\max} \cos(\omega t + \varphi_V), \quad (1.5)$$

with associated phasor

$$V = V_{\max} e^{j\varphi_V}. \quad (1.6)$$

The impedance $Z(\omega)$ of a two-terminal element is defined as the ratio between the phasors V and I ,

$$Z(\omega) = \frac{V}{I} = R + jX, \quad (1.7)$$

where $R = \operatorname{Re} Z$ is the *resistance* and $X = \operatorname{Im} Z$ is the *reactance*. Alternatively, if the driving signal is a sinusoidal voltage source $v(t)$ and a sinusoidal current $i(t)$ crosses the element, it is possible to define the *admittance* $Y(\omega)$ as the ratio of the phasors I and V associated to the signals $i(t)$ and $v(t)$,

$$Y(\omega) = \frac{I}{V} = \frac{1}{Z(\omega)} = G + jB. \quad (1.8)$$

The quantity $G = \operatorname{Re} Y$ is the *conductance* and $B = \operatorname{Im} Y$ is the *susceptance*. According to the SI, the unit of impedance is the ohm (Ω) and the unit of admittance is the siemens ($S = \Omega^{-1}$).

From the constitutive equations it can be seen that for an ideal resistor, impedance and admittance are real quantities independent of frequency, whereas for a pure capacitor or inductor, impedance and admittance are imaginary quantities which depend on the frequency (table 1.1)

Table 1.1: Impedance and admittance of pure two-terminal elements.

Element	Symbol	Impedance Z	Admittance Y
Resistor	R	R	$\frac{1}{R}$
Capacitor	C	$-j\frac{1}{\omega C}$	$j\omega C$
Inductor	L	$j\omega L$	$-j\frac{1}{\omega L}$

Any arbitrary passive impedance, not purely real or imaginary, can be modelled at a fixed frequency as a series or parallel combination of a resistor and either a capacitor or an inductor.

1.1.2 Multi-terminal elements

An electrical network with m accessible terminals is called an m -terminal element. Consider the linear and time-invariant multi-terminal element \mathcal{N} of figure 1.3, with current J_k flowing into the generic terminal k at voltage E_k with

respect to an arbitrary reference node² O . We denote the voltage difference between two terminals as $V_{jk} = E_j - E_k$. Kirchhoff's current and voltage laws for an m -terminal element, $\sum_{k=1}^m J_k = 0$ and $V_{12} + V_{23} + \dots + V_{m1} = 0$, imply that $m - 1$ voltages and currents can be independently specified. Further constraints are then imposed by the element's behaviour. With reference to figure 1.4, the *four-terminal impedance*, or *transimpedance*, $Z_{ij,kl}$ is defined as the ratio between the open-circuit voltage phasor V_{ij} between terminals i and j and the current phasor I_{kl} flowing from terminal k to terminal l , when all other terminals are open-circuited [9]:

$$Z_{ij,kl} = \left. \frac{V_{ij}}{I_{kl}} \right|_{I_n=0; n \neq k,l}. \quad (1.9)$$

An impedance $Z_{il,kl}$, with one terminal in common, is a *three-terminal impedance*; an impedance $Z_{kl,kl}$ represents the already defined *two-terminal impedance*.

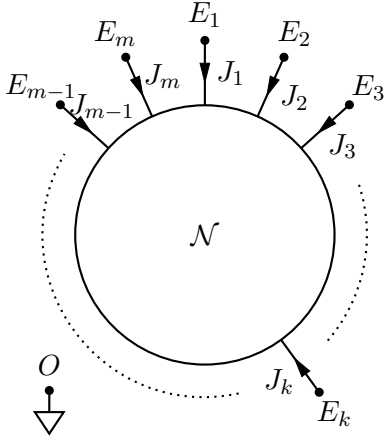


Figure 1.3: Multi-terminal element \mathcal{N} . The terminal voltages E_i are measured with respect to O , an arbitrary reference node; the terminal currents J_i flowing into \mathcal{N} are positive. Reproduced with permission from [9] ©IOP Publishing. All rights reserved.

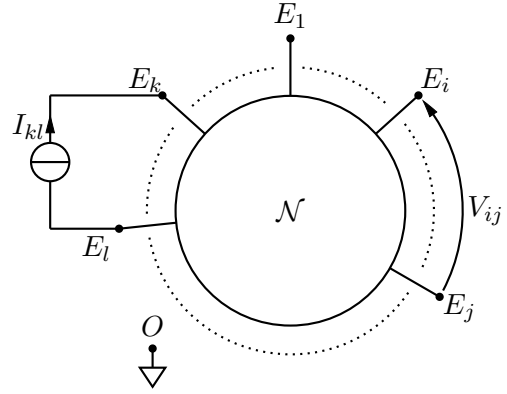


Figure 1.4: Definition of four-terminal impedances of a multi-terminal element \mathcal{N} . The four-terminal impedance is obtained by considering the current I_{kl} flowing between the terminals k and l and the voltage V_{ij} across the terminals i and j . Reproduced with permission from [9] ©IOP Publishing. All rights reserved.

Sometimes the terminals of an m -terminal element, with m even, can be grouped into $n = m/2$ ordered pairs called *terminal-pair* or *ports*, so that the current entering into the first terminal of the pair is equal to the current exiting from the

²Here and in the following, voltages and currents are considered as voltage and current phasors.

second one [6]. For an n -port element, for each port k , we define the voltage V_k as the difference between the voltages of the two terminals of the pair, and I_k as the inward current.

A linear m -terminal element \mathcal{N} can be represented by the *indefinite admittance matrix*. We can, in fact, write the linear relationship between terminal voltages and currents as

$$J_k = \sum_{l=0}^m \bar{y}_{kl} E_l, \quad (1.10)$$

where

$$\bar{y}_{kl} = \left. \frac{J_k}{E_l} \right|_{E_j=0; j \neq l} \quad (1.11)$$

are complex quantities called *admittance coefficients*. By defining the column vectors $\mathbf{J} = (J_1, \dots, J_m)^T$ ³ and $\mathbf{E} = (E_1, \dots, E_m)^T$, the equation (1.10) can be written in matrix form as

$$\mathbf{J} = \bar{\mathbf{Y}} \mathbf{E}, \quad (1.12)$$

where $\bar{\mathbf{Y}} = (\bar{y}_{kl})_{m \times m}$ is the so called indefinite admittance matrix [10]. The main properties of this matrix are [8–12]:

- As a consequence of Kirchhoff's current law, the sum of all the elements in each column is zero, so that $\sum_k \bar{y}_{kl} = 0$ for any l .
- Since the terminal currents of \mathcal{N} should remain the same under a change of the reference node O , the sum of all the elements of each row of the matrix is zero, such that $\sum_l \bar{y}_{kl} = 0$, for any k . These first two properties make $\bar{\mathbf{Y}}$ a singular matrix.
- Consider the r th terminal connected to O , so that \mathcal{N} becomes an $(m - 1)$ -port element with port voltages $E_1, \dots, E_{r-1}, E_{r+1}, \dots, E_m$. It is possible to obtain its $(m - 1) \times (m - 1)$ *short-circuit admittance matrix* $\mathbf{Y} = (y_{kl})$ by deleting the r th row and column of $\bar{\mathbf{Y}}$. The matrix \mathbf{Y} is non-singular and, hence, it can be used to find the $(m - 1) \times (m - 1)$ open-circuit impedance matrix $\mathbf{Z} = (z_{kl}) = \mathbf{Y}^{-1}$ of the $(m - 1)$ -port element [8].

We can use the third property to determine a four-terminal impedance $Z_{ij,kl}$. In fact, by connecting the r th terminal to O , we can consider kr and lr as input ports respectively driven by the currents I_{kl} and $-I_{kl}$, and ir and jr as output ports with port voltages V_{ir} and V_{jr} . The ratio $V_{ij}/I_{kl} = (V_{ir} - V_{jr})/I_{kl}$ can then be obtained directly from the open-circuit impedance matrix \mathbf{Z} .

³T denotes the transpose operation.

Alternatively, it is possible to directly calculate $Z_{ij,kl}$ from the indefinite admittance matrix as [12, 13]

$$Z_{ij,kl} = \text{sgn}(k - l) \text{sgn}(i - j) \frac{\bar{\mathbf{Y}}_{kl;ij}}{\bar{\mathbf{Y}}_{11}}, \quad (1.13)$$

where $\text{sgn}(x)$ is the sign function, $\bar{\mathbf{Y}}_{11}$ is the first cofactor obtained by removing from $\bar{\mathbf{Y}}$ the first row and column, and $\bar{\mathbf{Y}}_{kl;ij}$ is the second cofactor obtained by removing from $\bar{\mathbf{Y}}$ rows number k and l , and columns number i and j .

Multi-terminal definitions of impedance are commonly employed in resistance metrology and are implemented by means of unshielded electrical cables and simple electromagnetic boundary conditions.

In the two-terminal definition (2T), shown in figure 1.5, the impedance Z is connected to the meter M through two conductors: the voltage V is measured across the same conductors in which the current I flows and electromagnetic boundary conditions are not imposed. For a two-terminal impedance, the measurement is affected by the following stray parameters due to the connections and to the environment:

- resistance of conductors;
- self- and mutual-inductance of the conductors;
- the cross-capacitance of the conductors;
- capacitances from the impedance body and the conductors to the environment average potential (ground).

The error due to these stray parameters is greater for very low or very high resistance values or for high-frequency measurements.

By adopting the four-terminal definition of impedance, it is possible to reject the effect of the series parameters of the conductors (resistance and self-inductances). In this configuration, shown in figure 1.6, the current flows through two current terminals of the impedance (C), while the voltage across the impedance is measured between two separate voltage terminals (P). Furthermore, no current should flow through the voltage terminals: $I_P = 0$. With these conditions, the DC measurement of a four-terminal resistance is no longer affected by stray resistances.

1.1.3 Multi-port elements

In the AC regime, the measurement of a four-terminal impedance is still affected by the following residual stray parameters:

- mutual-inductance of the conductors;

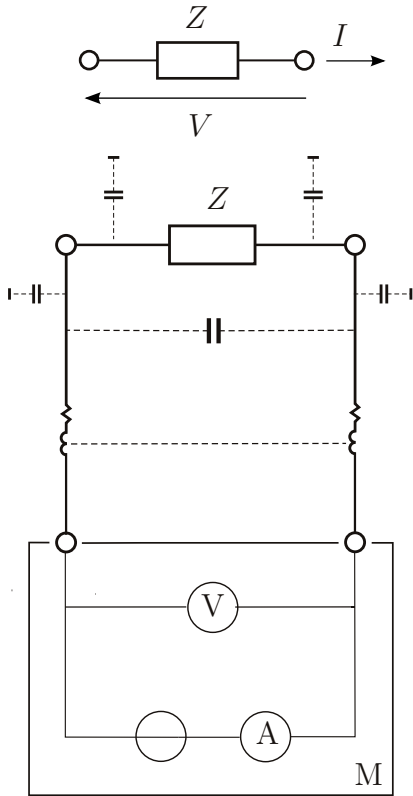


Figure 1.5: Two-terminal measurement of impedance: M is the meter, injecting a current into the impedance and measuring the voltage across its input terminals. The small elements represent stray resistances, inductances and capacitances. The black rectangles represent the average potential of the surrounding environment.

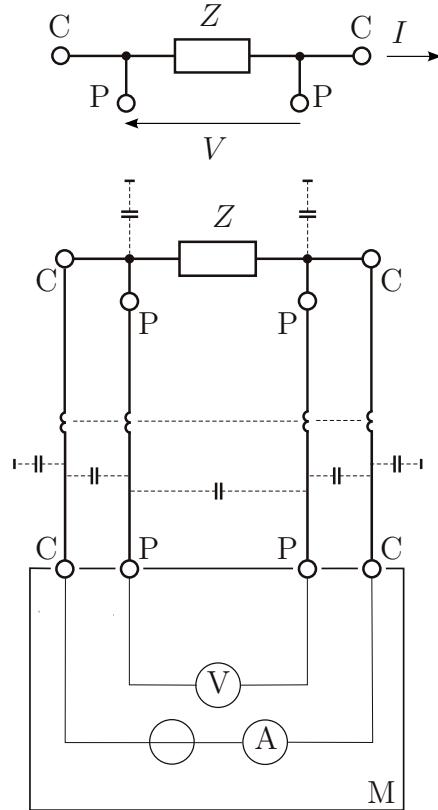


Figure 1.6: Four-terminal measurement of impedance: injecting a current into the impedance through the current terminals (C) and measuring the voltage across its voltage terminals (P).

- cross-capacitance of the conductors;
- capacitances from the impedance body and the conductors to ground.

Furthermore, in terminal definitions, the voltage V_{ab} between two terminals a and b of the impedance may depend on the measurement geometry, that is, on the integration path of the electric field. In fact, the voltage V_{ab} is defined as

$$V_{ab} \stackrel{\text{def}}{=} \int_{a \rightarrow b} \mathbf{E} \cdot d\mathbf{r}, \quad (1.14)$$

where the integral sign denotes the line integral along the path $a \rightarrow b$ from a to b , $d\mathbf{r}$ is the line element along the path, and \mathbf{E} is the electric field in the region containing the path. This definition limits the applicability of the terminal definitions to DC and low frequency measurements. In the AC regime, in fact, \mathbf{E} is no longer irrotational and V_{ab} is no longer uniquely defined because it now depends on the measurement (integration) path. This dependence becomes particularly significant at high frequency.

For AC measurements, the n -terminal-pair (or n -port) impedance definition is usually adopted. In this configuration, the impedance is shielded, all the n terminations are coaxial pairs (or ports) and the measuring circuit is interconnected by coaxial cables. For a coaxial circuit composed of two coaxial conductors, an inner one and an outer one, we can assume that:

- the electromagnetic boundary conditions are fixed by the the conductors and the impedance shield;
- at each cross section, the currents flowing in the inner and outer conductors have equal magnitudes, but opposite direction;
- the main mode of propagation is the transverse electromagnetic one, for which the voltage is uniquely defined between the inner and the outer conductors at each cross section.

Since both electric and magnetic fields are, to a first approximation, confined within the coaxial leads, because of the electrostatic shield and the coaxiality condition, mutual-inductances between leads are negligible.

In the two-terminal-pair impedance definition (or two-port), shown in figure 1.7, there are two ports, a high (H) and a low (L) port. Voltage V_H is defined at the port H, Current I_L at the port L, and the impedance is

$$Z_{2P} = \frac{V_H}{I_L}, \quad (1.15)$$

with the electromagnetic boundary condition $V_L \equiv 0$. In this configuration the measurement result is no longer influenced by the mutual inductance of the conductors, the cross-capacitance of the conductors and the capacitances between the impedance body and the conductors towards the environment average potential (ground). Yet, it is still affected by the series stray parameters of the leads, self-inductance and resistance. The two-terminal-pair configuration is widely employed in low-frequency impedance metrology for high- and medium-value impedances and also in high-resistance DC measurements.

In the *four-terminal-pair* (or four-port) impedance definition, shown in figure 1.8, there are four ports, the high (HC) and low (LC) current ports and the high (HP) and low (LP) voltage ports. The current is injected into the HC port,

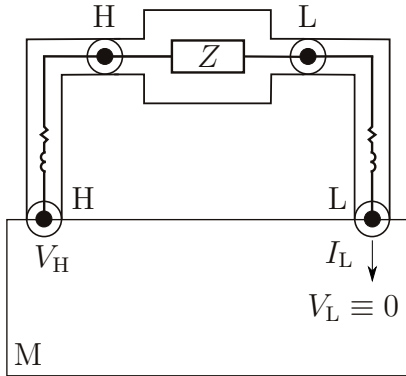
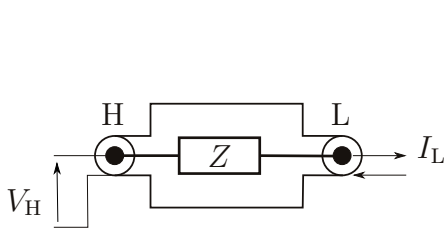


Figure 1.7: Two-terminal-pair (or two-port) measurement of impedance: measuring the current at the low port (L) of the impedance and the voltage at the high port (H), by fixing the electromagnetic boundary condition that $V_L \equiv 0$.

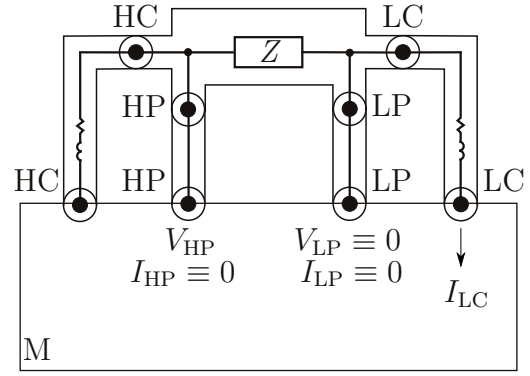
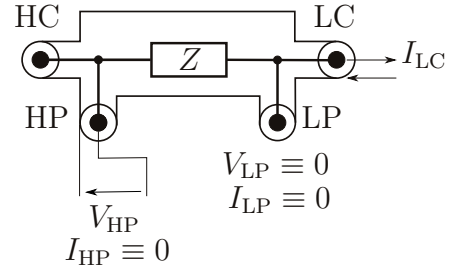


Figure 1.8: Four-terminal-pair (or four-port) measurement of impedance: measuring the current at the low current port (LC) of the impedance and the voltage at the high voltage port (HP), by fixing the electromagnetic boundary conditions that $I_{HP} \equiv 0$, $V_{LP} \equiv 0$ and $I_{LP} \equiv 0$.

the voltage is measured at the HP port, while the current is measured at the LC port. The four-terminal-pair impedance is defined as

$$Z_{4P} = \frac{V_{HP}}{I_{LC}}, \quad (1.16)$$

with the following electromagnetic boundary conditions:

$$I_{HP} \equiv 0, \quad (1.17)$$

$$V_{LP} \equiv 0, \quad (1.18)$$

$$I_{LP} \equiv 0. \quad (1.19)$$

In this configuration, the measurement result is no longer affected by any stray parameter, even the series ones, such as the lead self-inductance and resistance. The impedance definitions, especially the n -terminal-pair definitions, are usually implemented in impedance measuring systems through auxiliary circuits.

1.2 The International System of Units

Metrology is the science of measurement. Since people began to exchange goods, this discipline has been needed to agree on commonly accepted standards as a basis for fair trade. However, until the 18th century, many different standards were in use. This, of course, was a barrier to trade which led to abuse and fraud.

During the French Revolution, for the first time, the French *Académie des Sciences* took the initiative to define standards based on stable quantities of nature available to everyone at all times. Consequently, in 1799, a platinum bar was cast to represent the standard of length defined as the ten-millionth part of the quadrant of the earth (*Mètre des Archives*). The standard of mass, the kilogram, was defined as the mass of one cubic decimeter of pure water at the temperature of 3.98 °C [14], where density is highest, and represented by the *Kilogramme des Archives*.

This system was not really accepted throughout Europe, or even in France, until 1875, when 17 signatory countries of the Metre Convention accepted the metric system based on the meter and the kilogram. At the time of writing, the Metre Convention is signed by 61 states and other 41 states are associated with it. The *Conférence Générale des Poids et Mesures* (CGPM), consisting of the delegates of all contracting Governments, is the highest authority supervising the organization of the Metre Convention. Since the first CGPM in 1889, when the international prototype of the kilogram (IPK) was adopted as the basis of the unit of mass, the system of units has been continuously extended. In 1960, the 11th CGPM finally defined the International System of units (SI) with the kilogram, second, meter, ampere, kelvin, and candela as base units. Then, the 14th CGPM in 1971 added the mole, the unit of amount of substance, as the seventh base unit of the SI. At that time, the meter and the second were the only units defined by constants of nature. However, the SI is a system that changes according to the progress in science and technology, whenever there is consensus about the need for improvement.

In 2005, the article “Redefinition of the kilogram: a decision whose time has come” by Mills et al. [15] opened to the wider scientific community the discussion about the possible redefinition of the kilogram without an artefact. Furthermore, a major revision of the SI was suggested to overcome the limitations in the definitions of other units: the ampere, the kelvin, the mole. The general goal of the proposed revision of the SI was to consider the 20th century progresses in physics, concerning quantum and statistical physics, and technology, by avoiding definitions strictly linked to recommended practical realizations. The discussion brought the idea of an SI based on fixed fundamental constants. The work to fix the exact values of the fundamental constants took many years and involved several National Metrology Institutes (NMIs) worldwide.

The 26th CGPM, convened in Versailles in November 2018, approved the revision of the SI, which was then implemented on 20 May 2019, by adopting a system

where all the units are based on defining fundamental constants with exactly specified numerical values [16–19].

The kilogram definition changed for the first time since the adoption of the IPK in 1889, together with the definitions of the ampere, the kelvin and the mole. These changes are due to the revolutions in atomic physics and quantum metrology that characterized the second half of the 20th century and that allowed to link directly the definition of the units to natural constants. By adopting units definitions based on these atomic and quantum phenomena, the level of accuracy is limited only by our capacity to observe them.

The new definitions of the units are expressed in a form that specifies the numerical value of one of the seven constants, when expressed in SI units, and can be found in the 9th edition of the SI Brochure [16]. The seven defining constants are the unperturbed ground state hyperfine transition frequency of ^{133}Cs ($\Delta\nu_{\text{Cs}}$), the Planck constant (h), the speed of light in vacuum (c), the elementary charge (e), the Boltzmann constant (k), the Avogadro constant (N_{A}), and the luminous efficacy of monochromatic radiation of frequency 540×10^{12} Hz (K_{cd}) [20]. The SI brochure [16] defines the International System of Units as the system of units in which these defining constants have the numerical values presented in table 1.2, together with the associated base units, according to the 2017 CODATA adjustment [21, 22]. These numerical values do not exhibit uncertainty and have been chosen to ensure continuity between the past and present SI. The seven base units and the associated defining constants, represented in figure 1.9, fully define all of SI base and derived units, disconnecting the definition of a unit from its realization and providing a most fundamental, stable and universal reference.

In the present SI, a formal distinction between base and derived units has been maintained for pedagogical reasons and to keep consistency with international standards, but is no longer strictly necessary.

The experiments or the techniques realizing a unit can now be freely chosen on the basis of technological and scientific advances, without changing the definition. Furthermore, physical artefacts are no longer adopted. We can finally state that the present revised SI is conceptually superior than the previous one since it is based totally on constants of nature, which are independent on space and time, by considering the level required for present and near future metrology.

1.2.1 Resistance and impedance units in the SI

In the 20th century, quantum mechanics brought a new description of the reality. Parallel to the progresses in physics and technology, the present SI has evolved to exploit quantum effects to realize the electrical units. The most accurate realizations of the electrical units can be obtained by fixing two fundamental constants from quantum mechanics, the Planck constant h and the elementary charge e . The uncertainty in the realization of the electrical units is now limited only by the

Table 1.2: The seven constants, their values and the associated base units of the SI. The units hertz (Hz), joule (J), coulomb (C), lumen (lm), and watt (W) can be related to the base units through $\text{Hz} = \text{s}^{-1}$, $\text{J} = \text{kg m}^2 \text{s}^{-2}$, $\text{C} = \text{A s}$, $\text{lm} = \text{cd m}^2 \text{m}^{-2} = \text{cd sr}$, and $\text{W} = \text{kg m}^2 \text{s}^{-3}$.

Constant	Symbol	Value	Unit
Cs hyperfine transition frequency	$\Delta\nu_{\text{Cs}}$	9 192 631 770 Hz	second
Speed of light in vacuum	c	299 792 458 m s^{-1}	metre
Planck constant	h	$6.626\,070\,15 \times 10^{-34} \text{ J s}$	kilogram
Elementary charge	e	$1.602\,176\,634 \times 10^{-19} \text{ C}$	ampere
Boltzmann constant	k	$1.380\,649 \times 10^{-23} \text{ J K}^{-1}$	kelvin
Avogadro constant	N_{A}	$6.022\,140\,76 \times 10^{23} \text{ mol}^{-1}$	mole
Luminous efficacy	K_{cd}	683 lm W^{-1}	candela



Figure 1.9: The base units of the SI and their defining constants ©BIPM. All rights reserved.

quality of the implementations of the quantum phenomena.

The quantum Hall effect (QHE) is a macroscopic quantum effect that occurs in a two-dimensional electron gas at low temperature and in a strong magnetic field. The discovery of the QHE in 1980 by Klaus von Klitzing [23] made a quantum resistance standard available. In fact, the QHE provides quantized values of electric resistance that only depend on an integer index, the elementary charge e , and the Planck constant h . In 1985, Klaus von Klitzing was awarded the Noble Prize in physics for the discovery of the QHE, which has had a tremendous impact on resistance and impedance metrology.

In the present SI the definitions of the units are not associated to any specific realization, but the Appendix 2 of the 9th version of the SI Brochure reports two

recommendations for the mise en pratique of the electrical units [16, Appendix 2]. One of the recommended realizations for the resistance and impedance units is based on the QHE. This recommended realization depends on the universality of the QHE and of the accuracy of equation $R_K = h/e^2$, which has been experimentally tested in [24–35] (see section 1.3 for more details).

Here is reported the recommendation for the mise en pratique of the ohm⁴:

The ohm Ω can be realized as follows:

- (a) by using the quantum Hall effect in a manner consistent with the CCEM Guidelines [36] and the following value of the von Klitzing constant R_K :

$$R_K = 25\,812.807\,459\,304\,5\,\Omega. \quad * \quad (1.20)$$

* This value has been calculated to 15 significant digits.

This value follows from the assumption of the accuracy of the equation $R_K = h/e^2$, which is strongly supported by a large body of experimental and theoretical works, and the values of h and e given in [16]. Although the quotient h/e^2 can obviously be calculated with any number of digits, this truncated recommended value is in error by less than 1 part in 10^{15} , which is intended to be negligible in the vast majority of applications. In those rare cases where this error may not be negligible, additional digits should be employed. The advantage of recommending a particular value of R_K for practical use is that it ensures that virtually all realizations of the ohm based on the quantum Hall effect employ exactly the same value; or

- (b) by comparing an unknown resistance to the impedance of a known capacitance using, for example, a quadrature bridge, where, for example, the capacitance has been determined by means of a calculable capacitor and the value of the electric constant [...].

[16, Appendix 2]

Here is reported the recommendation for the mise en pratique of the farad⁵:

The farad F can be realized as follows:

⁴For consistency citation and equation numbers are adapted to the present text.

⁵The equation number reported in the quote below refers to this text.

- (a) by comparing the impedance of a known resistance obtained using the quantum Hall effect and the value of the von Klitzing constant given in Eq. (1.20) [...], including a quantized Hall resistance itself, to the impedance of an unknown capacitance using, for example, a quadrature bridge; or
- (b) by using a calculable capacitor and the value of the electric constant [...].

[16, Appendix 2]

Here is reported the recommendation for the mise en pratique of the henry⁶:

The henry H can be realized as follows:

- (a) by comparing the impedance of an unknown inductance to the impedance of a known capacitance with the aid of known resistances using, for example, a Maxwell-Wien bridge, where the known capacitance and resistances have been determined, for example, from the quantum Hall effect and the value of R_K given in Eq. (1.20) [...]; or
- (b) by using a calculable inductor of, for example, the Campbell type of mutual inductor and the value of the magnetic constant μ_0 [...].

[16, Appendix 2].

1.3 Realization of the units from the quantum Hall effect

This section is focused on the basic phenomenology of QHE. A detailed theoretical description of this effect is beyond the scope of this dissertation and is not here reported. More detailed presentations can be found, for example, in [37–46], where different approaches to the theory of QHE are reported. To date, however, a complete theory of this effect has not yet been developed.

The QHE is a macroscopic quantum effect that occurs in a two-dimensional electron gas (2DEG) at cryogenic temperature subjected to a perpendicular high magnetic field.

In a 2DEG the electrons can move freely in two dimensions, but their motion is confined in the third. This can be obtained by confining the electrons with electrostatic fields in semiconductor devices. Confining fields can be generated

⁶The equation number reported in the quote below refers to this text.

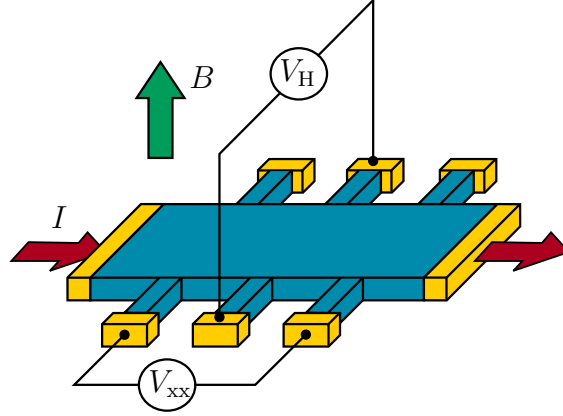


Figure 1.10: Representative drawing of a Hall bar. The measurement current I is injected along the longitudinal direction of a 2DEG device (here represented as a blue prism), subjected to a perpendicular high magnetic field. In these conditions, the transverse voltage V_H and the longitudinal voltage V_{xx} are measured across two contacts on the opposite and the same sides of the bar, respectively.

by a gate bias in silicon (Si) metal-oxide field-effect transistors (MOSFET), by the interfaces between layers of different composition in gallium arsenide (GaAs) heterostructures, or naturally in graphene.

In these conditions, if we inject a measurement current I along the longitudinal direction of a 2DEG device, such as the Hall bar of figure 1.10, the transverse resistance across two contacts on the opposite sides of the bar defines the Hall resistance $R_H = V_H/I$, which is quantized at values

$$R_H = \frac{R_K}{i}, \quad (1.21)$$

where i is a positive integer and

$$R_K \stackrel{\text{def}}{=} \frac{h}{e^2} \quad (1.22)$$

is the von Klitzing constant, or resistance quantum. At the same time, the longitudinal resistance $R_{xx} = V_{xx}/I$ measured between two contacts on the same side of the bar vanishes, so that

$$R_{xx} \approx 0, \quad (1.23)$$

since the scattering of electrons is suppressed [47].

The QHE breaks down above a certain critical current, typically of a few hundreds μA for the best devices [35, 48, 49].

Many works reported a deviation from the perfect quantization increasing with the measurement current and linearly coupled with the longitudinal resistance [31].

The Hall resistance is experimentally observed to be quantized over an extended range of the magnetic field. The width of these Hall resistance plateaus depends on the specific properties of the individual sample.

Nonetheless, it is established, also in theory, that the QHE is a universal quantum effect [24–26] and that the Hall resistance is accurately quantized, independently from the material in which the 2DEG is realized. The universality and reproducibility [27, 28] of the QHE and of the von Klitzing constant R_K was provided by experiments involving 2DEGs fabricated with different materials (Si-MOSFET [29, 30], GaAs/AlGaAs [31], graphene [32, 33]), different geometries [50] and with different electronic properties [30, 34, 35] with relative uncertainties of a few parts in 10^{11} .

Thanks to its universality, the QHE has been employed from 1990 to 2018 as a *representation* of the ohm and, in the present SI, as a realization. In recent years, the QHE has been also employed in the AC regime for impedance metrology, to directly realize the farad [51, 52].

1.3.1 QHE devices

Quantum Hall resistance standards for resistance and impedance metrological applications have been mostly based on 2DEGs in GaAs/AlGaAs heterostructures. Recently, a new material, called *graphene*, was found to exhibit the QHE in less demanding experimental conditions and then employed for metrological applications.

GaAs/AlGaAs heterostructures

A 2DEG system can be realized by semiconductor heterojunctions [53], for the development of which, in 2000, Kroemer and Alferov were awarded the Nobel Prize in physics. A heterojunction is the interface between a semiconductor and a metal or an insulator (for example, the Si/SiO₂ interface in MOSFETs), or two semiconductors with different band gap energies (for example, the GaAs/AlGaAs interface). A structure composed of one or more heterojunctions is called a heterostructure.

GaAs is a direct-gap semiconductor characterized by a band gap energy $E_g \approx 1.42$ eV. It is composed of an element of the third (Ga) and one of the fifth (As) groups of the periodic table and forms a III–V compound semiconductor.

AlAs is also a III–V compound semiconductor characterized by an indirect band gap with $E_g \approx 2.16$ eV.

$\text{Al}_x\text{Ga}_{1-x}\text{As}$, where x is the aluminium mole fraction, is a ternary mixed crystal and a III–V compound semiconductor where the Ga and Al atoms are randomly distributed over the lattice sites of the group III elements. The band gap energy varies from 1.42 eV (GaAs, $x = 0$) to 2.16 eV (AlAs, $x = 1$), and increases with decreasing temperature. For $x < 0.45$, the ternary compound has a direct band gap as in GaAs.

Thanks to the fortunate circumstance that GaAs and $\text{Al}_x\text{Ga}_{1-x}\text{As}$ have almost the same lattice constant, high-quality GaAs/ $\text{Al}_x\text{Ga}_{1-x}\text{As}$ heterostructures can be fabricated with epitaxial crystal growth techniques, like molecular beam epitaxy (MBE) [54] or metalorganic vapor-phase epitaxy (MOVPE).

MBE is performed in an ultrahigh vacuum chamber with an ultralow impurity concentration. The growth rate is very low, typically about $1\ \mu\text{m h}^{-1}$, which corresponds to one GaAs monolayer (0.28 nm thick) per second. This allows to control with single atomic layer resolution the thickness of the structure. Then, a Si effusion cell is used to dope the GaAs or $\text{Al}_x\text{Ga}_{1-x}\text{As}$ layers.

In MOVPE, the metalorganic compounds (that provide Ga and Al) are transported by a carrier gas (like hydrogen) to a reaction chamber, where they chemically react with the group-V precursor, supplied as hydrides, at the surface of the substrate, on which the GaAs/ $\text{Al}_x\text{Ga}_{1-x}\text{As}$ heterostructure grows epitaxially. MOVPE operates at a pressure of $10^4\ \text{Pa}$, higher than that required by the MBE.

With both epitaxial methods, it is possible to deposit a thin layer of GaAs between two layers of $\text{Al}_x\text{Ga}_{1-x}\text{As}$, with $x = 0.3$, for which $E_g \approx 1.8\ \text{eV}$ at room temperature.

Figure 1.11 shows the cross-section of a typical GaAs/AlGaAs heterostructure and the energy-band diagram.

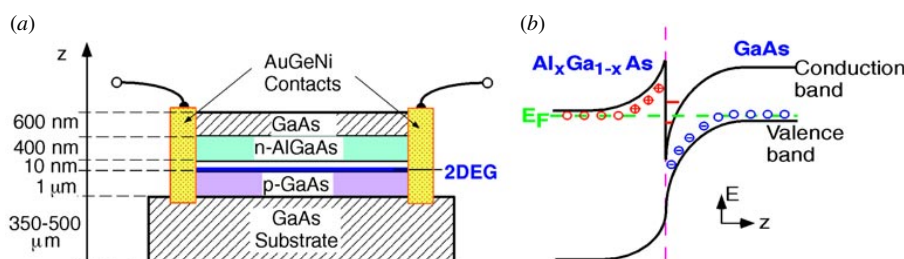


Figure 1.11: (a) Cross-section of a typical GaAs/AlGaAs heterostructure. (b) Energy-band diagram at the GaAs/ $\text{Al}_x\text{Ga}_{1-x}\text{As}$ interface.

The misalignment of the bands in the layers of the heterostructure, shown in figure 1.11, influences the electronic properties, since it results in the formation of potential wells, ideally with a rectangular shape, in the conduction and valence bands, thus confining both electrons and holes. In this way, a 2DEG can be produced in a potential well confined by the heterojunctions.

The concentration of charge carriers can be modified by doping, that is, by replacing the original lattice atoms with donor or acceptor atoms. At low temperature, semiconductors with wide energy gap usually have low density of intrinsic conduction electrons. Thus, to study effects at low temperature, like the QHE, it is necessary to dope the semiconductor with donors to provide an excess of electrons in the conduction band. However, with this method, even at low temperatures, scattering at ionized donors limits the electron mobility. Scattering can be strongly

reduced by the so-called modulation doping [55]. In this type of doping, donors are spatially separated from the mobile electrons, so that the scattering at ionized donors decreases and the carriers mobility increases.

A modulation-doped heterostructure consists of a GaAs/Al_xGa_{1-x}As interface in which the Al_xGa_{1-x}As is doped with Si donors. The electrons diffuse from the doped Al_xGa_{1-x}As layer into the undoped GaAs one, thus providing high mobility electrons. The resulting charge distribution forms a quasi-triangular quantum well. The lowest quantized energy level of the potential well is located below the Fermi level and is hence populated with electrons. As a result, a 2DEG is formed at the interface. Typically, between the GaAs and the Al_xGa_{1-x}As layers, there is an additional undoped Al_xGa_{1-x}As spacer layer, which reduces the scattering at the interface. This type of heterostructures are used in most of today's devices for resistance and impedance metrology. For this type of applications, the optimal carrier density ranges from 3×10^{15} to 5×10^{15} cm⁻² and the electron mobility ranges from 10 to 80 T⁻¹ [56].

The QHE devices are fabricated by usual lithography and etching techniques with a Hall bar geometry (see figure 1.10). To realize the contacts with the 2DEG, annealed AuGeNi is laterally deposited at the edges.

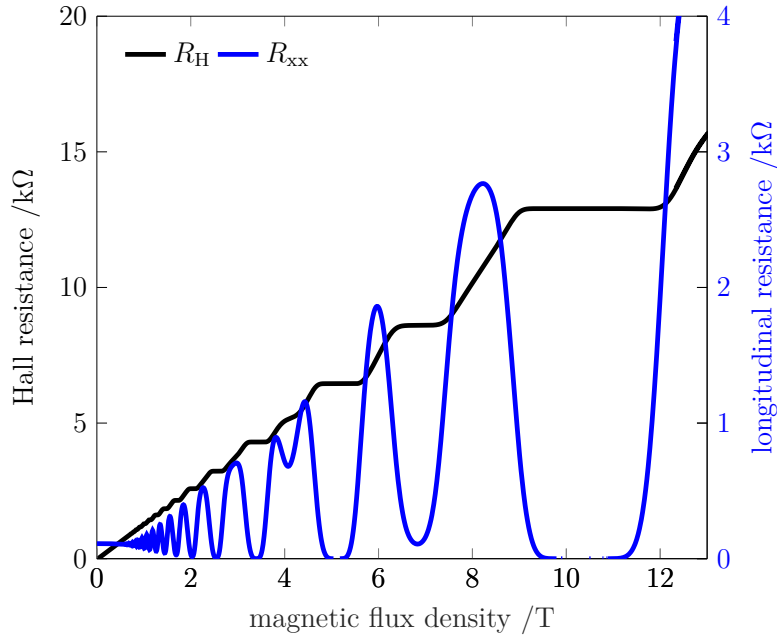


Figure 1.12: Magnetic field dependence at 2.5 K and 25 μ A of the Hall and the longitudinal resistance R_H and R_{xx} of a GaAs/AlGaAs Hall bar heterostructure (Laboratoire Electronique Philips LEP 514). The Hall resistance exhibits plateaus corresponding to $R_H = R_K/i$ (with $i = 1, 2, 3, \dots$) and, correspondingly, the longitudinal resistance vanishes ($R_{xx} \approx 0$). Data courtesy of C. Cassiago, INRIM.

Figure 1.12 shows the typical magnetic flux density dependence at low temperature of the Hall and longitudinal resistances R_H and R_{xx} of a GaAs quantized Hall resistance (QHR) standard. The Hall resistance exhibits plateaus at R_H/i with $i = 1, 2, 3, \dots$ and, correspondingly, the longitudinal resistance vanishes. GaAs QHR standards are usually well quantized at very low temperature, below 4.2 K, and high magnetic flux density. In fact, the $i = 2$ Hall resistance plateau corresponding to $R_H \approx 12\,906.4\,\Omega$, which in figure 1.12 is approximately between 9 T and 12 T, is the widest and more accurate plateau, usually within one part in 10^9 . The breakdown current is of a few hundreds of μA for the best devices [56]. As a result of studies and measurements performed by metrologists on these devices, technical guidelines [36] about the device properties and the characterization techniques were recommended. The main parameters to check if a QHR standard is accurately quantized are the contact resistances below $10\,\Omega$ and the longitudinal resistances below $100\,\mu\Omega$ [36].

Graphene

The realization of the SI ohm with QHR standard made from GaAs/AlGaAs heterostructures requires highly specialized personnel and equipment typically available only at NMIs. In fact, such kind of QHR standards operate at low temperatures and high magnetic fields, around 1 K and 10 T, depending on the material properties.

In 2004, Andre K. Geim and Konstantin S. Novoselov presented the exceptional properties of a new material called graphene [57–59]. For the production of this material and their groundbreaking studies about its properties, they were awarded the Nobel Prize in physics in 2010. It has been recently demonstrated [33] that graphene can exhibit the QHE at higher temperatures and lower magnetic fields with respect to GaAs/AlGaAs heterostructures, so that graphene QHR standards may be more easily employed in metrology.

Graphene is the two-dimensional allotrope of carbon, considered as the building block of the three-dimensional graphite. Monolayer graphene, the most important type in metrology, is a single layer of carbon atoms organized in a honeycomb lattice with strong σ bonds formed by hybrid sp^2 orbitals. The p_z orbitals, unaffected by hybridization, are oriented perpendicularly to the layer and form a half-filled π band [60].

The band structure, which can be obtained with the tight-binding method [60, 61], is such that the valence and the conduction bands touch at six points in the Brillouin zone. These are called Dirac points [60, 62]. For this reason, monolayer graphene is considered a semimetal with zero band gap energy. Around Dirac points, the dispersion curve between energy and wavevector is linear [60, 62], similar to that of massless relativistic particles. Thus, close to the Dirac points, the quasielectron wavefunctions are the solutions of a Dirac equation. When graphene

is undoped, the Fermi energy is located at the Dirac point. By doping or applying an electric field, it is possible to generate a 2DEG of almost massless electrons. A more detailed description of graphene electronic properties is presented, for example, in [60, 62].

Graphene can be produced with different methods, such as mechanical exfoliation, chemical vapour deposition or epitaxial growth. Monolayer graphene was isolated by mechanical exfoliation from graphite in the work of Geim and Novoselov [57–59]. This method is not suitable for metrology, since it produces layers rarely larger than a few hundreds of μm^2 with, as a consequence, a small breakdown current of the QHE [63]. This limits the measuring current and, in turn, the measurement uncertainty.

Graphene layers with larger area can be fabricated by chemical vapour deposition on metallic surfaces. These act as catalysts for the decomposition of carbon hydrides [64]. However, the transfer of a graphene layer from a metallic to a non-conducting substrate may degrade the quality of the graphene. For this reason, this technique is not used in the most recent work on QHE for metrological applications.

The preferred method is now the epitaxial growth by high-temperature sublimation of silicon carbide (SiC), since with this method the graphene layers grow directly on a nonconductive substrate. To grow a monolayer graphene the SiC has to be an hexagonal polytype of SiC, 4H-SiC or 6H-SiC, to provide a well-suited template for the hexagonal graphene layer. At temperatures from around 1400 °C to 1900 °C, the silicon sublimates and forms a thin carbon layer [65, 66], with properties that depend on various parameters and conditions. The graphene monolayer grows on a carbon buffer layer, which is covalently bonded to the SiC substrate [67]. By controlling the growth parameters and conditions, it is possible to obtain larger uniform graphene layers [68, 69]. The graphene layers growth with this technique may be not perfectly flat because, during the annealing phase, the restructuring of the SiC surface results in monolayer graphene terraces separated by step edges [66, 68, 69], also as high as 10 nm, along which bilayer graphene nucleates. This can cause anisotropic deviations from the perfect QHR [70]. Supplying additional carbon from a polymer adsorbate stabilizes the SiC surface and, thus, prevents the formation of the terraces, improving the growth of monolayer graphene [71] with maximum step heights of only 0.75 nm. This technique allows the growth of millimeter-sized uniform graphene monolayers, suitable for metrology applications.

In metrology, it is often preferred to measure the QHR close to the smallest possible integer filling factor i and at low magnetic fields. To achieve these conditions, it is necessary to decrease the electron density in the graphene layer from 10^{12} – 10^{13} cm^{-2} , typical of epitaxially grown graphene and due to the donor states in the carbon buffer layer, to around 10^{11} cm^{-2} [62]. There are several techniques to reduce the electron density. An electric field can be applied to a gate structure deposited on top of the graphene monolayer, but additional fabrication steps are required, which may damage the graphene layer. Furthermore, the gate voltage

needs to be continuously applied to keep the electron density stable. The electron density can also be controlled with photochemical gating [72], by permanently depositing on the graphene a polymer spacer layer and a photosensitive resist layer. Then, activated by ultraviolet (UV) radiation, acceptor states form in the photosensitive resist, effectively reducing the electron density, which is reported to remain constant for several months. It is possible to undo the process and recover the high electron density by thermal annealing. Other gating methods use polymer coatings subjected to corona discharge [73] or a chromium tricarbonyl ($\text{Cr}(\text{CO})_3$) functionalization of the graphene layer [74].

QHR standards in graphene monolayers are more practical to be implemented, since they can be operated under relaxed experimental conditions with respect to GaAs ones. Monolayer graphene, in fact, exhibits the so-called half-integer QHE [58, 59, 62], with

$$R_{\text{H}} = \frac{1}{j - \frac{1}{2}} \frac{h}{4e^2}, \quad (1.24)$$

with $j = 1, 2, 3, \dots$. The dependence on j is due to the peculiar band structure of graphene.

The behaviour expressed by (1.24) is confirmed by the experimental data presented in figure 1.13 [75], which shows the typical magnetic field dependence of the Hall resistance and longitudinal resistivity of monolayer graphene Hall bar. At a temperature $T = 2$ K and a current $I = 10$ μA , the Hall resistance exhibits the $R_{\text{H}} = R_{\text{K}}/2 \approx 12\,906.4 \Omega$ plateau corresponding to $i = 2$ at a relatively low magnetic field, $B \approx 3$ T.

Since the band structure of monolayer graphene differs from that of semiconductors conventionally used in metrology, graphene has been employed to test the reproducibility and universality of the QHE [76], by measuring over long times and at temperatures and magnetic fields similar to those commonly used to operate GaAs QHR standards. The agreement between the QHR in exfoliated graphene and in GaAs/AlGaAs heterostructures was found to be within few parts in 10^9 [76]. The agreement between the QHR in epitaxial graphene and in GaAs/AlGaAs heterostructures was found to be within few parts in 10^{11} [32, 77]. The agreement between the QHR in graphene produced by CVD on SiC and in GaAs/AlGaAs heterostructures was found to be within few parts in 10^{11} [78].

For graphene devices, in the space defined by temperature, magnetic field and current density, the manifold which bounds QHE states is more extended than in GaAs. Therefore, in graphene, the QHE can be obtained with sufficiently low uncertainty also at less demanding experimental conditions, that is, at a lower magnetic field and/or higher operating temperature. For example, the QHE was even observed at room temperature by applying a magnetic field of 29 T [79]. For what concerns the critical current density of graphene, at 7 T this is of several A m^{-1} [63] and at 10 T is even higher, whereas the typical one for GaAs devices is 1 A m^{-1} [31]. Taking into account these limitations, [78] reports QHE measurements at 5 T and

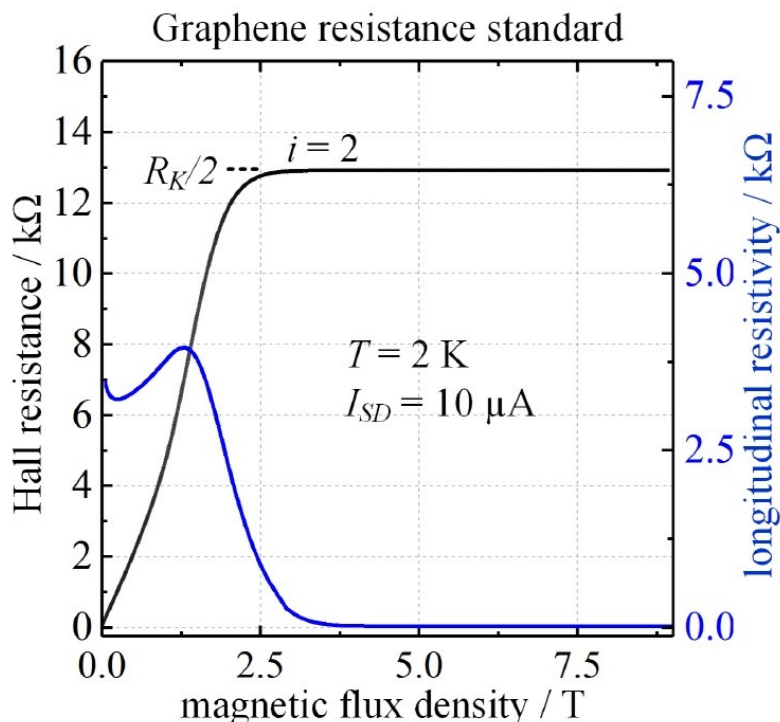


Figure 1.13: Magnetic field dependence at 2 K and 10 μA of the Hall resistance and the longitudinal resistivity of an epitaxial graphene Hall bar at a charge carrier density $n \approx 1.5 \times 10^{11} \text{ cm}^{-2}$. The Hall resistance exhibits a plateau with the value of $R_H = R_K/2$, corresponding to $i = 2$, at a relatively low magnetic flux densities of $B \geq 3 \text{ T}$ and, correspondingly, the longitudinal resistivity vanishes. Reproduced with permission from [75] ©IOP Publishing. All rights reserved.

5 K in graphene with an uncertainty of 10^{-9} . These measurements conditions testify the beginning of a new era, when also small cryogen-free system can be employed to measure quantized Hall resistances in graphene with metrological accuracy (few parts in 10^9) [80, 81]. These are important steps toward a more practical realization of QHR standards.

From monolayer graphene, QHE devices are then fabricated by traditional lithographic techniques and etching processes with a Hall bar geometry (see figure 1.10). Contacts with graphene are usually realized with a strongly interacting metal [82, 83], such as Pd or Ni, to reduce the metal-graphene contact resistance, and Au. The Ti/Au bond pads are then deposited to support conventional wire-bonding. Moreover, windows or meandered graphene edges can improve the side-contacting capability of the sheet [84]. Quantized resistances, normally measured at four terminals for high precision, can also be measured at two terminals by eliminating undesired resistances when applying superconducting split contacts [85].

1.3.2 Quantum Hall Array Resistance Standards

A quantum Hall array resistance standard (QHARS) is an integrated circuit composed of several QHE elements connected together. With series, parallel or bridge connections, QHARSs can provide fractions or multiples of the quantized resistance value [86–91].

The unique properties of the QHE, such as the perfect equipotentiality along the edges of the bar and the quantization of any two-terminal resistance at the same value, can be exploited to reject the effect of the stray resistances at contacts and interconnections in four terminals measurements. In fact, in a QHARS, the interconnections among the QHE elements are realized as *multiterminal connections*, such as multiple-series, multiple-parallel or multiple-bridge connections, characterized by an order m identifying the number of connections between each group of devices and the order $O(\epsilon^m)$ of the residual effect of the stray resistances [9, 86, 92]. For example, if two QHE elements are connected by an m -series or an m -parallel connection, then

$$R_S^m = 2R_H(1 + O(\epsilon^m)), \quad R_P^m = \frac{R_H}{2}(1 + O(\epsilon^m)), \quad (1.25)$$

where R_S^m and R_P^m are the four-terminal resistances of the m -series and m -parallel connection of the two QHE elements, respectively, and ϵ is the ratio between the maximum interconnection resistance and R_H .

Figure 1.14 and 1.15 show a triple-series and a -parallel connection ($m = 3$) of two QHE elements, respectively. Therefore, by exploiting the multiple connection technique, it is possible to extend the range of QHR standards available. Decadal resistance values (100 Ω , 1 k Ω , 10 k Ω , ...) are particularly interesting for metrological applications.

QHARSs of GaAs/AlGaAs QHE devices with triple- or quadruple-connections were developed by several NMIs [88, 93–97].

Accurate QHARSs require the quantization of all the QHE elements at the same magnetic flux density. This condition is restrictive for GaAs/AlGaAs QHARSs, since a very homogeneous electronic density (to within a few percent) is needed because of the short width of the R_H plateaus. This condition is overcome in graphene QHARSs, since the $i = 2$ R_H plateau covers a wide range of magnetic field values.

QHARS may suffer from stray resistances at contacts and interconnections. Furthermore, the crossover of the electrical multiple-connections between the QHE elements requires perfect insulating layers that may introduce other stray components, such as leakage currents through the dielectric where the voltage terminals need to cross the current path. Split-contact geometry and superconducting interconnections can be employed to minimize the effect of these stray components and ensure precise resistance quantization [85, 98], as recently proved for a graphene

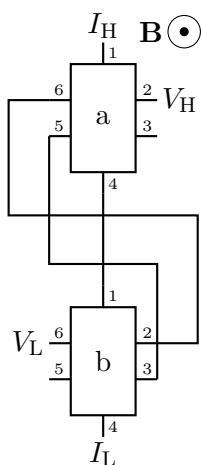


Figure 1.14: Triple-series connection of two QHE elements, a and b. Each element is provided with two current contacts (1,4) and four voltage contacts (2,3,5,6). The resulting network has two current terminals, I_H and I_L , and two voltage terminals, V_H and V_L .

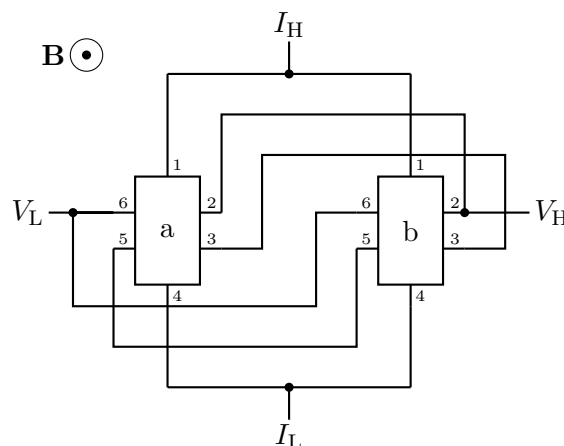


Figure 1.15: Triple-parallel connection of two QHE elements.

QHARS exhibiting a deviation from the nominal resistance value of the order of 10^{-9} [98].

1.3.3 Quantum Hall effect in the AC regime

In the AC regime, the resistance of a QHR standard is also expected to remain quantized within one part in 10^9 at frequencies in the kilohertz range [99, 100]. Therefore, the AC QHE can be employed for metrological applications to realize QHR standards operating in AC and providing traceability of impedances.

To preserve the perfect quantization of the Hall resistance in the AC regime, specific techniques are exploited. The Hall bar, for instance, is implemented by means of multiple-connections, introduced in section 1.3.2, to cancel the large quadratic frequency dependencies due to series inductance and to ensure the zero current requirement in the voltage arm of the QHR standard [101, 102]. Some works have reported a residual deviation from the perfect quantization of a few parts in 10^8 at 1 kHz, linearly increasing with frequency and current [103], and linearly coupled with the longitudinal resistance, as in the DC regime. This contribution is ascribed to AC current losses in the internal capacitances of the Hall bar and in the external stray capacitances toward ground. The double-shielding technique of the Hall bar can be implemented to cancel the frequency dependence of the QHR to within

$1 \times 10^{-9} \text{ kHz}^{-1}$ [102].

1.4 Resistance and impedance calibration techniques in the SI

The most common calibration techniques employed in resistance and impedance metrology are based on the comparison between one or more reference standards and a standard under calibration by means of a *bridge*.

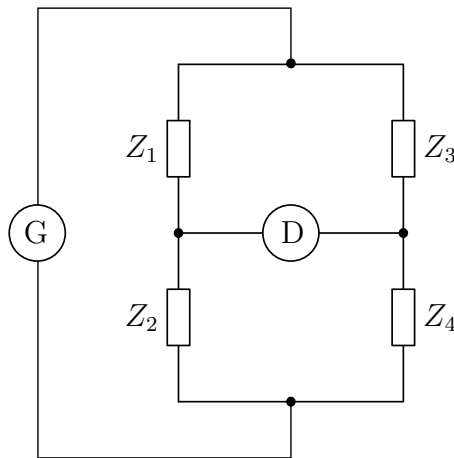


Figure 1.16: Principle schematic diagram of a Wheatstone bridge. The bridge is composed of the impedances Z_1 , Z_2 , Z_3 and Z_4 driven by the generator G , which can be a voltage or a current source. D is the detector, whose reading is zero when the bridge is balanced.

The prototype arrangement of a bridge is that of the *Wheatstone bridge*, shown in figure 1.16. This device compares the two-terminal resistances or impedances Z_1 , Z_2 , Z_3 and Z_4 , arranged in two voltage or current dividers driven by the voltage or current generator G . When the voltage or current detector D measures zero, the bridge is *balanced*, or in *equilibrium*, so that,

$$\frac{Z_1}{Z_2} = \frac{Z_3}{Z_4}. \quad (1.26)$$

In this case, the bridge measures one of the impedances, the one under calibration, in terms of the others, the *reference standards*. If one or more reference standards are variable, the bridge can be balanced by modifying their values until the detector indicates zero. This is the *null mode* of operation.

The Wheatstone bridge can be rearranged as a *voltage ratio bridge* or a *current ratio bridge*. In the voltage ratio bridge shown in figure 1.17, the ratio of the

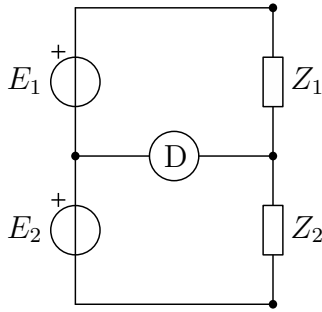


Figure 1.17: Voltage ratio bridge. E_1 and E_2 are two voltage sources, with a known voltage ratio.

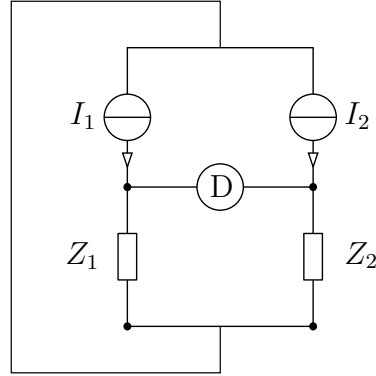


Figure 1.18: Current ratio bridge. I_1 and I_2 are two current sources, with a known current ratio.

impedances Z_1 and Z_2 , which constitute a voltage divider, is compared with the known ratio of the voltages E_1 and E_2 , such that the bridge balance equation is

$$\frac{E_1}{E_2} = \frac{Z_1}{Z_2}. \quad (1.27)$$

In the current ratio bridge shown in figure 1.18, the ratio of the impedances Z_1 and Z_2 , which constitute a current divider, is compared to the known ratio of the currents I_1 and I_2 , such that the bridge balance equation is

$$\frac{I_1}{I_2} = \frac{Z_2}{Z_1}. \quad (1.28)$$

This means that any voltage or current ratio device can be employed to construct a bridge, such as transformers, voltage/current dividers or digital signal sources.

Furthermore, there are bridges designed for more complex (e.g. four-terminal or two- and four-port impedances) impedance definitions, which contain auxiliary networks and sources.

In the DC regime, QHE devices realize the ohm and, as DC QHR standards, they are used by NMIs to calibrate resistance standards with decadal values. Different resistance bridges, reported in section 1.4.1, are used for the calibration, depending on the target uncertainty level: potentiometric bridges (section 1.4.1), commercial bridges based on a direct current comparator (section 1.4.1), or bridges equipped with cryogenic current comparators (section 1.4.1).

In the AC regime, the farad is realized from the QHE by means of impedance bridges, as reported in section 1.4.2. The traceability chain can be based on a DC QHR standard (section 1.4.2), or on a QHR standard in the AC regime, that is, an AC QHR standard (section 1.4.2).

The henry is usually obtained from calibrated AC standard resistors or from the farad, by means of impedance bridges.

1.4.1 Resistance calibrations

Potentiometric bridge

The potentiometric method is based on the comparison of the voltages across two resistors, the DC QHE resistance standard R_H and the resistance standard under calibration R_S , connected in series and driven by a high-stability DC current source. The potentiometric set-up is composed of a potentiometer and a high-resistance voltage detector. The voltage across R_H is compared against a closely adjusted voltage generated by the potentiometer using the detector [104]. Then, the same comparison is repeated for R_S . The two ratio measurements are repeated for the reversed current, so that, at the end of the whole process, linear drifts of the current sources and thermal voltages are rejected. The resistance ratios 1 : 1 and 1.29 : 1 can be measured with a relative uncertainty of few parts in 10^8 [105]. A method adopted by several NMIs for the scaling to other decadal resistance values is a Hamon type series-parallel resistor network [106].

The bridge performances improve significantly if the potentiometer is replaced by a Josephson reference [107], or by employing a dual Josephson potentiometer [108]. Although the uncertainty achieved with these improvements are competitive, the resistance bridge based on the cryogenic current comparator achieves a lower uncertainty.

Direct current comparator

The sequential procedure requested by the potentiometric method can be affected by the shot-term instability of the source, and this is the main limit of the method. To overcome this problem, the two resistance standards under comparison can be placed in two separate current loops, tracking one another. The ratio between these two currents is measured by a DC comparator [109, 110], through two windings wound on a high-permeability toroidal core and a second-harmonic flux-gate magnetometer. A servo circuit from the output of the magnetometer controls the current in one of the loops, to keep zero flux in the magnetic core. The number of windings on the other loop is adjusted so that the voltages across the two resistances are the same. This second balance is checked by a voltage detector. When the flux and the voltage balances are obtained at the same time, the ratio between the resistance standards is equal to the ratio between the windings in the two loops. The accuracy achievable with this method is of a few parts in 10^8 for the measured ratio whereas the resolution is limited by the noise of the magnetic modulation. Nowadays, commercial instruments, able to self-calibrate the current ratios are available on the market [111].

Cryogenic current comparator

The magnetic error caused by the flux leakage from the ferromagnetic core (whose permeability is finite) is the main limitation of the current comparator. Flux leakage can be virtually eliminated by employing superconducting shielding. The Meissner effect, in fact, excludes the magnetic induction from a superconductor in an external magnetic field less than its critical field, so that it becomes perfectly diamagnetic and a surface-shielding current is produced. Therefore, the volume enclosed in the superconducting surface is completely shielded by external DC or AC magnetic fields. Furthermore, when a volume is multiply connected, for example in a torus, a magnetic field can be completely confined within.

Superconducting shielding requires a cryogenic environment to operate. The resulting instrument is thus called *cryogenic current comparator* (CCC) [112, 113]. In this environment, it is also possible to employ the most sensitive magnetometric technique available, based on *superconducting quantum interference devices* (SQUIDs). These devices exploiting a macroscopic quantum charge transport effect, allows to achieve a very high sensitivity, at the level of $\text{fT Hz}^{-\frac{1}{2}}$.

Automated CCC bridges can achieve relative accuracies of a few parts in 10^{10} . Nowadays, the CCC is employed by several NMIs as the main method to calibrate resistance standards, against other resistance standards or directly against a QHR standard.

1.4.2 Impedance calibrations

Over the years, NMIs have adopted different measuring systems for the realization of the capacitance, inductance and resistance scales at audio-frequencies [114, 115]. As discussed in section 1.4, the measuring systems mainly employed are the impedance bridges, which, once balanced, compare the impedance ratio with a voltage or current ratio. Thus, the accurate generation or measurement of this voltage ratio is the main challenge of impedance metrology. Traditionally, different bridges are employed for different types of comparisons: ratio bridges compare impedances of the same type; quadrature bridges compare capacitances with resistances; Maxwell-Wien or resonance bridges compare inductances to resistances and capacitances.

In traditional implementations of voltage ratio bridges, the accurate voltage ratio is generated using a ratio transformer or an inductive voltage divider (IVD), over the years optimized to achieve the highest accuracy, 1×10^{-9} [116, 117]. These bridges are now employed also for the direct calibration of a 10 pF against the QHR standard in the AC regime (AC QHR) with a standard uncertainty of 6×10^{-9} at 1233 Hz [51]. The measurement system developed for this purpose is very complex, its operation is time consuming and requires highly skilled operators. Moreover, the transformers are fabricated so that the bridge can work only at fixed ratios (usually

1:1 and 10:1) at which only pure impedance standards (resistors, capacitors and inductors) can be compared.

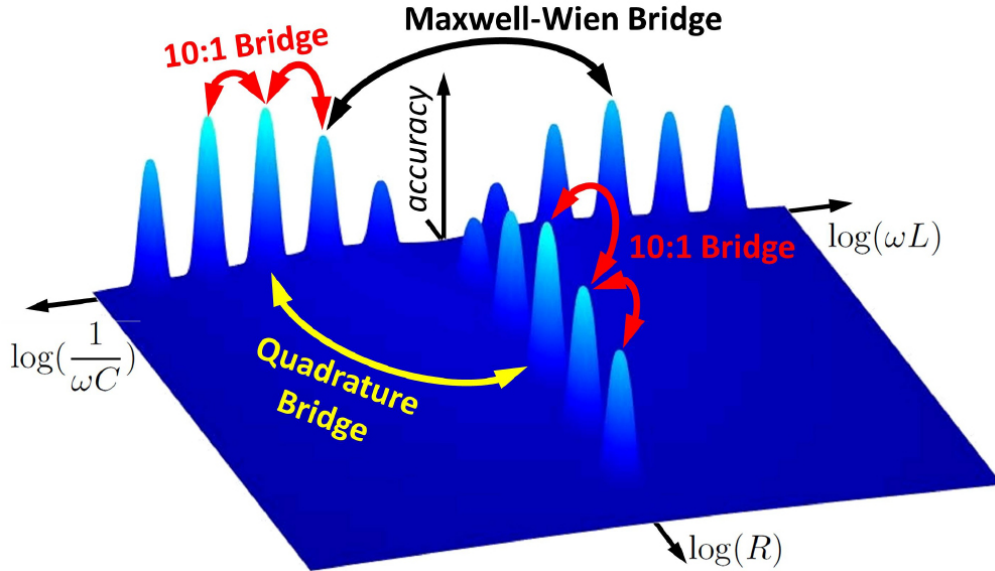


Figure 1.19: Accuracy landscape of the impedance bridges based on ratio transformers used for the impedance calibrations. Reproduced with permission from [7] ©IOP Publishing. All rights reserved.

At present, the best calibration performances are obtained with transformer-based impedance bridges. However, with these devices the possible voltage ratios are fixed, since they are set by choosing the number of turns of the windings during the fabrication of the transformer, and the phase shift between the generated voltages is limited to either 0° or 180° . These limitations are well represented by the graph of figure 1.19, which shows the accuracy landscape of the transformer bridges traditionally employed by impedance metrology for impedances located in the complex plane [7]. The highest accuracies are achieved for comparison between impedances lying along the axes of the complex plane. For the other impedances, the accuracy achievable is extremely low.

Recently, digital impedance bridges based on fast and accurate DACs and ADCs [118] allow the comparison of any kind of impedances, located over the whole complex plane.

In general, digital impedance bridges can be classified on the basis of the implemented impedance definition (two-terminal pair or four-terminal pair), of the reference quantity (voltage ratio or current ratio), of the bridge architecture (digitally assisted, if the reference ratio is defined by a transformer, or fully digital, if the reference ratio is completely defined by a digital system), of the source type (electronic, if the source is based on digital electronics, or Josephson, if the source is a

programmable Josephson voltage standard or a Josephson arbitrary waveform synthesizer), of the ratio reading (sourcing, generating or based on digital-to-analogue converters (DACs), if the reference ratio is determined by the settings of a digital signal source, or digitizing, sampling or based on analogue-to-digital converters (ADCs), if the reference ratio is determined from digitized samples).

Digitally-assisted bridges can use computer controlled IVDs [119, 120], electronic sources [121–124] or high resolution DACs [125–130], so that the balancing procedure can be controlled by an adequate algorithm [131] and performed automatically within a few minutes with an uncertainty level of a few parts in 10^8 .

The ability of digital bridges to compare impedances located on the whole complex plane results in a significant simplification in the realization of the various impedance chains. Furthermore, digital bridges can be able to calibrate capacitances (and, potentially, inductances) directly against the ACQHR, providing a primary realization of the farad (and of the henry) using a single measurement system.

Nowadays, the dual Josephson impedance bridge (DJIB), based on two Josephson arbitrary waveform synthesizers, achieves the best accuracy obtainable with a digital impedance bridge, that is, at the level of few parts in 10^8 [132–134]. These performances are not yet comparable with the traditional transformer-based impedance bridges, even though the DJIB outperforms all of them in terms of flexibility, automation and frequency range.

Since transformer-based impedance bridges were not employed in this thesis, the following sections of this dissertation are only focussed on the new generation of digital bridges. This section introduces the main characteristics of fully-digital bridges based on electronic sources and on sampling. The realization of the farad from the QHE is then discussed, presenting, as example, the traceability chain currently adopted by INRIM and other NMIs, based on digitally-assisted transformer bridges and starting from the QHE in the DC regime (section 1.4.2). Finally, the possibility to simplify the chain by means of fully digital bridges and a QHE experiment in the AC regime is described in section 1.4.2.

Electronic generating fully-digital bridges

The development of polyphase generators by means of high-accuracy digital-to-analogue converters (DACs) allowed the generation of arbitrary voltage ratios, which cannot be realized even with the more accurate fixed-ratio transformers. With this novel technology, it became possible the implementation of automatable applications, such as fully-digital voltage ratio impedance bridges.

The simplest design of a fully-digital bridge [135] is the two terminal-pair bridge, where the ratio between two two-terminal-pair impedances is compared with the ratio between two digitally-generated voltages. Then, the bridge is balanced by

adjusting the amplitude and phase of one voltage [136]. The accuracy in the determination of the impedance ratio mainly depends on the agreement between the generators settings and the voltages actually applied to the impedances. It is possible to reduce significantly the error related to the possible asymmetry between the two channels of a dual voltage source by repeating the measurement reversing the position of the two impedances [130, 135]. Further uncertainty components are related to the source non-linearity [137], gain and phase stability [138, 139], and loading effect of the stray admittances [135].

Four terminal-pair fully-digital bridges can be developed by adding further voltage sources to the design [130, 140]. Although some implementations are still based on IVDs for the adjustment of the voltage ratio [138], they can be adopted for the calibration of impedances of different type, like resistance-capacitance [130, 141] or inductance-capacitance [142] comparisons.

These bridges usually operate at frequencies between tens of Hz [141] (or even lower [140]) and 10 kHz [143]. The uncertainty on the generated voltage ratio is usually of few parts in 10^5 [138] or 10^6 [144].

Electronic sampling fully-digital bridges

The calibration of impedances can be performed also with other types of digital bridges, like the three-voltmeter method [145–153] or sampling-based bridges [154–165] whose operation is not based on the ability to generate accurate voltages, but on their accurate measurements implemented with a single digitizer. Therefore, although the two voltages still need to be generated and adjusted, in a sampling-based bridge only the single digitizer needs to be stable during the measurement sequence.

The sampling bridges are employed to directly compare inductance standards to reference resistance standards [154, 157], to determine the dissipation factor of capacitor and the time constant of resistors [155, 156], to compare low value resistors [160, 165] or high value capacitors [166] or, in general, any type of impedances [158, 161, 162, 164].

Realization of the farad from the DC QHE

A number of NMIs developed a traceability chain of the farad from a realization of the ohm obtained by the DC QHE [117, 167–174]. Most of the developed chains require many measurement steps and usually not less than three different transformer-based impedance bridges. The possibility to employ digitally-assisted impedance bridges significantly simplifies the calibration procedure and the chain itself.

Here, as an example, the first complete ohm to farad traceability chain based on digitally assisted bridges is presented. This chain was developed and still employed

at INRIM for the realization of the farad from the DC QHE.

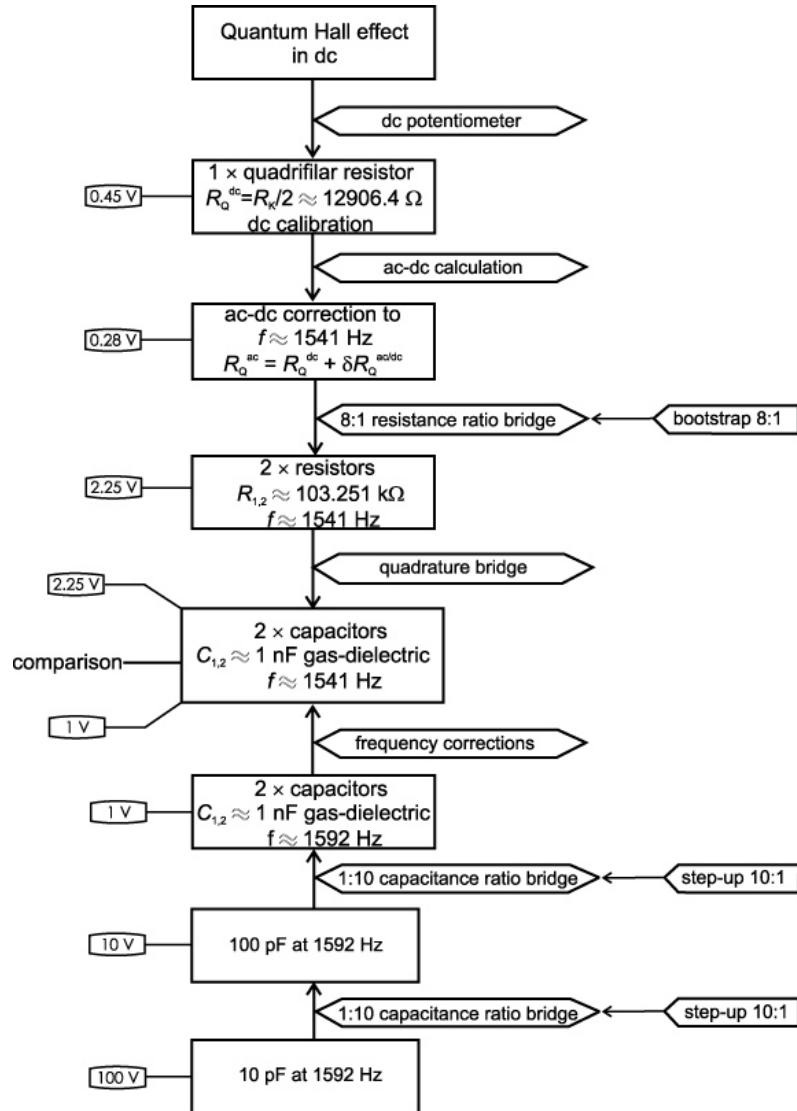


Figure 1.20: Representation of the traceability chain employed at INRIM for the realization of the farad unit from the QHE in the DC regime. Reproduced with permission from [125] ©IOP Publishing. All rights reserved.

Figure 1.20 shows the traceability chain [125], composed of several steps involving a resistance ratio bridge and a quadrature bridge, both digitally-assisted bridges.

As a first step, the QHE is employed to calibrate a quadrifilar resistance standard, whose frequency dependence and reactive parameter are calculable from its geometry [175]. The quadrifilar resistor has nominal value $R_K/2 \approx 12\,906.4\,\Omega$.

Then, a 8:1 resistance ratio bridge is employed to calibrate two resistance standards having nominal value $8 \times R_K/2 \approx 103.251 \text{ k}\Omega$. These resistance standards are then used to calibrate the product of two 1000 pF temperature-controlled gas-dielectric capacitance standards by means of a digitally-assisted quadrature bridge. This kind of bridge, in fact, measures the product of two capacitances in terms of the product of two resistances. Since a comparison of this capacitance standard with the national capacitance standard, maintained at the level of 10 pF, is necessary, a capacitance ratio bridge is employed to perform a scaling up to 1000 pF and the single measurement of the two capacitance standards.

The digitally-assisted impedance bridges has a working frequency of about 1541.4 Hz. The national capacitance standard is instead maintained at 1592 Hz, that is, 10 krad^{-1} . The correction for the frequency shift can be estimated by means of indirect measurements of the frequency dependence.

The estimated relative standard uncertainty of the capacitance determination obtained with this traceability chain is 64×10^{-9} (coverage factor $k = 1$) at 1000 pF.

Realization of the farad from the AC QHE

The AC QHR standards operation at frequency of few kilohertz opened up the way towards the development of quantum standards of impedance directly linked to R_K [176, 177].

A direct realization of the farad from the QHE, in fact, can be realized by calibrating a capacitance directly from two quantum Hall resistance standards by means of a transformer-based quadrature bridge with a relative uncertainty of 6×10^{-9} [178]. This method avoids the additional calibration step of the calculable resistance, employed in the traceability chain introduced in section 1.4.2. However, the method still employs transformer-based bridges that are limited to a few fixed nominal ratios (like 1:1 and 10:1) and require long calibrations at each ratio and frequency.

The pulse-driven Josephson voltage standards [7, 179, 180], generating sine waves with high spectral purity, can be employed to compare arbitrary impedances over a wide range of frequency with the same uncertainty obtained with the transformer-based impedance bridges. Moreover, the ratio of the bridge is defined by two pulse-driven Josephson series arrays that can be adjusted in amplitude and phase so that any kind of impedance can be compared, at frequencies up to 40 kHz [133]. The calibration of a capacitance against an AC QHR standard is thus possible by means of this technology, even though it requires a complex and expensive experiment involving two pulse-driven Josephson voltage standards and one quantum Hall resistance standard. The agreement with the traditionally-performed calibration was found to be of few parts in 10^8 [132].

The employment of fully-digital impedance bridges can simplify a lot the implementation of the realization of the unit farad directly from the AC QHE.

Chapter 2

QHE circuit modelling

As introduced in chapter 1, the units of resistance and impedance can be realized by means of multi-terminal (typically 8 terminals) QHE elements.

The accurate measurement of the QHR requires the rejection of any stray resistance (in DC) or impedance (in AC) due to the contacts and the external leads. A simple four-terminal connection can be sufficient to measure the QHR in the DC regime; more complex connection schemes, usually based on the multiple-connections introduced in section 1.3.2, are required to reject the stray components when several QHE elements are connected in series or parallel [86, 181], as in a QHARS (section 1.3.2), or when the QHR is measured in the AC regime [177].

Therefore, the modelling of electrical connections of single, or several, multi-terminal QHE elements is relevant for electrical metrology.

A QHE element can be accurately modelled by means of the Ricketts and Kemeny [182] or Delahaye [86, 183] equivalent circuits. Then, a four-terminal resistance (or impedance) can be determined by applying Kirchhoff's laws to the chosen model with constraints given by the external connections and by solving the resulting equations. This analysis was applied to double- and triple-series connections of single and twin devices in the DC regime [86, 181], and then extended in the AC regime [177]. Such analytical calculations can be tedious and error-prone, and numerical solutions can have issues of convergence [184]. Therefore, only few connection schemes of known practical relevance have been analyzed in full in this way.

An alternative general approach [9] for modelling the electrical behaviour of multi-terminal QHE elements with external connections is based on the formalism of the indefinite admittance matrix, introduced in section 1.1, and can be implemented by analytical or numerical software tools, including the popular SPICE circuit analysis software [185].

This chapter discusses this analysis method and its applications. Section 2.1 introduces the single QHE element model. Section 2.2 presents the model of a QHARS in the DC regime. Section 2.3 presents a general and systematic procedure

for the error modelling of QHARSs, based on the previously discussed analysis technique. As an example, this procedure is applied to the characterization of a $1\text{ M}\Omega$ QHARS fabricated by the NMIJ. Finally, section 2.5 provides a SPICE macro-model for a QHE element, discussing its applications to the simulation of networks of QHE elements.

2.1 Circuit models of QHE elements

As discussed in section 1.1.2, in circuit theory, an M -terminal element can be considered as a black-box interacting with the environment only through its M terminals and can be completely characterized by its external behaviour described by the set of admissible terminal voltage-current pairs [186, 187]. Therefore, if two M -terminal elements have the same external behaviour, they are *equivalent* from the circuit theory point of view.

An electric circuit composed of several interconnected elements can be itself turned into an M -terminal element by connecting terminals to M selected nodes of the circuit, and can be thus considered as its *circuit model*, *macromodel* or *equivalent circuit*.

2.1.1 Ideal QHE device

According to its external behaviour, it is possible to classify an ideal QHE element as:

- *ideal clockwise (cw) M -terminal QHE element* with Hall resistance $R_{\text{H}} > 0$: an element whose terminal voltages and currents are related by

$$R_{\text{H}} j_m = e_m - e_{m-1}, \quad m = 1, \dots, M, \quad (2.1)$$

with $e_0 \equiv e_M$;

- *ideal counterclockwise (ccw) M -terminal QHE element*: an element whose terminal voltages and currents are related by

$$R_{\text{H}} j_m = e_m - e_{m+1}, \quad m = 1, \dots, M, \quad (2.2)$$

with $e_{M+1} \equiv e_1$.

The above sets of equations (2.1) and (2.2) are, indeed, a consequence of the QHE phenomenology, but can also be derived theoretically on the basis of the Landauer-Büttiker formalism (see e.g. [45, section 16.3] and references therein). A real QHE device operating at appropriate values of temperature and magnetic flux density can be modelled, with a certain approximation, either as an ideal cw or an

ideal ccw element depending on the orientation of the magnetic field applied to the device and on the type of the majority charge carriers.

Ideal QHE elements are *memoryless*, because 2.1 and 2.2 relate terminal voltages and currents at the same time instant, *passive*, since they dissipate power, and *nonreciprocal* [185, 188].

The sets of equations (2.1) and (2.2) can be rewritten in the matrix form (1.12) of section 1.1.2 as [9]

$$\mathbf{J} = \bar{\mathbf{Y}}_i \mathbf{E}, \quad (2.3)$$

where $\mathbf{J} = (J_1, \dots, J_M)^T$ and $\mathbf{E} = (E_1, \dots, E_M)^T$ are column vectors, and where the $M \times M$ indefinite admittance matrix $\bar{\mathbf{Y}}_i$ associated to the ideal QHE element is either (cw QHE element)

$$\bar{\mathbf{Y}}_i = \frac{1}{R_H} \begin{pmatrix} 1 & 0 & \cdots & 0 & -1 \\ -1 & 1 & 0 & \cdots & 0 \\ & \ddots & \ddots & \ddots & \vdots \\ 0 & \cdots & -1 & 1 & 0 \\ 0 & 0 & \cdots & -1 & 1 \end{pmatrix}, \quad (2.4)$$

or (ccw QHE element)

$$\bar{\mathbf{Y}}_i = \frac{1}{R_H} \begin{pmatrix} 1 & -1 & 0 & \cdots & 0 \\ 0 & 1 & -1 & \ddots & 0 \\ \vdots & \ddots & \ddots & \ddots & \vdots \\ 0 & \cdots & 0 & 1 & -1 \\ -1 & 0 & \cdots & 0 & 1 \end{pmatrix}. \quad (2.5)$$

2.1.2 Contact resistances

When interconnecting N QHE elements, the contact resistances of each element terminal should be taken into account. Let R_{nm}^T be the m th terminal resistance of the n th QHE element. The set of equations (2.1) and (2.2) can then be completed as [9]

$$\mathbf{D}_n \mathbf{J} = \bar{\mathbf{Y}}_i \mathbf{E} \quad (2.6)$$

or, equivalently,

$$\mathbf{J} = \mathbf{D}_n^{-1} \bar{\mathbf{Y}}_i \mathbf{E}, \quad (2.7)$$

where $\bar{\mathbf{Y}}_i$ is either (2.4) for cw QHE elements or (2.5) for ccw QHE elements. Respectively, \mathbf{D}_n for the n th QHE element is either (cw QHE element)

$$\mathbf{D}_n = \begin{pmatrix} 1 + \frac{\epsilon_{n1}}{2} & 0 & \cdots & -\frac{\epsilon_{nM}}{2} \\ -\frac{\epsilon_{n1}}{2} & 1 + \frac{\epsilon_{n2}}{2} & \cdots & 0 \\ \vdots & \ddots & \ddots & \vdots \\ 0 & \cdots & -\frac{\epsilon_{n(M-1)}}{2} & 1 + \frac{\epsilon_{nM}}{2} \end{pmatrix} \quad (2.8)$$

or (ccw QHE element)

$$\mathbf{D}_n = \begin{pmatrix} 1 + \frac{\epsilon_{n1}}{2} & -\frac{\epsilon_{n2}}{2} & \cdots & 0 \\ 0 & 1 + \frac{\epsilon_{n2}}{2} & -\frac{\epsilon_{n3}}{2} & \vdots \\ \vdots & \ddots & \ddots & 0 \\ -\frac{\epsilon_{n1}}{2} & 0 & \cdots & 1 + \frac{\epsilon_{nM}}{2} \end{pmatrix}, \quad (2.9)$$

being $\epsilon_{nm} = R_{nm}^T/(R_H/2)$ the resistance R_{nm}^T normalized to $R_H/2$, in agreement with the convention typically employed in literature [9, 182]. Because of (2.7), the indefinite admittance matrix of the n th QHE element is

$$\bar{\mathbf{Y}}_n = \mathbf{D}_n^{-1} \bar{\mathbf{Y}}_i. \quad (2.10)$$

In analytical calculations, being \mathbf{D}_n typically very close to the identity matrix (see (2.8) and (2.9)), \mathbf{D}_n^{-1} can be in most cases approximated as a Taylor series expansion up to the appropriate order in $\epsilon_1, \dots, \epsilon_m$.

2.2 Analysis of a QHARS

A QHARS composed of N interconnected QHE elements, in the same quantized state and with M terminals each, interconnected by L leads and having K externally accessible nodes can be itself analyzed by means of the indefinite admittance matrix formalism to obtain the QHARS four terminal resistance $R_{ab,cd}^Q$ for certain designated nodes a, b, c and d (see (1.9)). For ease of notation, here and in the following sections, the symbols n, m, l and k denote indices running from 1 to, respectively, N, M, L and K .

The linear matrix relationship (2.3) between node currents and applied voltages can be written as

$$\mathbf{J} = \bar{\mathbf{Y}}^Q \mathbf{E}, \quad (2.11)$$

where $\bar{\mathbf{Y}}^Q$ is the $K \times K$ indefinite admittance matrix associated to the QHARS.

The QHARS is composed of QHE and resistive elements, the latter modelling the contact resistances and the interconnecting leads. The matrix $\bar{\mathbf{Y}}^Q$ is obtained by combining two more elementary matrices: the indefinite admittance matrix $\bar{\mathbf{Y}}$ defined in (2.10) is extended to a block matrix to represent all the *unconnected* QHE and resistive elements; an interconnection matrix \mathbf{A} is constructed to represent the topology of the network, that is, the way in which nodes join the terminals of the elements.

The indefinite admittance matrix $\bar{\mathbf{Y}} = \bar{\mathbf{Y}}(R_H, \{\epsilon_{nm}\}, \{\delta_l\})$ is thus a matrix of order $NM + 2L$, equal to the total number of element terminals, depending on:

- R_H , common to all QHE elements;

- $\epsilon_{nm} = R_{nm}^T / (R_H/2)$, the m th terminal resistance R_{nm}^T of the n th QHE element normalized to $R_H/2$;
- $\delta_l = R_l^W / (R_H/2)$, the resistance R_l^W of the l th lead normalized to $R_H/2$.

The resulting block diagonal matrix $\bar{\mathbf{Y}}$, in which each block represents a single element of the QHARS and the QHE elements are listed first, is

$$\bar{\mathbf{Y}} = \begin{pmatrix} \mathbf{D}_1^{-1} \bar{\mathbf{Y}}_1 & \mathbf{0} & \dots & \mathbf{0} & \dots & \mathbf{0} \\ \mathbf{0} & \ddots & \mathbf{0} & \vdots & \ddots & \vdots \\ \vdots & \mathbf{0} & \mathbf{D}_N^{-1} \bar{\mathbf{Y}}_N & \mathbf{0} & \dots & \mathbf{0} \\ \mathbf{0} & \dots & \mathbf{0} & \mathbf{G}_1 & \mathbf{0} & \dots \\ \vdots & \ddots & \vdots & \mathbf{0} & \ddots & \mathbf{0} \\ \mathbf{0} & \dots & \mathbf{0} & \vdots & \mathbf{0} & \mathbf{G}_L \end{pmatrix}. \quad (2.12)$$

The n th QHE element is described by $\mathbf{D}_n^{-1} \bar{\mathbf{Y}}_n$, being \mathbf{D}_n and $\bar{\mathbf{Y}}_n$, respectively, (2.8) and (2.4) for the n th cw QHE element, and (2.9) and (2.5) for the n th ccw QHE element.

The resistance of the l th lead is represented by the matrix \mathbf{G}_l , which can be written as [189]

$$\mathbf{G}_l = \frac{2}{R_H} \begin{pmatrix} 1/\delta_l & -1/\delta_l \\ -1/\delta_l & 1/\delta_l \end{pmatrix}. \quad (2.13)$$

When the elements are interconnected, their terminal voltages are limited by constrains, which can be expressed in matrix form by means of a matrix \mathbf{A} composed of $NM + 2L$ rows and K columns. The matrix \mathbf{A} , representing the transformation from the node voltages to the terminal voltages, is composed of 1's and 0's so that each column represents a node and a 1 in each row corresponds to the terminal joined by the associated node.

The QHARS indefinite admittance matrix $\bar{\mathbf{Y}}^Q$ can hence be obtained from $\bar{\mathbf{Y}}$ and \mathbf{A} as [9, 10]

$$\bar{\mathbf{Y}}^Q = \mathbf{A}^T \bar{\mathbf{Y}} \mathbf{A}. \quad (2.14)$$

The QHARS four-terminal resistance $R_{ab,cd}^Q$ can then be directly calculated from (1.13) as

$$R_{ab,cd}^Q = \text{sgn}(c - d) \text{sgn}(a - b) \frac{\bar{\mathbf{Y}}_{cd;ab}^Q}{\bar{\mathbf{Y}}_{11}^Q}. \quad (2.15)$$

2.3 Application: the QHARSmachine

In a QHARS, the nominal value of interest R_{nom} is approximated by a suitable fraction $R_{\text{nom}}^Q = (p/q)R_H \approx R_{\text{nom}}$, being p and q positive integers.

Because of the connections between the QHE elements, contact and lead resistances cause deviations from the quantized values. As introduced in section 1.3.2, multiple connections of the individual QHE elements [86, 90, 92] reject, to a large extent, these deviations.

To estimate the deviations caused by these stray parameters, a model of the entire QHARS, including the set of estimated contact and lead resistances of the fabricated chip, need to be solved.

The analysis method presented in the previous section allows one to model QHARSs of arbitrary complexity in the DC regime. A systematic implementation of this modelling procedure was developed as a Mathematica¹ notebook (QHARSmachine [1]) to allow fast calculations with arbitrary precision arithmetic. The complete Mathematica notebook and an example of the stray parameters spreadsheet are available in appendix A.1 and in the online repository [191]. The program LTspice² is used only as a simple, off-the-shelf schematic editor. The LTspice graphical symbols used in this chapter are available online [191].

The procedure evaluates the deviation of the modelled resistance from $R_{\text{nom}}^{\text{Q}}$ as a simulated probability distribution, from which the expected value and confidence intervals can be computed.

Figures 2.1 and 2.2 present schematically the workflow adopted for the analysis and the applications employed.

An electrical schematic is required to faithfully represent the QHARS, including the QHE elements and lead resistances. A portion of an example schematic drawn with the LTspice schematic editor is shown in figure 2.3. A comment line specifying the nodes a, b, c, d of the four-terminal resistance $R_{ab,cd}^{\text{Q}}$ and the parameter $R_{\text{nom}}^{\text{Q}}/R_{\text{H}} = p/q$ has to be inserted in the schematic for the simulation.

The electrical schematic is then saved in a file and imported by the QHARSmachine, which runs successively the *converter* and *solver* blocks, as shown in figure 2.2.

2.3.1 Converter

The converter extracts the parameters a, b, c, d and p/q from the comment line of the LTspice schematic, derives the parameters N, M and L , and constructs the interconnection matrix \mathbf{A} .

2.3.2 Solver

The analysis method developed in section 2.2 is implemented by the solver, as shown in detail in figure 2.2, to obtain a Monte Carlo simulation [193] of the

¹Wolfram Mathematica 11 [190]

²Linear Technology Corporation LTspice XVII [192]

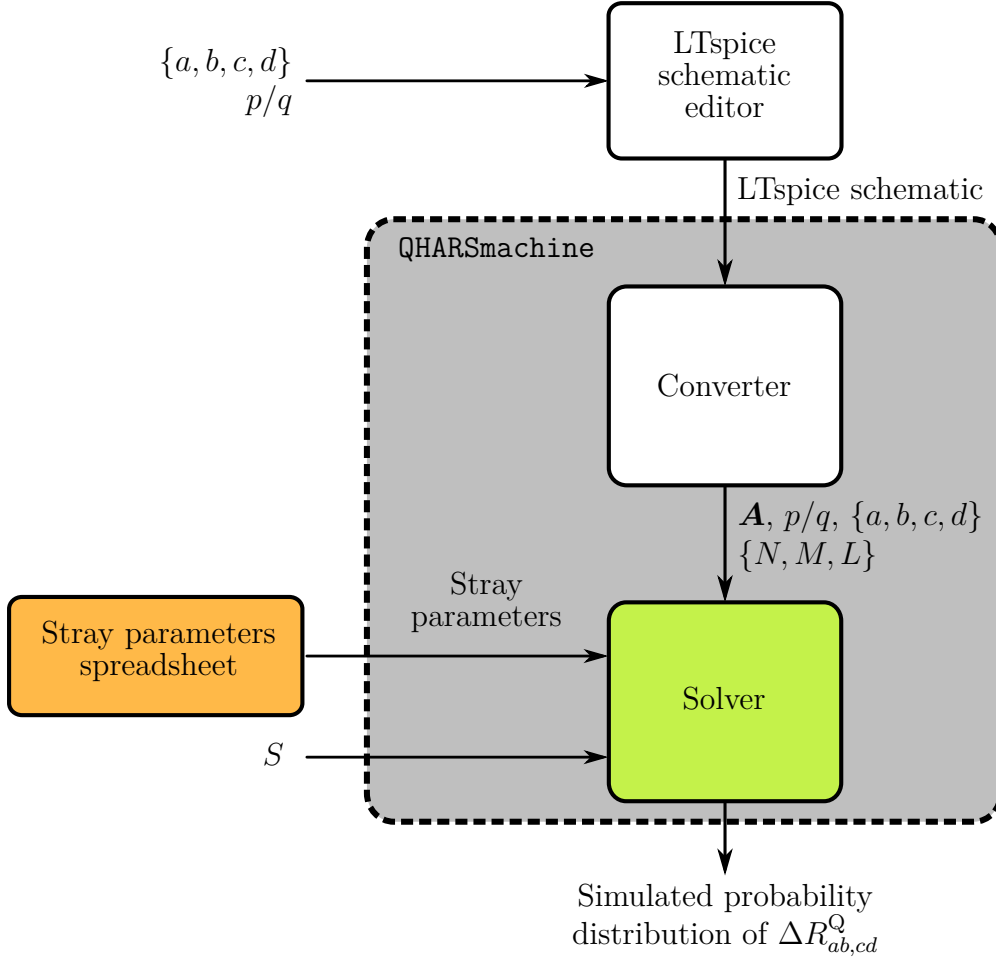


Figure 2.1: Workflow of the modelling procedure.

probability distribution of the deviation $\Delta R_{ab,cd}^Q = R_{ab,cd}^Q - R_{\text{nom}}^Q$.

The endpoints $[\epsilon_{nm}^{\min}, \epsilon_{nm}^{\max}]$, $[\delta_l^{\min}, \delta_l^{\max}]$ of the $NM + L$ experimental stray parameter distributions, reported in a spreadsheet, are imported by the Monte Carlo subblock to generate a random sample of length S extracted from an $(NM + L)$ -dimensional multivariate uniform distribution³ and composed of the $\{\epsilon_{nm;s}\}_{s=1,\dots,S}$ and $\{\delta_{l;s}\}$ sequences. The multivariate random sample of the NM terminal resistances and of the L lead resistances are thus obtained.

The sequences of matrices $\{\bar{\mathbf{Y}}_s\}$ and $\{\bar{\mathbf{Y}}_s^Q\}$, and the sequence of deviations $\{\Delta R_{ab,cd;s}^Q\}$ which represents the simulated probability distribution of $\Delta R_{ab,cd}^Q$ are then constructed by the solver, according to (2.12), (2.14) and (2.15).

³The implementation here reported is limited to uniform distributions, but it can be generalized to other distributions.

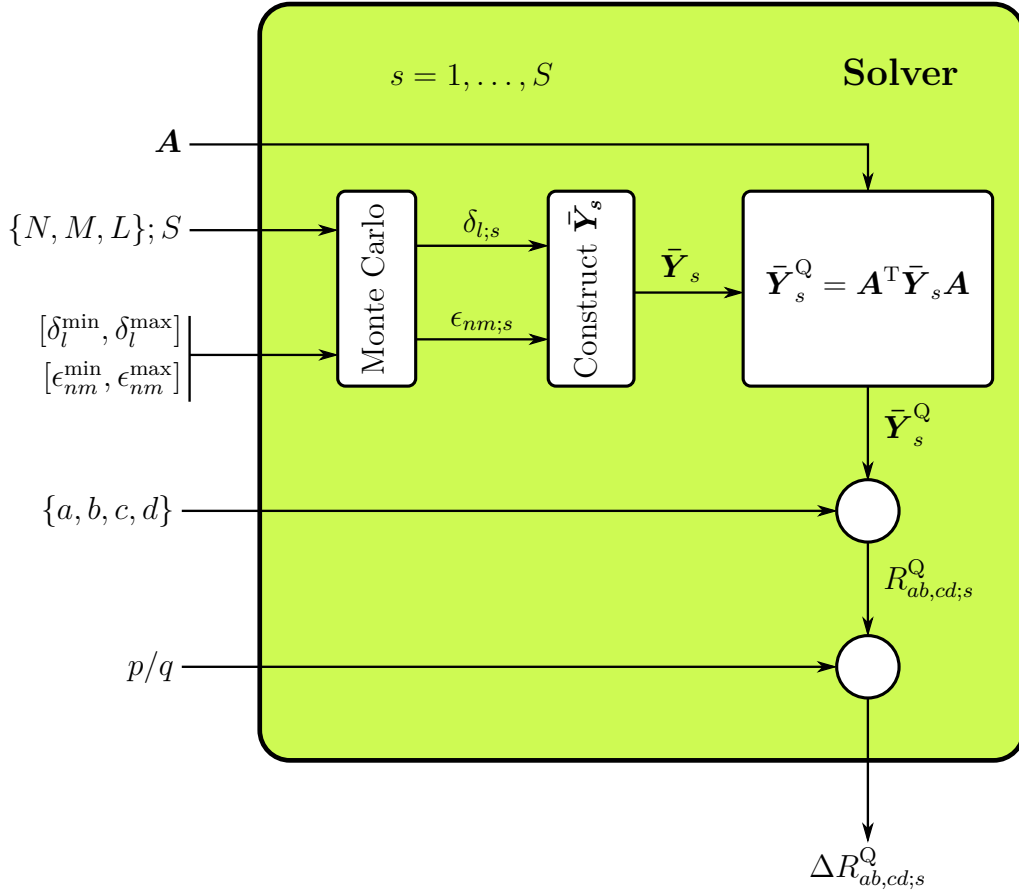


Figure 2.2: Detail of the solver of figure 2.1.

2.3.3 Example: analysis of a 1 M Ω QHARS

As an example, a QHARS developed by the National Metrology Institute of Japan (NMIJ) [88, 194] with nominal resistance value $R_{\text{nom}}^Q = (10150/131)R_H = (1 - 16.4 \times 10^{-9}) \text{ M}\Omega$ [195] is here analyzed, detailing the identification of its stray parameters.

The device

Figure 2.4 shows the 1 M Ω QHARS, fabricated on a 8×8 mm GaAs/AlGaAs chip. It is composed of 88 QHE elements interconnected with Au-Ti leads by means of triple connections [86]. The leads are arranged in two layers to avoid crossings. The QHARS design, developed with the method presented in [90], and based on the decomposition $p/q = 10150/131 = 77 + 63/131$, combines 77 QHE elements in series and 11 elements that are arranged to obtain the fraction 63/131. The QHARS fabrication is described in full details in [88].

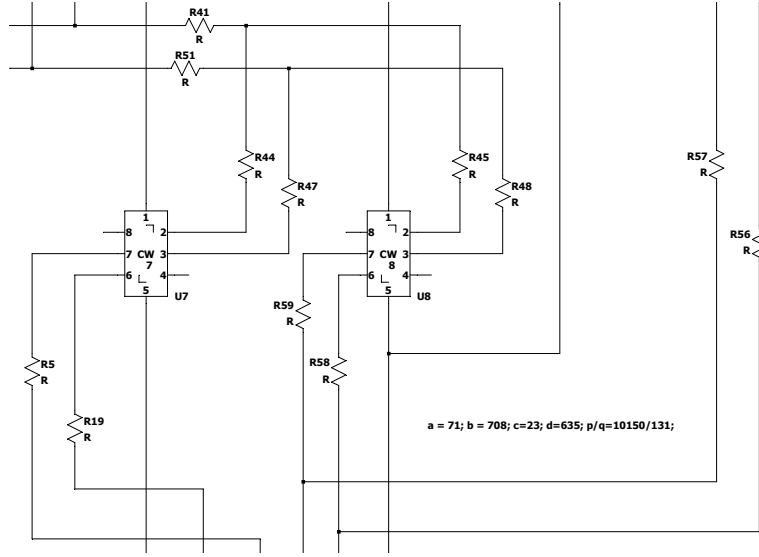


Figure 2.3: A portion of an example schematic produced with the LTSpice editor. The n th QHE element is designated by U_n . The numbers from 1 to 8 within the symbol designate the index m of the corresponding terminal. The CW label identifies the clockwise element. Each resistance, identified with the index l , represents a lead connection between two nodes. The comment line $a=71$; $b=708$; $c=23$; $d=635$; $p/q=10150/131$; specifies the nodes a, b, c and d , and the fraction p/q .

2.3.4 Identification of the stray parameters

The solver, described in section 2.3.2, performs the Monte Carlo analysis on the basis of the distributions of the stray resistances, which are here estimated.

The stray resistances can be decomposed into leads resistances, pad resistances and contact resistances to the 2DEG, as shown in figure 2.5. Contact and pad resistances compose the terminal resistances. A pad is composed of five meanders [88] and, for the cw QHE elements employed in this QHARS, the current flows mainly through the larger one [196] (in the example of figure 2.5, the bottom meander of the left pad is the larger one). In the QHE regime, from the QHE element the current crosses only that meander contact edge and then flows through the whole pad from edge to edge. For this reason, the resistance of this path, that is, the pad resistance, is counted in the evaluation of the current terminal resistance. A lead is any trace segment connecting two pad edges, two junctions or a junction and a pad edge. As a result, possibly different probability distributions can be assumed for each stray resistances component.

The contact, pad and lead resistances were estimated from experimental data, obtained from the characterization of purpose-built test devices and probes.

The insulation resistances between the two layers of the QHARS device are of the order of tens of teraohm [88]; since the crossing leads are approximately

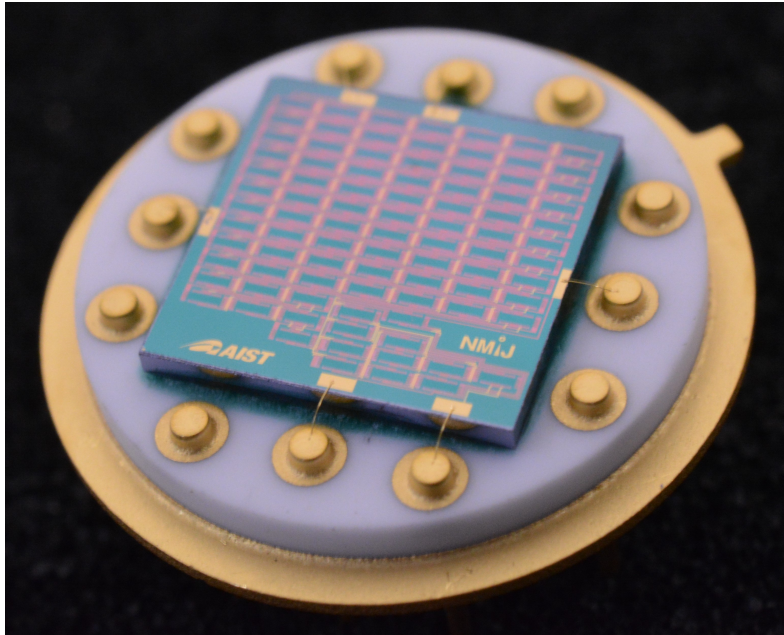


Figure 2.4: 1 M Ω QHARS device, mounted on a TO-8 chip carrier. Reproduced with permission from Marzano et al. [1] ©IOP Publishing. All rights reserved.

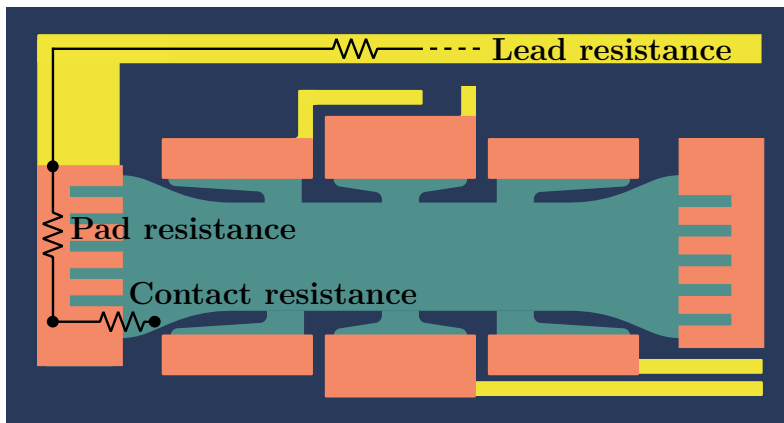


Figure 2.5: The stray resistances are decomposed into lead resistance (yellow), pad resistance (pink) and the contact resistance between the pad and the QHE element (light blue). Reproduced with permission from Marzano et al. [1] ©IOP Publishing. All rights reserved.

equipotential, the effect of insulation resistances can be neglected in this case.

The measurement results are collected in a spreadsheet, which is then imported by the `QHARSmachine` to perform the Monte Carlo analysis. Two example portions of the spreadsheet, reporting the measured lengths and the estimated lead and contact resistances, are shown in figure 2.6 on the facing page.

#R	Width (m)	Length (m)	$R_{\text{cav}}(\Omega)$	$R_{\text{up}}(\Omega)$	δ_{cav}	δ_{up}	description	$V=0/1$	$W_{\text{pad}}(\text{m})$	$L_{\text{pad}}(\text{m})$	$W_{\text{pad}}(\text{m})$	$L_{\text{pad}}(\text{m})$	R_{cav}	R_{up}	R_{cav}	R_{up}	N_{times}	prepad(1=no,0=yes)	rho2D_Vmin=0.0781765210	rho2D_Vmax=0.0938118250	rho2D_lmin=0.0764163840	rho2D_lmax=0.081431710	RK=25812.8070		
1	0.00033	1.62000E-04	0.4126847360	0.43817312340	3.20E-05	3.40E-05	currentDevice1_63/131	1	0	0	0	0	0	0	0	0	0	0	1	rho2D_Vmin=0.0781765210	rho2D_Vmax=0.0938118250	rho2D_lmin=0.0764163840	rho2D_lmax=0.081431710	RK=25812.8070	
2	0.00033	1.91000E-04	0.48651764480	0.51661152203	3.77E-05	4.00E-05	CurrentDevice2-3_63/131	1	0	0	0	0	0	0	0	0	0	0	0	1					
3	0.00033	1.37000E-04	0.34896815360	0.37055381423	2.70E-05	2.87E-05	CurrentDevice3-4_63/131	1	0	0	0	0	0	0	0	0	0	0	0	1					
4	0.00028	8.20000E-04	0.22220366979	0.23594822773	1.72E-05	1.83E-05	padDevice2_63/131	1	0	0	0	0	0	0	0	0	0	0	0	1					
5	0.00002	1.225984E-03	4.71343494758	5.65612192504	3.65E-04	4.38E-04	CentralDoubleles(device7-10_63/131)	0	0	0	0	0	0	0	0	0	0	2	0	1					
6	0.00024	8.92500E-04	0.27951484721	0.29680442671	2.17E-05	2.30E-05	CurrentDevice1-6_63/131	1	0	0	0	0	0	0	0	0	0	0	0	1					
7	0.00024	9.00000E-05	0.02824053742	0.02998737492	2.19E-06	2.32E-06	CurrentDevice7-2_63/131	1	0	0	0	0	0	0	0	0	0	0	0	1					
8	0.00033	2.00467E-04	0.45968785238	0.48812215470	3.56E-05	3.78E-05	CurrentDevice2-8_63/131	1	0	0	0	0	0	0	0	0	0	0	0	1					
9	0.00033	1.19232E-03	3.01163043428	3.19791686711	2.33E-04	2.48E-04	CurrentDevice3-8_63/131	1	0	0	0	0	0	0	0	0	0	0	0	1					
10	0.00033	1.10300E-03	2.78410359040	2.95631619677	2.16E-04	2.29E-04	CurrentDevice4-5_63/131	1	0	0	0	0	0	0	0	0	0	0	0	1					
11	0.00024	9.00000E-05	0.02818733344	0.02993087998	2.18E-06	2.32E-06	CurrentDevice6-9_63/131	1	0	0	0	0	0	0	0	0	0	0	0	1					
12	0.00024	9.00000E-05	0.02818559604	0.02992909511	2.18E-06	2.32E-06	CurrentDevice7-10_63/131	1	0	0	0	0	0	0	0	0	0	0	0	1					
13	0.00033	1.18697E-03	2.99798578966	3.18342822379	2.32E-04	2.47E-04	CurrentDevice8-10_63/131	1	0	0	0	0	0	0	0	0	0	0	0	1					
14	0.00034	6.00000E-05	0.02818637115	0.02993085816	2.18E-06	2.32E-06	CurrentDevice10-11_63/131	1	0	0	0	0	0	0	0	0	0	0	0	1					
15	0.00033	3.213095E-03	3.07981767543	3.27032187608	2.39E-04	2.53E-04	CurrentDevice9-11_63/131	1	0	0	0	0	0	0	0	0	0	0	0	1					
16	0.00033	3.03000E-03	7.59069414400	8.06022165267	5.88E-04	6.23E-04	CurrentDevice5-11_63/131	1	0	0	0	0	0	0	0	0	0	0	0	1					
17	0.00002	2.20438E-04	0.76576094243	0.81312760227	5.93E-05	6.30E-05	CurrentDevice17_63/131	1	0	0	0	0	0	0	0	0	0	0	0	1					

Contact Type	$R_{\text{low}}(\Omega)$	$R_{\text{up}}(\Omega)$	ϵ_{low}	ϵ_{up}
I terminal	2.04E-01	3.06E-01	1.58E-05	2.37E-05
Lateral V terminal	2.00E-01	2.00E+00	1.55E-05	1.55E-04
Central V terminal	2.00E-01	2.00E+00	1.55E-05	1.55E-04

Figure 2.6: Two example portions of the spreadsheet containing the experimental stray parameters distributions. The first example reports the measurements of lead resistances, the second the measurements of contact resistances (the number of digits in the columns is not significant).

Lead resistances

Different processes were adopted to fabricate *current leads*, connected to the current terminals of the QHE elements, and *voltage leads*, connected to the voltage terminals [88].

The lead resistances are assumed to be uniformly distributed. Their values can be estimated, depending on their dimensions, from the measured resistivities at 4.2 K, since the resistivity of gold can be considered approximately constant for lower operating temperatures [197].

The resistivity of current leads was estimated from measurements at room temperature on test devices with different lead widths and lengths fabricated next to the QHARS (figure 2.7). The dependence of the test pattern resistance on length and temperature is reported in figure 2.8. The dependence of the resistivity on the lead width at room temperature, probably due to the process tolerances, is in figure 2.9.

Current leads are 30 μm wide; the resistivity was obtained by extrapolating from the data of figure 2.9 the room temperature resistivity at a width of 30 μm , and by scaling this at a temperature of 4.2 K from the data of figure 2.8.

The current lead lengths, known from the QHARS layout, need a correction for the presence of corners. The comparison between the calculated and measured resistance values produces an estimated 10 μm reduction of the effective length $L_{\text{lead,eff}}$ for each corner, so that $L_{\text{lead,eff}} = L_{\text{lead}} - N_{\text{corners}} \times 10 \mu\text{m}$, being L_{lead} the measured lead length and N_{corners} the number of corners along the lead. This result was confirmed by a finite element analysis of the current distribution around the corners (see figure 2.10).

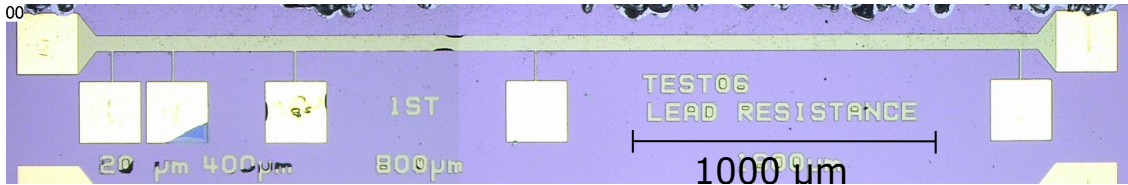


Figure 2.7: Test device with a 50 μm wide lead. Reproduced with permission from Marzano et al. [1] ©IOP Publishing. All rights reserved.

The relative standard uncertainty of 1.7×10^{-2} is assigned to the resistances of the current leads, evaluated by comparing calculated and measured resistance values at room temperature, and by considering a possible contribution of the magnetoresistance effect in the metallic interconnections. The magnitude of this effect depends on the ratio of the resistivities at 300 K and 4.2 K at zero magnetic field [198], which is related to the level of impurities in the metal. Since this ratio is about 2 for the leads (figure 2.8), from the available literature [198–200] one can infer an effect of the order of percent at most.

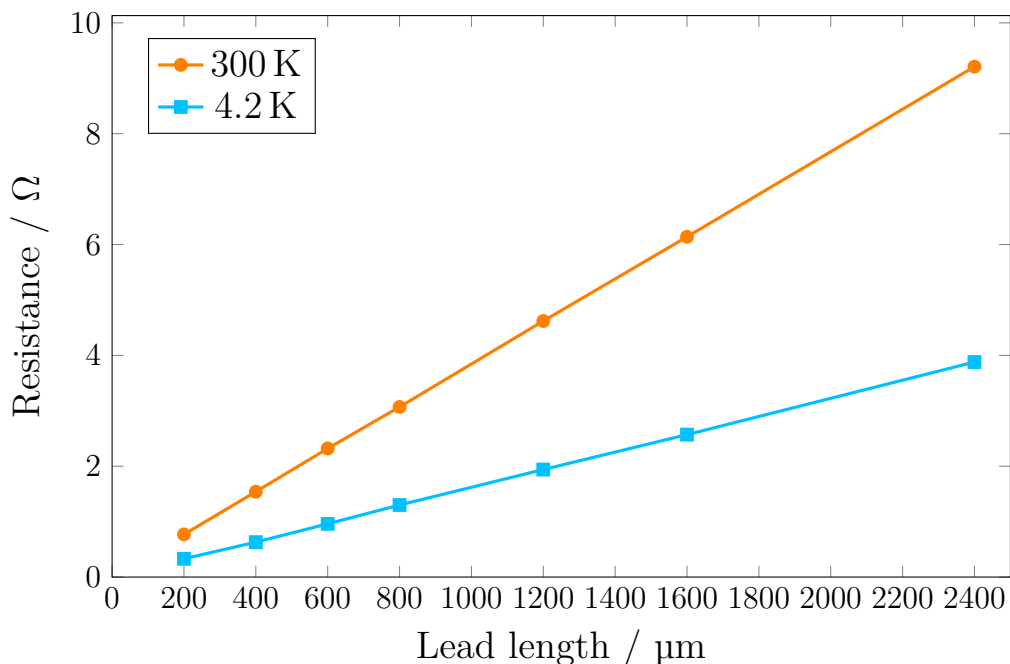


Figure 2.8: Dependence of the test pattern resistance on length and temperature. The orange (●) curve represents the measurements at 300 K; the lightblue (■), the measurements at 4.2 K.

At the time of the fabrication, no test pattern was designed for the voltage leads. The resistivity of the voltage leads was therefore estimated from their structure [88] to be greater than or equal to the current lead resistivity, with a relative standard uncertainty of 5.8×10^{-2} .

Pad resistances

A single meander resistance was measured repetitively at room temperature (about 0.2Ω), and then scaled at 4.2 K as described in section 2.3.4, to estimate the pad resistance, which is about 0.25Ω at 4.2 K. However, the relative standard uncertainty of the pad resistance is assumed to be of 1.2×10^{-1} , because of the not accurately known current distribution in the pad.

Contact resistances

Figure 2.11 shows a device composed of a number of QHE elements with the same size of those employed in the $1 \text{ M}\Omega$ QHARS. This device was employed to estimate the yield ratio of the contact resistance to the 2DEG. QHE elements of 5 different shapes, described in [88], are represented in the device. The $1 \text{ M}\Omega$ QHARS employs the contact shape called type A in [88], for which the measured resistance of

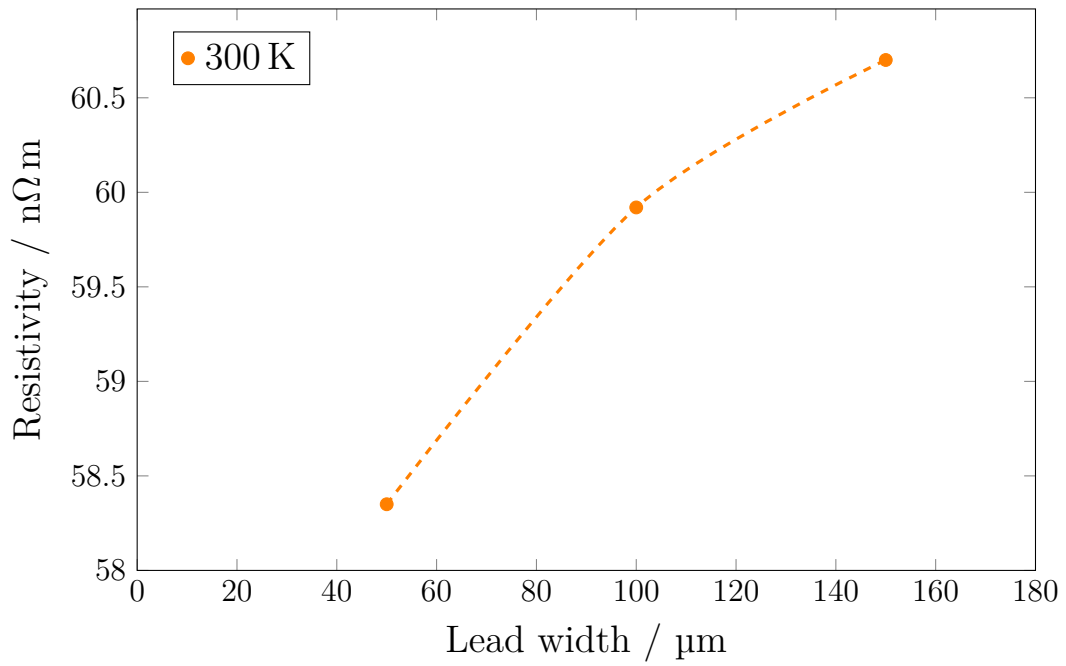


Figure 2.9: Dependence of the resistivity on the lead width at room temperature.

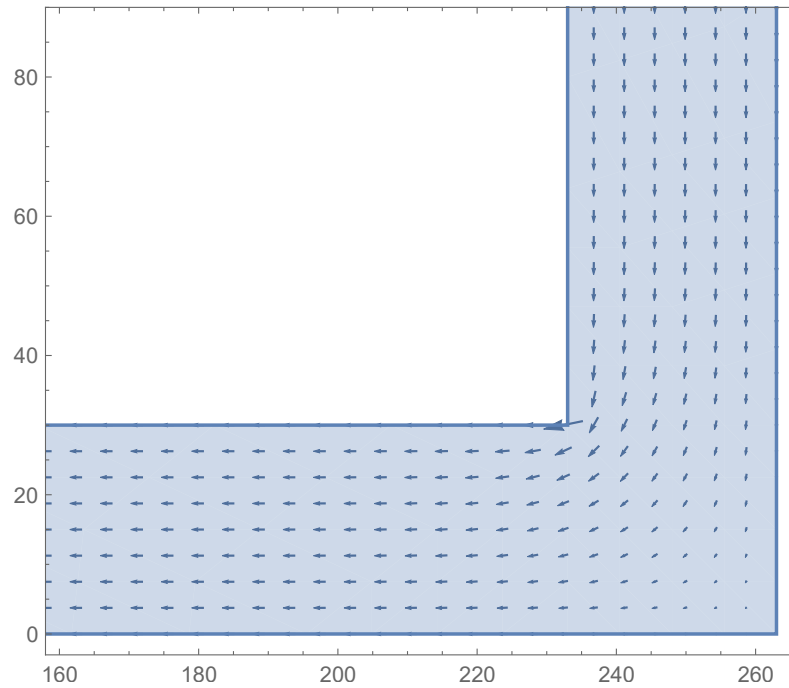


Figure 2.10: Current distribution around a current lead corner obtained with a finite element analysis. The distances are measured in micrometers.

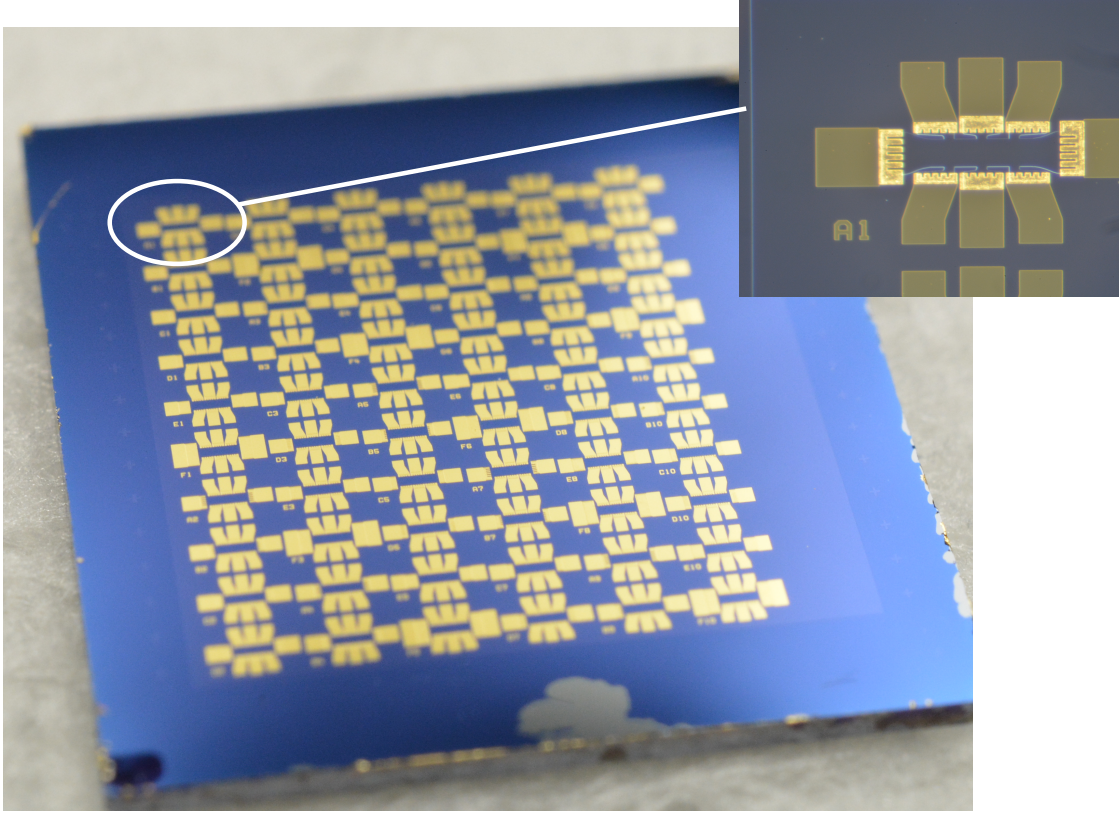


Figure 2.11: Device fabricated for the yield ratio test of contact resistance. Reproduced with permission from [1] ©IOP Publishing. All rights reserved.

the current contacts ranged from $2 \text{ m}\Omega$ to $8.5 \text{ m}\Omega$; the voltage contacts, not directly measured, were assumed to be equal to the highest measured contact resistance on the whole device, that is, a resistance range from $2 \text{ m}\Omega$ to 2Ω . The probability distributions of the contact resistances were assigned according to these ranges.

2.3.5 Results

Figure 2.12 shows the probability distribution of the relative deviation $\Delta R_{ab,cd}^Q / R_{\text{nom}}^Q$ for the $1 \text{ M}\Omega$ QHARS, with a sample size $S = 1000$. The mean value of the distribution is 3.5×10^{-11} with a standard deviation of 10^{-12} .

The upper bond of the relative deviation for the series of the 77 QHE elements can be calculated from [88, equation 5] as

$$\left| \frac{\Delta R_{77}^Q}{R_{\text{nom},77}^Q} \right| < \frac{77-1}{4 \times 77} \left(\frac{1}{2} \max_l \{\delta_l\} + \max_{n,m} \{\epsilon_{nm}\} \right)^3 \quad (2.16)$$

$$\approx 6.7 \times 10^{-10},$$

being $R_{\text{nom},77}^{\text{Q}} = 77R_{\text{H}}$ the nominal resistance of the series and the term within parentheses the maximum stray resistance of an interconnection between two QHE elements.

The simulated relative deviation is compatible with the calculated upper bond, together with the experimental result shown in [88, 201], albeit such a small deviation is beyond the possibility of an experimental check.

In addition, a relative deviation from the nominal value $(63/131)R_{\text{H}}$ of a few parts in 10^{11} resulted from the individual analysis of the arrangement of the 11 elements corresponding to the resistance $(63/131)R_{\text{H}}$ with the QHARSmachine. This means that, more generally, small deviations for comparable values of the stray resistances can be expected even for QHARS of lower resistance.

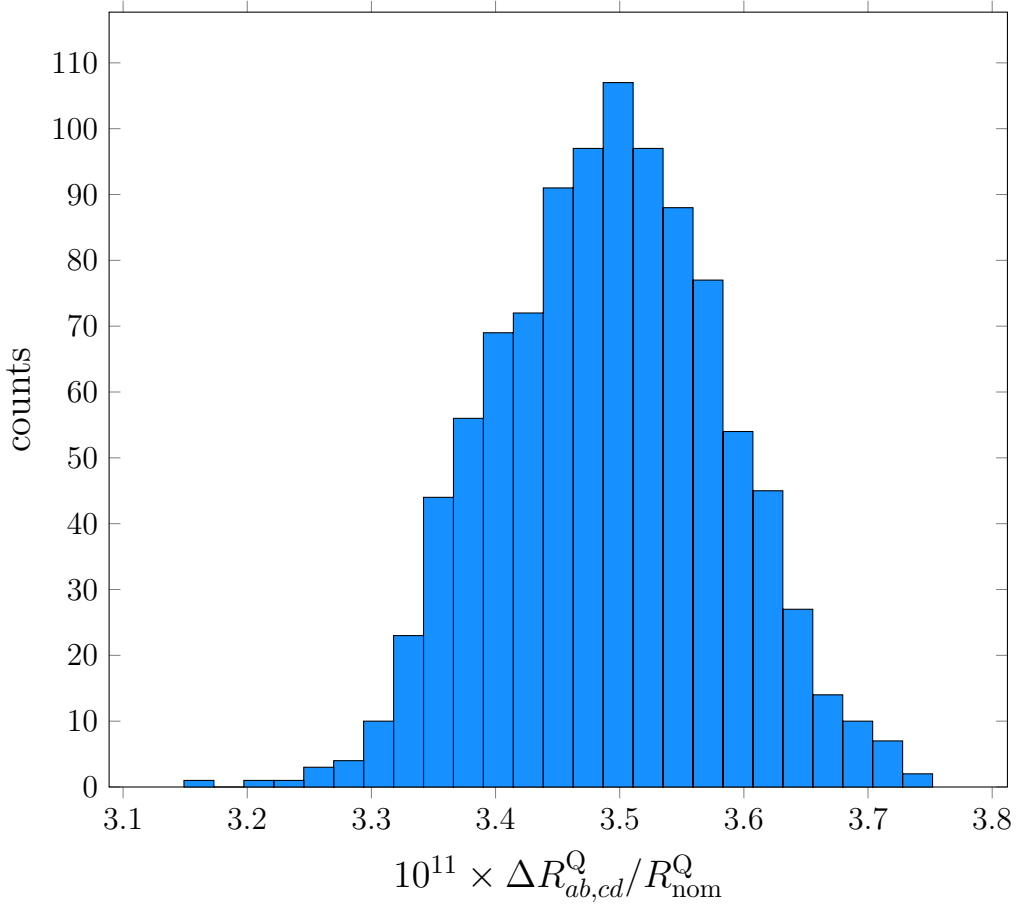


Figure 2.12: Simulated probability distribution of the relative deviation $\Delta R_{ab,cd}^{\text{Q}}/R_{\text{nom}}^{\text{Q}}$ of the $1\text{M}\Omega$ QHARS. The distribution is obtained with a sample size $S = 1000$. The mean value of the distribution is 3.5×10^{-11} with a standard deviation of 10^{-12} . Reproduced with permission from Marzano et al. [1] ©IOP Publishing. All rights reserved.

2.4 Remarks

The development of new design of QHARS can be improved by exploiting the method of analysis described in section 2.2 and the application `QHARSmachine` described in section 2.3.

First, by simulating different interconnection layouts, it is possible to evaluate which one yields the lowest deviation.

Second, by decomposing a QHARS into subarrays accessible through test terminals, it is possible to run the application `QHARSmachine` several times to evaluate the four-terminal resistances simulated distributions of the different subarrays⁴. By implementing auxiliary test QHE bridges (e.g. [27, 28]) into the QHARS, even after the fabrication the consistency of the QHARS subarrays with respect to the simulation can be verified. The reliability can be also checked by repeating this kind of testing along the QHARS’s life .

Lastly, a basic sensitivity analysis can be performed by simulating different arrangements of specific lead or contact resistances.

2.5 SPICE macro-model of a QHE element

Analogue electronic circuit simulation tools, like SPICE [202] and its derivatives, are commonly employed to perform numerical analysis of electrical circuits. SPICE is typically adopted to simulate linear and non-linear networks in time and frequency domains, and to perform noise analysis.

In SPICE, a *netlist* is the list of statements, written according to a certain specific syntax [202, 203], that represents a circuit and how its elements are interconnected. A SPICE macro-model (or *subcircuit netlist*) is a netlist with a designated name that can be treated as any other SPICE element to compose larger circuits in a hierarchical way.

Electrical networks containing QHE elements can be modelled by means of circuit models already existing in literature [92, 181–185, 204–207]. These circuit models are only composed of resistors (to represent the memorylessness and passivity) and controlled sources (to represent the nonreciprocity). Since the external behaviour of the circuit models is exactly described by (2.1) and (2.2) [9], they need not to be related to the actual device physics. All the mentioned circuit models can be directly translated into SPICE macro-models as circuits composed exclusively of resistors and controlled sources, being equivalent from the point of view of circuit theory. However, many of those models are not numerically solvable and a SPICE simulation would fail to run.

⁴The application can be extended to simulate the joint distributions of the different subarrays.

Actually, there exist at least two properties required by SPICE models to be solvable, (1) and (2) below, but one more, (3), would be useful [185]:

1. *No loops of voltage sources.* Only circuits not containing loops composed of only ideal voltage sources (independent or controlled) can be solved by SPICE. Otherwise, either Kirchhoff’s voltage law would be violated or the current crossing the loop would be indeterminate, such that the circuit could not be univocally solved.
2. *No cut sets of current sources.* This property is the dual of (1). Only circuits not containing a node where only current sources join can be solved by SPICE. Otherwise, either Kirchhoff’s current law would be violated or the node potential would be indeterminate (floating node).
3. *Non-dissipative/generative sources.* QHE elements are passive elements that dissipate power. A further desirable property of the circuit model is that the power is completely dissipated in the resistors, whereas the overall power absorbed or delivered by the controlled sources is zero. If this property is fulfilled by the circuit model, the thermal noise generated by the QHE elements can be correctly predicted by SPICE, even if SPICE have still a few limitations in noise analysis (e.g. it is not able to analyze correlations directly and a workaround is needed [208]). This property is not strictly required, but it might help to obtain a circuit model as complete as possible.

Table 2.1 summarizes which properties hold for the circuit models existing in the literature. For the models not fulfilling property (3), the power delivered by the controlled sources is reported in the cw case.

Table 2.1: Properties satisfied by the existing circuit models [92, 181–185, 204–207]. The holding of a certain property is indicated by a bullet. For property (3), the power delivered by the controlled sources is reported (in the cw case) when this is not identically zero.

Model	Property (1)	Property (2)	Property (3)
1. Ricketts-Kemeny [182]		•	•
2. Hartland <i>et al.</i> [204, 205]	•	•	$p = 2r(j_3 + j_4)(j_2 + j_3 + 2j_4)$
3. Jeffery <i>et al.</i> [92, 181]		•	•
4. Sosso-Capra [184, 206]	•	•	$p = e_1j_2 + e_2j_3 + e_3j_4 + e_4j_1$
5. Schurr <i>et al.</i> [183, 207]		•	$p = 2r(j_1j_2 + j_3j_4)$
6. Ortolano-Callegaro [185]	•		•

Models 1 and 3 of table 2.1 violate property (1). Even though two remedies may be adopted to fulfill it, none of them are completely satisfactory. In fact, by adding

a small series resistance to the loop of voltage sources [209], the effect on the simulation accuracy cannot be easily predicted in the case of many interconnected QHE elements. By removing one of the controlled sources in the loop (this does not alter the model’s behaviour), the symmetry of the model would be destroyed, making it more difficult to develop possible refinements to take account of nonidealities.

Model 6 violates property (2). However, since the potential of the floating node of this model can be fixed arbitrarily without altering the model’s behaviour, property (2) can be satisfied without the need for additional elements and without destroying the circuit symmetry. Therefore, model 6 can be implemented as a SPICE macro-model.

In addition, models 2,4 and 5 violate property (3), and cannot be easily modified to satisfy it and are hence not considered further.

The SPICE macro-models for ideal cw and ccw 8-terminal QHE elements proposed in [185] (corresponding to model 6 in table 2.1) are reported in the listings 2.1 and 2.2, respectively ⁵. Here, the node joining the controlled current sources is connected to ground. The default value of R_H is $1\ \Omega$, but other values can be assigned when the macro-model is called or, alternatively, one can normalize all resistances in the circuit to R_H .

These SPICE macro-model are very helpful to simulate, both in DC and AC, the electric behaviour of complex network composed of QHE elements, such as graphene pn-junctions [2]. However, with respect to the method described in section 2.2 and implemented with arbitrary precision arithmetic, SPICE simulations may in some cases generate inaccurate results due to round-off errors.

Listing 2.1: SPICE macro-model for an ideal cw 8-terminal element.

```
.subckt qhe8cw 1 2 3 4 5 6 7 8 params: RH=1
R1 1 2 {2*RH}
R2 2 3 {2*RH}
R3 3 4 {2*RH}
R4 4 5 {2*RH}
R5 5 6 {2*RH}
R6 6 7 {2*RH}
R7 7 8 {2*RH}
R8 8 1 {2*RH}
G1 1 0 2 8 {1/(2*RH)}
G2 2 0 3 1 {1/(2*RH)}
G3 3 0 4 2 {1/(2*RH)}
G4 4 0 5 3 {1/(2*RH)}
G5 5 0 6 4 {1/(2*RH)}
G6 6 0 7 5 {1/(2*RH)}
G7 7 0 8 6 {1/(2*RH)}
```

⁵These macro-models should work out of the box, or with just slight modifications, with any modern SPICE simulator that accepts subcircuits with parameters.

```
G8 8 0 1 7 {1/(2*RH)}  
.ends
```

Listing 2.2: SPICE macro-model for an ideal ccw 8-terminal element.

```
.subckt qhe8ccw 1 2 3 4 5 6 7 8 params: RH=1  
R1 1 2 {2*RH}  
R2 2 3 {2*RH}  
R3 3 4 {2*RH}  
R4 4 5 {2*RH}  
R5 5 6 {2*RH}  
R6 6 7 {2*RH}  
R7 7 8 {2*RH}  
R8 8 1 {2*RH}  
G1 0 1 2 8 {1/(2*RH)}  
G2 0 2 3 1 {1/(2*RH)}  
G3 0 3 4 2 {1/(2*RH)}  
G4 0 4 5 3 {1/(2*RH)}  
G5 0 5 6 4 {1/(2*RH)}  
G6 0 6 7 5 {1/(2*RH)}  
G7 0 7 8 6 {1/(2*RH)}  
G8 0 8 1 7 {1/(2*RH)}  
.ends
```

Chapter 3

Quantum Hall Kelvin Bridge

This chapter presents the design of a DC quantum Hall Kelvin bridge for the direct calibration of standard resistors against a QHR and its first implementation in the Resistance Metrology and in the Graphene Laboratories at NIST, Gaithersburg, MD, US Marzano et al. [4].

The simple bridge design involves a minimal number of instruments and does not include any adjustable element: the bridge reading is the deviation from equilibrium. The bridge implementation is based on a *bridge-on-a-chip*, a QHARS composed of three graphene QHE elements and superconducting wiring. Moreover, the QHE properties provide a Kelvin-like combining network able to reject the stray resistances of contacts and connections, even in the case of wiring with normal conductors. The bridge is able to calibrate a $12\,906\,\Omega$ standard resistor with a standard uncertainty of a few parts in 10^9 , comparable with that of the bridges traditionally employed in such calibrations.

Section 3.1 explains the reasons why the quantum Hall Kelvin bridge is interesting for metrological applications. In section 3.2, the conventional Kelvin bridge is briefly reviewed. Section 3.3 presents the theory of operation of the quantum Hall Kelvin bridge. Section 3.4 describes the device employed for the bridge implementation and its characterization. In sections 3.6 and 3.7, a detailed circuit model of the whole electrical network is developed to evaluate the measurement uncertainty. Section 3.8 reports the measurement results showing that the bridge can calibrate a resistor having nominal value R_H with a relative uncertainty of a few parts in 10^9 , thus comparable with that of the CCC bridge [210] employed during the validation measurements. As finally discussed in section 3.9, the quantum Hall Kelvin bridge concept can be extended to include QHARSs [90, 211] in place of the individual elements, thus allowing the calibration of resistance standards having nominal values different from R_H , like decadal ones.

3.1 Motivations

The QHE is commonly exploited by the NMIs for the realization of the unit of resistance (section 1.2.1). The most common traceability chain is based on a QHE experiment: a resistance bridge compares the quantized resistance $R_H \approx 12\,906.4\,\Omega$ of a single QHE element with the resistance of the artefact standard under calibration. The resistance standards of interest have nominal values in decadal sequence ($100\,\Omega$, $1\,\text{k}\Omega$, ...) or equal to R_H [125, 205].

As discussed in section 1.4, the resistance bridges with the highest accuracy, at the 10^{-9} level, are based on the CCC [112, 113]. This device operates in a low-noise, low-magnetic field liquid helium cryogenic environment, necessarily independent from that where the QHE is realized. The calibration can be performed also with a dedicated room-temperature DCC bridge, though this is limited by the few available resistance ratios (for instance, only the $R_H : 1\,\text{k}\Omega$ ratio might be available for the measurement of R_H), the minimum current intensity in the QHE device and the measurement accuracy, at the 10^{-8} level [210]. Both CCC and DCC bridges are expensive instruments.

The peculiar properties of the QHE let traditional measurement circuits be rearranged in a novel perspective. The QHARSs, introduced in section 1.3.2, are being investigated as resistance standards with decadal resistance values (e.g. [96]) and voltage dividers (e.g. [212]). These networks require multiple connections [86, 90] to reduce the effect of the stray resistances due to contacts and connections. A bridge composed of four QHE elements was designed to verify the reproducibility of the QHR [86], and later implemented with GaAs QHRs with an accuracy of few parts in 10^{11} [27, 28].

3.2 Traditional Kelvin bridge

Figure 3.1 shows the schematic of a traditional Kelvin bridge, suitable to compare two impedances of low value Z_1 and Z_2 approximately defined as four-terminal standards. z identifies the stray impedance between the nodes A and B. The impedances z_1 and z_2 compose the so-called *Kelvin arm* [114, 115].

By means of a $\Delta - Y$ transformation of the impedances z_1 , z_2 and z into z_A , z_B and z_C (on the right in figure 3.1), with

$$z_A = \frac{zz_1}{z + z_1 + z_2}, \quad z_B = \frac{zz_2}{z + z_1 + z_2}, \quad (3.1)$$

the bridge can be analyzed as a Wheatstone bridge, with impedances under comparison $Z_1 + z_A$, $Z_2 + z_B$, Z_3 and Z_4 . The impedance z_C , in series with D, modifies only the sensitivity of the detector but not the balance equation (1.26), which is now

$$\frac{Z_1 + z_A}{Z_2 + z_B} = \frac{Z_3}{Z_4}. \quad (3.2)$$

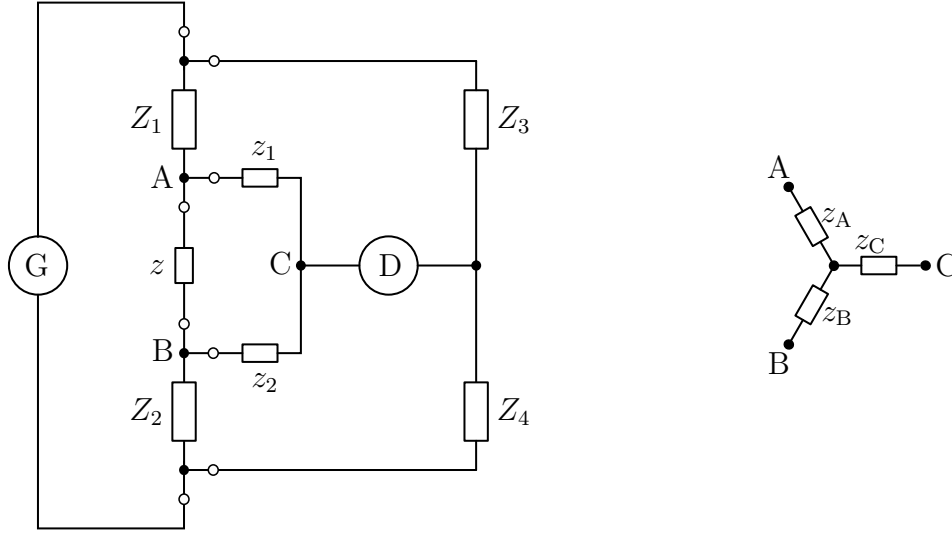


Figure 3.1: The schematic on the left represents the traditional Kelvin bridge. The interconnection impedance between nodes A and B is modelled by z . z_1 and z_2 compose the Kelvin arm. On the right, the schematic represents the impedances z_A , z_B and z_C resulting from the $\Delta - Y$ transformation of the impedances z_1 , z_2 and z .

By substituting (3.1) into (3.2), the Kelvin bridge balance equation becomes

$$\frac{Z_1(z + z_1 + z_2) + zz_1}{Z_2(z + z_1 + z_2) + zz_2} = \frac{Z_3}{Z_4}, \quad (3.3)$$

which is independent of the value of z if the *Kelvin condition*

$$\frac{z_1}{z_2} = \frac{Z_1}{Z_2} = \frac{Z_3}{Z_4} \quad (3.4)$$

is fulfilled.

The above condition can be achieved by selecting the nominal values of z_1 and z_2 , or by modifying the voltage across z (by varying z itself or by adding a small voltage) and adjusting z_1 and z_2 so that the equilibrium condition is insensitive to the variation of the voltage across z .

The Kelvin arm is an example of *combining network*. In fact, because of the impedances z_1 and z_2 , the potential at node C is a linear combination of the potentials at nodes A and B. The combining network is thus adjusted so that the potential at node C is independent of the unknown voltage across z .

When the Kelvin condition is not fulfilled, there is an error that depends at the first order on the stray resistances.

3.3 Quantum Hall Kelvin bridge: theory of operation

The bridge design presented in this chapter is a DC quantum Hall Kelvin bridge able to calibrate four-terminal resistance standards with value close to the quantized Hall resistance $R_H \approx 12\,906.4\,\Omega$ directly against the DC QHE [3]. A compact possible implementation considers the employment of a QHARS to reduce the number of connections required.

The bridge principle schematic is shown in figure 3.2 and its operation exploits the unique properties of the QHE as a circuit element [182]: multiple connections [86], introduced in 1.3.2, reduce the effect of lead resistances, and mimic the behaviour of the combining network of a conventional Kelvin bridge introduced in the previous section.

U_2 and U_3 are the two QHE elements composing the ratio arm; the QHE element U_1 and the four-terminal resistance standard under calibration R_x compose the opposite arm. Let us set $R_x = R_H(1 + x)$, x being the relative deviation of R_x from R_H . The bridge operates in the *deflection mode*, that is, the measurand x is related to the bridge unbalance voltage V_D .

The bridge is driven by the excitation current I which splits between the two bridge arms, such that I_x is the current fraction crossing U_1 and R_x and $V = R_H I_x$ is the Hall voltage measured across U_1 .

U_1 , U_2 and U_3 are connected by triple-series and -parallel connections; U_1 and U_3 are connected to R_x by a double-series connection between the current terminals and a single connection between the voltage terminals.

We assume here that the QHE elements are interconnected within the cryogenic system to form a single device, (blue in figure 3.2). The red colour represents instead the room-temperature four-terminal resistance standard under calibration and its connections to the QHE elements.

In an ideal case, where lead and contact resistances are zero, and leakage resistances are infinite, the bridge can be assimilated to the equivalent circuit of figure 3.3. Applying the Kirchhoff's voltage law to the 8-shaped path Γ yields

$$-V_3 + V_D - V + V_2 + V_D + V_x = 0. \quad (3.5)$$

Since $V_x = (R_x/R_1)V$ and, for ideal QHE elements, $R_1 = R_2 = R_3$ and $V_2 = V_3$, the measurement model in the ideal case is

$$x = -2 \frac{V_D}{V}. \quad (3.6)$$

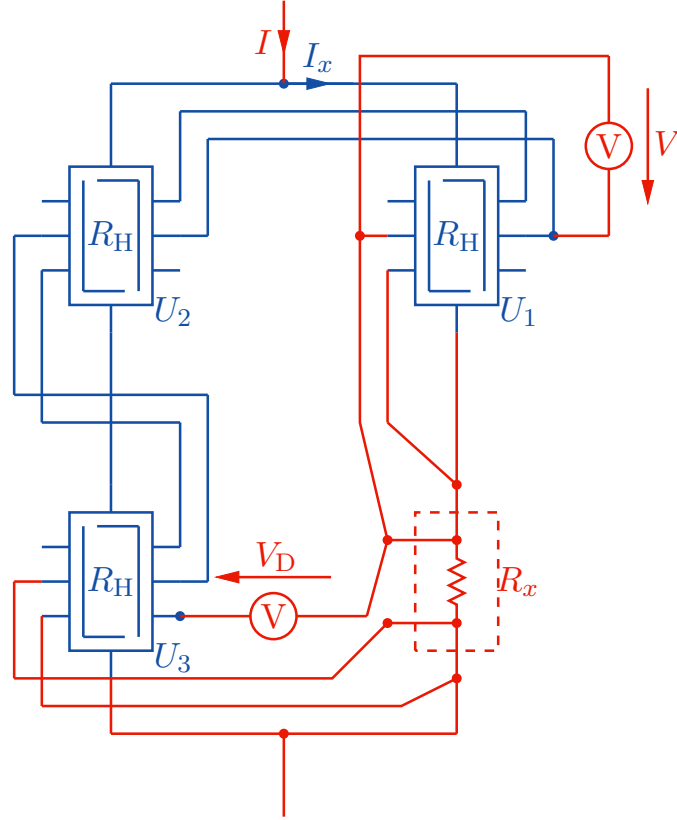


Figure 3.2: Principle schematic of the proposed quantum Kelvin bridge. U_1 , U_2 and U_3 are the QHE elements, interconnected by triple-series and -parallel connections. R_x is the four-terminal resistance standard under calibration, connected to U_1 and U_3 by a double series connection between the current terminals and a single connection between the voltage terminals. I is the bridge excitation current. V_D the bridge unbalance differential voltage. The voltage drop across U_1 and V_D is $V = R_H I_x$, where I_x is the current fraction crossing U_1 and R_x . Blue elements represent the device; red elements are external to the device. Reproduced with permission from Marzano et al. [4] ©IOP Publishing. All rights reserved.

3.4 Bridge-on-a-chip: device description and characterization

In general, the quantum Hall Kelvin bridge can be implemented by means of three single QHE elements separately mounted on a holder and interconnected by wired multiple connections or, alternatively, by means of a QHARS, on which the multiple connections are integrated into the device. The latter can be called a *bridge-on-a-chip*.

The bridge-on-a-chip can be implemented with any type of QHE elements (e.g.

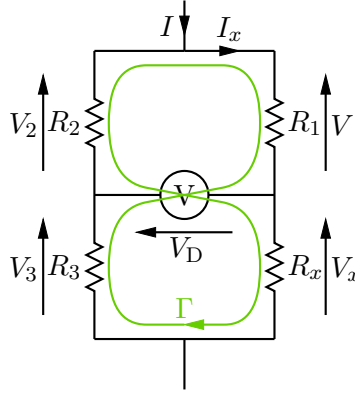


Figure 3.3: The schematic represents the bridge equivalent circuit in the ideal case. The resistances of the QHE elements U_1 , U_2 and U_3 are represented by R_1 , R_2 and R_3 , respectively. V , V_2 and V_3 correspond to the Hall voltages across U_1 , U_2 and U_3 , V_x is the voltage across the resistance standard under calibration R_x . The green-highlighted 8-shaped path Γ is a reference path for the derivation of the bridge model. Reproduced with permission from Marzano et al. [4] ©IOP Publishing. All rights reserved.

GaAs or graphene) and with conventional double- or triple-connections, according to the schematic of figure 3.2.

The quantum Hall Kelvin bridge herewith presented was implemented using a quantum Hall array resistance standard (QHARS) composed of three multiple-series and parallel interconnected graphene Hall bars. To reduce the effect of contact resistances, split contacts are applied as described in [85]. Furthermore, superconducting interconnections are adopted, which do not have ohmic resistance and do not suffer from magnetoresistance, so that the voltage terminals are directly connected to the current path, making the QHARS as precise and stable as a single QHE resistance standard [98]. Because of the superconducting interconnections, this kind of QHARS differs from a conventional one for being *crossover free*. This means that different insulated layers are no more required to avoid the crossing leads crossover. Both the split contacts and the interconnections are made of NbTiN.

The mounted sample and the design details of the QHARS are presented in figure 3.4. Figures 3.4(b) and (c) report the sample characterization performed by confocal laser scanning microscopy [213], showing the NbTiN interconnections and split contacts as well as the structured monolayer graphene Hall bar.

The QHARS was fabricated with a graphene sample growth with a process combining face-to-graphite (FTG) and polymer-assisted sublimation growth (PASG). The details of the growth process and of the device fabrication are not topics of this dissertation and are thoroughly described in [71, 75, 85, 214]. For charge carrier density control, the graphene was functionalized with $\text{Cr}(\text{CO})_3$ in a purpose-built

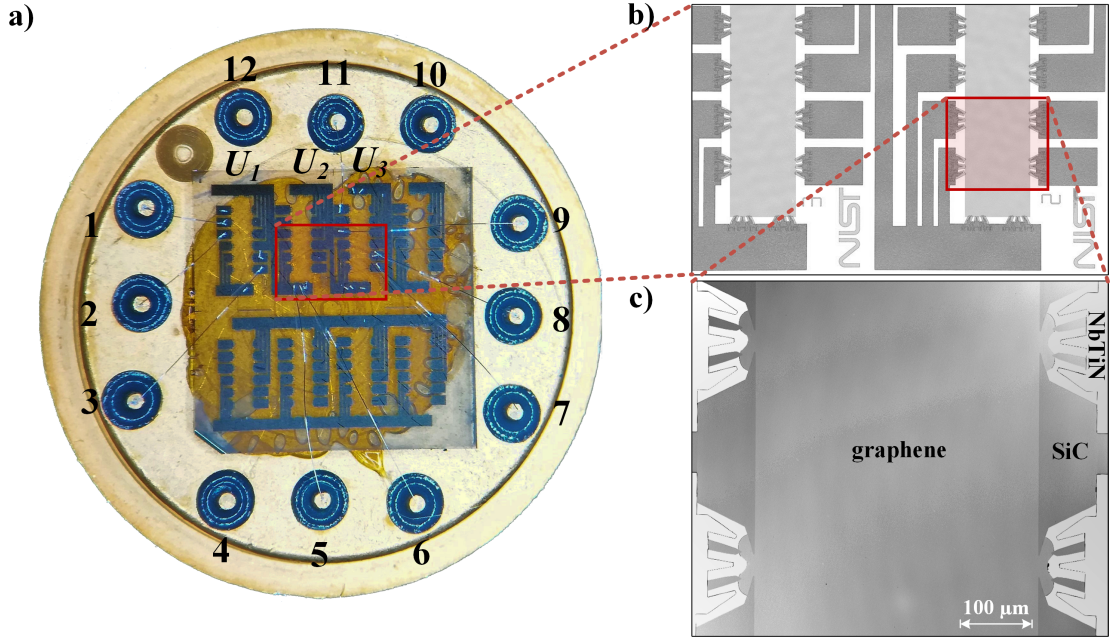


Figure 3.4: (a) The sample was mounted and contacted using a TO-8 header such that only three in series connected devices were active for the measurements. (b) The modified optical microscope image shows design details of the crossover-free multiple connection in the highlighted region of (a). (c) The confocal laser scanning microscope image indicated in (b) shows the split contact geometry as a part of the multiple connection. Reproduced with permission from Marzano et al. [4] ©IOP Publishing. All rights reserved.

deposition chamber after the device fabrication [74].

The QHARS was preliminary characterized at about 1.6 K with a lock-in amplifier system. The current is injected through a series resistor and modulated at 8 Hz, and the Hall and longitudinal voltages are measured by synchronous demodulation with a lock-in amplifier.

Figure 3.5 shows individual measurements of the magnetic field dependence of the Hall resistance R_H and of the longitudinal resistance R_{xx} of U_1 and U_3 in a four-terminal resistance configuration. The injected current is about $30 \mu\text{A}$ for each QHE element. In the legend, $V(i, j)$ is the voltage across the terminals i and j of figure 3.4, and $I(l, m)$ is the current entering into terminal l and exiting from terminal m . For both U_1 and U_3 , R_H and R_{xx} are asymmetric with respect to the magnetic field direction, with a plateau starting around $B = \pm 3 \text{ T}$. Despite both the elements exhibiting the typical behaviour of R_H and R_{xx} when the magnetic field direction is positive, the behaviour of R_{xx} and R_H is atypical when the magnetic field is reversed. This happens because of the different current paths caused by the position of the measurement terminals and the multiple-connections between the

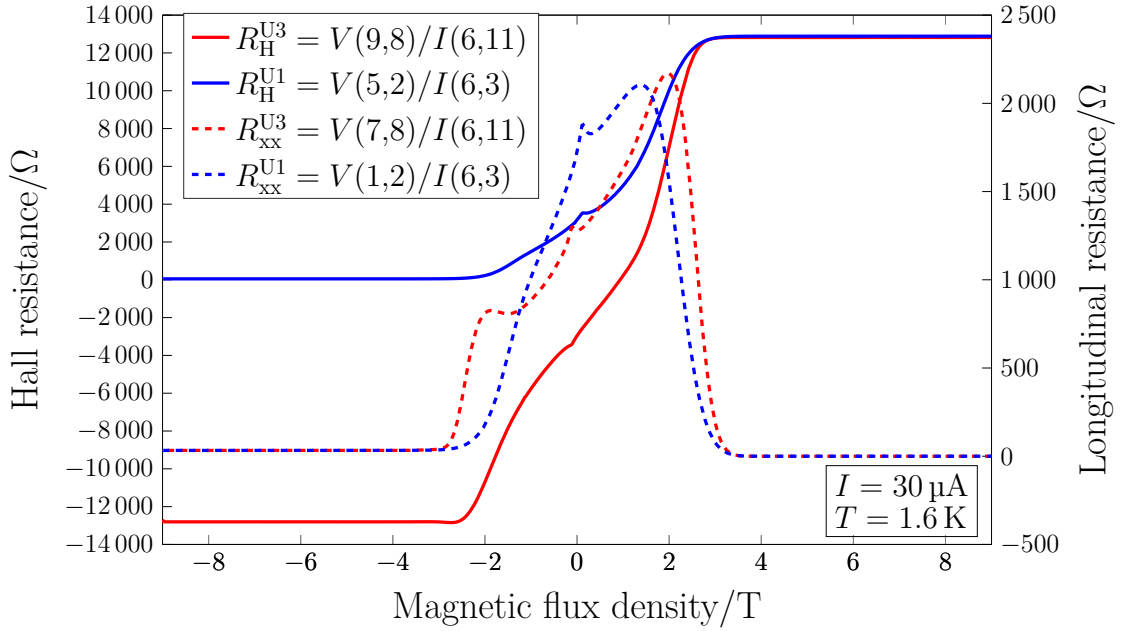


Figure 3.5: Preliminary characterization of the QHARS at $30\ \mu\text{A}$ and $1.6\ \text{K}$. The magnetic field dependence of the Hall resistance R_{H} (solid lines, left axis) and longitudinal resistance R_{xx} (dashed lines, right axis) of U_1 (blue) and U_3 (red) are presented. In the legend, $V(i, j)$ is the voltage drop between the terminals i and j of figure 3.4, $I(l, m)$ is the current entering into terminal l and exiting from terminal m . Reproduced with permission from Marzano et al. [4] ©IOP Publishing. All rights reserved.

devices [85].

The relative deviation of the Hall resistance R_{H} from the nominal value of U_1 , U_2 and U_3 are reported in figure 3.6 for different values of the current I_x injected in each QHE element, at $1.6\ \text{K}$ and $9\ \text{T}$. The measurements are performed by comparing the Hall resistances with a room-temperature $100\ \Omega$ resistance standard (Electro Scientific Industries ESI SR102) in turn calibrated against a GaAs QHR with a binary cryogenic current comparator (BCCC) bridge [113]. The reported bars represent the expanded uncertainties at a coverage factor $k = 2$. Self-heating causes an increase of the deviation with the current. The quantized Hall resistance deviation is less than $20\ \text{n}\Omega\ \Omega^{-1}$ for each device and currents up to $75\ \mu\text{A}$, that is, within the range usually employed in the calibrations. Measurements performed with two different terminal configurations are reported for U_1 and U_2 .

More accurate measurements of the longitudinal resistance R_{xx} of U_1 and U_3 were performed at $70\ \mu\text{A}$, $1.6\ \text{K}$ and $9\ \text{T}$ by means of an analogue nanovoltmeter and a current reversal measurement technique to eliminate offsets. The measured

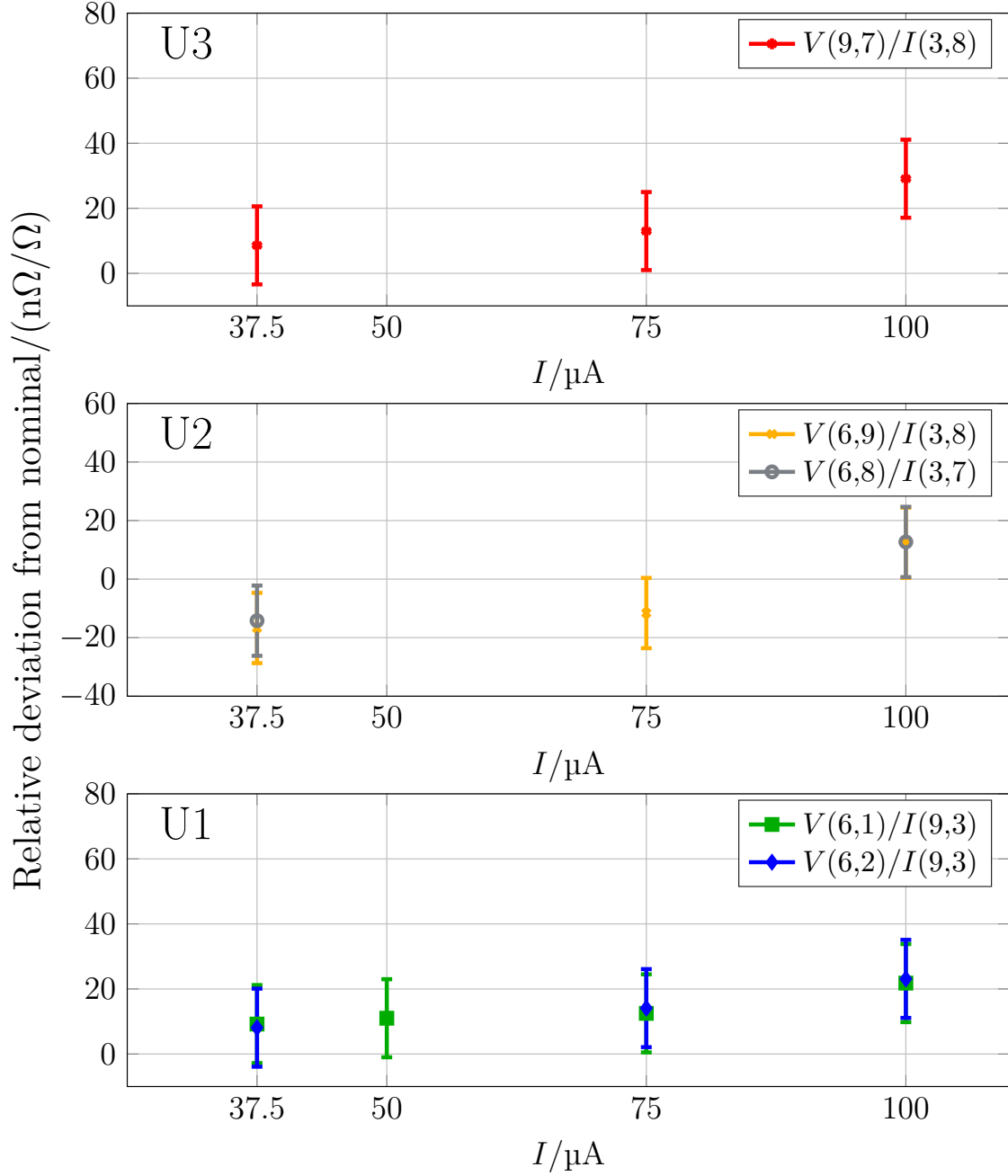


Figure 3.6: Relative deviation of the Hall resistance R_H from the nominal value of U_1 , U_2 and U_3 for different current values I_x at 1.6 K and 9 T. Measurements performed with two different terminal configurations are reported for the elements U_1 and U_2 . The measurements exhibit the expanded uncertainties ($k = 2$). Reproduced with permission from Marzano et al. [4] ©IOP Publishing. All rights reserved.

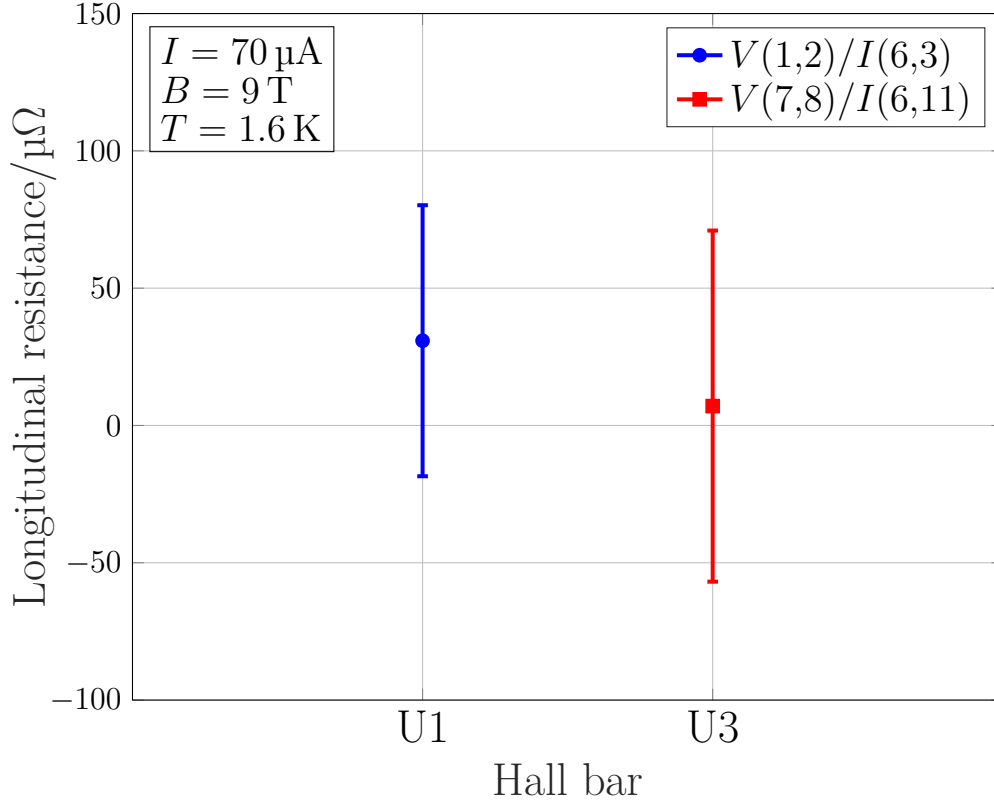


Figure 3.7: Measurements of the longitudinal resistances R_{xx} of U_1 and U_3 at $70\ \mu\text{A}$, $9\ \text{T}$ and $1.6\ \text{K}$. Reproduced with permission from Marzano et al. [4] ©IOP Publishing. All rights reserved.

resistances, presented in figure 3.7, are zero within the measurement uncertainty, $R_{xx}^{U1} = 31(49)\ \mu\Omega$ and $R_{xx}^{U3} = 7(64)\ \mu\Omega$. The uncertainty bars represent the standard uncertainty.

3.5 Experimental setup

The quantum Hall Kelvin bridge operates in the cryogenic system shown in figure 3.8 on the next page. The system usually works at about $1.6\ \text{K}$ and with a magnetic flux density up to $9\ \text{T}$.

Figure 3.9 shows the four-terminal resistance standard under calibration, the $12.9\ \text{k}\Omega$ NIST resistance standard (NIST ESI SP036), kept in a temperature-controlled oil bath at $25\ ^\circ\text{C}$ located in a different laboratory and connected to the bridge through $\approx 10\ \text{m}$ long cables.

The implementation of the bridge is shown in figure 3.10 on the following page:



Figure 3.8: Cryogenic system employed for the implementation of the bridge. The system usually works at about 1.5 K and with a magnetic flux density up to 9 T.

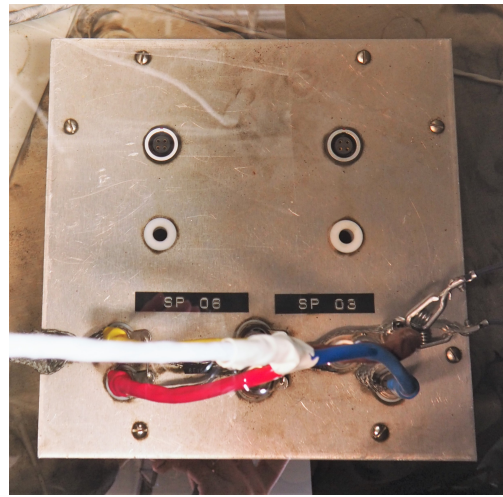


Figure 3.9: The 12.9 k Ω NIST four-terminal resistance standard (NIST ESI SP036) under calibration. The resistance standard is kept in a temperature-controlled oil bath at 25 °C located in a different laboratory and connected to the bridge through long shielded cables.

the bridge-on-a-chip is represented by the blue elements and connections; the four-terminal resistance standard under calibration and its connections with the device are represented by the red element and connections; the voltmeter used to measure the bridge voltages is represented by the green elements.

The numbers labelling the connections corresponds to the wire-bonded TO-8

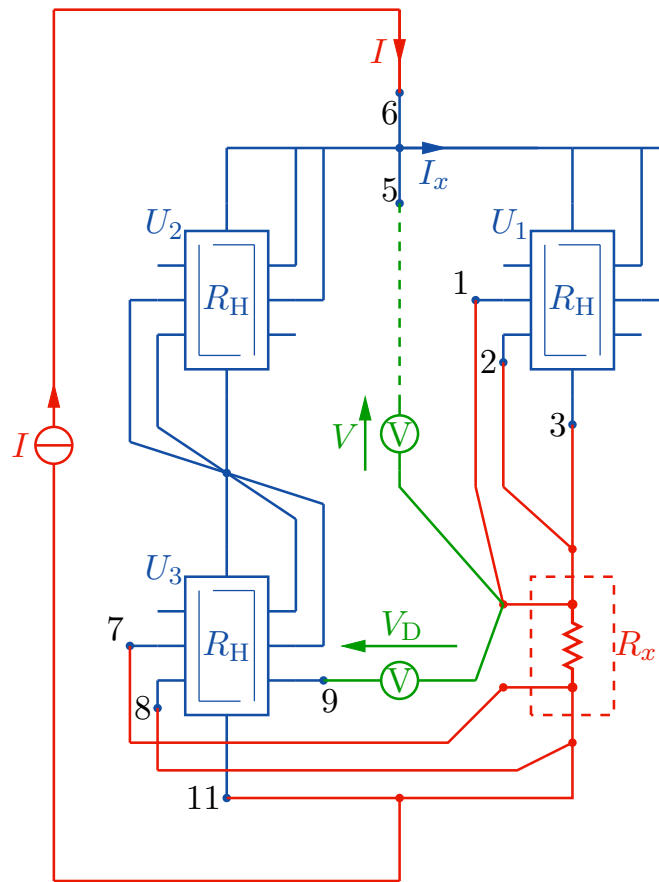


Figure 3.10: Schematic of the quantum Hall Kelvin bridge implemented with a QHARS composed of crossover-free multiple connections. Reproduced with permission from Marzano et al. [4] ©IOP Publishing. All rights reserved.

holder pins, as shown in figure 3.4.

An Adret 103A direct current and voltage standard is employed to generate the bridge excitation current I . An Agilent 34420A nanovoltmeter, manually switched between terminals 5 and 9, alternatively measures the voltages V and V_D .

The computer application employed for the data acquisition is the modified version of a software developed at NIST under the National Instruments Labview environment.

3.6 Error sources

The bridge measurements are affected by several error sources, which are here listed and analyzed individually by means of suitable mathematical models. The evaluation of the uncertainty presented in section 3.8 is obtained by applying the

complete measurement model presented in section 3.7 and composed of all the individual error terms.

The first errors discussed below are those which depend on the practical implementation of the bridge, even with ideal QHE elements: bias and drift, voltmeter error, lead, contact and leakage resistances. Then, the possible imperfect quantization of the QHE devices is discussed, and this mainly depends on the device fabrication and the operating conditions.

The computer method presented in [1, 9] is employed to obtain the analytical expression of the errors caused by lead, contact and leakage resistances.

3.6.1 Bias and drift

Thermoelectric voltages in the bridge circuit and voltmeter residual offset and bias current may bias to the bridge readings, and this bias can also drift with time. By periodically reversing the bridge excitation with an appropriate pattern, it is possible to eliminate the effect of both bias and drift [215, 216].

For this purpose, in this work, the excitation current I is periodically reversed with the sign pattern $- + + -$. This removes bias and first-order drift [215, 216]. This sign pattern corresponds to the raw readings $V_D^{\text{read},1}$ ($-$), $V_D^{\text{read},2}$ ($+$), $V_D^{\text{read},3}$ ($+$) and $V_D^{\text{read},4}$ ($-$). The combination of the raw readings yields to the following reading of the unbalance voltage:

$$V_D^{\text{read}} = \frac{1}{4}(-V_D^{\text{read},1} + V_D^{\text{read},2} + V_D^{\text{read},3} - V_D^{\text{read},4}). \quad (3.7)$$

Likewise, for the Hall voltage,

$$V^{\text{read}} = \frac{1}{4}(-V^{\text{read},1} + V^{\text{read},2} + V^{\text{read},3} - V^{\text{read},4}). \quad (3.8)$$

If the mean excitation current is sufficiently stable between the measurement phase of V_D and that of V , this method ensures also the rejection of any asymmetry between positive and negative excitation, considered as a bias with respect to the mean excitation.

3.6.2 Voltmeter error

The measurement of V_D is affected by a voltmeter systematic error that can be split into a gain error g_D , an offset error $V_{D,\text{OS}}$ and a nonlinearity error ΔV_D^\pm , as represented in figure 3.11 on page 69. The bridge unbalance voltage for positive and negative excitation can be represented by V_D and $-V_D$, respectively, and the

readings in the pattern $- + + -$ are thus

$$-V_D = (1 + g_D)V_D^{\text{read},1} + V_{D,\text{OS}} - \Delta V_D^-, \quad (3.9)$$

$$V_D = (1 + g_D)V_D^{\text{read},2} + V_{D,\text{OS}} - \Delta V_D^+, \quad (3.10)$$

$$V_D = (1 + g_D)V_D^{\text{read},3} + V_{D,\text{OS}} - \Delta V_D^+, \quad (3.11)$$

$$-V_D = (1 + g_D)V_D^{\text{read},4} + V_{D,\text{OS}} - \Delta V_D^-. \quad (3.12)$$

The combination of the above raw voltages, as in (3.7), yields

$$V_D = (1 + g_D)V_D^{\text{read}} - \Delta V_D, \quad (3.13)$$

with $\Delta V_D = (\Delta V_D^+ - \Delta V_D^-)/2$. The terms g_D and ΔV_D can be assumed to have zero value with uncertainties evaluated from the voltmeter specifications.

Similarly, for the Hall voltage,

$$V = (1 + g)V^{\text{read}} - \Delta V. \quad (3.14)$$

The measurement of ΔV_D and V are usually performed with the voltmeter set in two different ranges, so that the quantities g_D , g , ΔV_D and ΔV can be assumed to be uncorrelated.

3.6.3 Lead and contact resistances

The major lead and contact resistances of the implemented bridge are represented in the equivalent circuit shown in figure 3.12 on page 70. Assuming lead resistances much less than R_H , this circuit can be analyzed with the method developed in [9]. For this purpose, an analytical version of the QHARSmachine application [1] (introduced in section 2 and reported in appendix A) was developed. The resulted Mathematica notebook is reported in appendix A.2.

The result of the analysis is the relationship

$$x = -2\frac{V_D}{V} - \Delta x^{\text{leads}} \quad (3.15)$$

with

$$\Delta x^{\text{leads}} = \frac{1}{R_H^2} [r_a(r_b - r_1) + (r_c + r_4)r_d] + O\left(\frac{r_{\text{max}}}{R_H}\right)^3, \quad (3.16)$$

where r_{max} is the maximum lead resistance of a connection and the *big O notation* specifies the limit on the growth rate of the higher-order terms.

Thus, the lead resistances r_1 , r_a , r_b , $r_c + r_4$, and r_d contribute at second order to Δx^{leads} . Otherwise, Δx^{leads} depends only at third order on the resistances r_2 , r_3 , r_5 and r_6 , as expected from a triple-series connection.

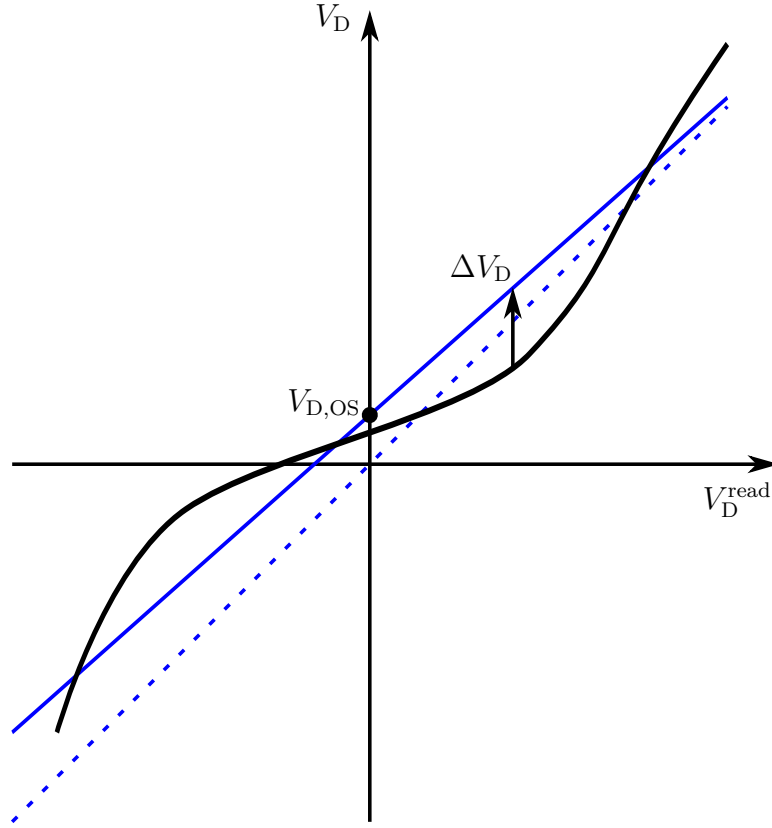


Figure 3.11: Voltmeter transfer characteristic representing the relation between the unbalance voltage V_D and the voltmeter reading V_D^{read} : the solid black curve is the voltmeter transfer characteristic; the solid blue line is a linear approximation with slope $1 + g_D$ and offset $\Delta V_{D,OS}$; and the dashed blue line is the ideal transfer characteristic with unit slope. The vertical deviation between the linear approximation and the transfer characteristic is the nonlinearity error ΔV_D .

As introduced in section 3.2, in addition to the main voltage ratio arm— R_2 and R_3 of figure 3.3, a Kelvin bridge is characterised by a *Kelvin arm*, that is, a network of two additional resistors combining [114, 115] the potentials at the low-voltage terminals (not shown in figure 3.3) of R_1 and R_x . In the case of the quantum Hall Kelvin bridge, in figure 3.12, the role of terminal 1 of U_1 is analogous to the low-voltage terminal of R_1 , so that r_b and r_1 can be considered as a Kelvin arm for the voltage on r_a . The term $r_a(r_b - r_1)$ in (3.16) models the contribution to Δx^{leads} caused by the unbalance of this Kelvin arm. In fact, differing from a conventional Kelvin bridge, the unbalance of the Kelvin arm has a second order effect on Δx^{leads} , because of the properties of the QHE, which scale down the current in the Kelvin arm.

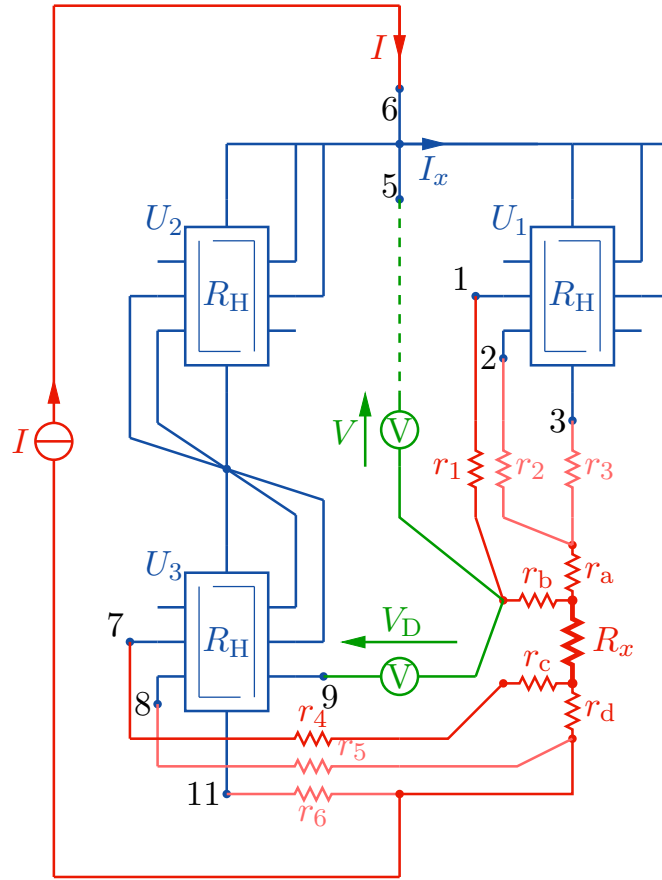


Figure 3.12: Equivalent circuit including the most significant lead resistances of the implemented bridge (contact resistances are incorporated into lead resistances). Letter subscripts identify the lead resistances associated to the four-terminal resistor under calibration; number subscripts identify the resistances associated to the connections to the cryogenic system. Reproduced with permission from Marzano et al. [4] ©IOP Publishing. All rights reserved.

3.6.4 Leakage resistances

The equivalent circuit of the implemented bridge with the leakage resistances of interest is shown in figure 3.13 on the next page: the resistance R_{CL} from the voltmeter low terminal to ground, which includes also the leakage resistances of the interconnection and the common-mode resistance of the voltmeter; the resistance R_{CH} from the high terminal to ground; and the differential resistance R_D of the voltmeter. The bridge unbalance voltage can be written as $V_D = V_{DH} - V_{DL}$, where V_{DL} and V_{DH} are, respectively, the voltage of the low and high voltmeter terminals with respect to ground.

Generally, by directly grounding V_{DL} by means of a Wagner ground [115], $V_{DL} \approx$

By considering now V_D and V as, respectively, the average unbalance and Hall voltages, the circuit of figure 3.13 can be analyzed to obtain the relationship

$$x = -2\frac{V_D}{V} - \Delta x^{\text{leak}} \quad (3.17)$$

with

$$\Delta x^{\text{leak}} = 2\frac{V_D}{V} \left(\frac{R_H}{2R_{\text{CL}}} + \frac{3R_H}{2R_D} \right) - \frac{R_H}{R_{\text{CL}}} \left(\frac{R_H}{R_{\text{CH}}} - \frac{R_H}{2R_{\text{CL}}} \right). \quad (3.18)$$

Leakage resistances thus cause both multiplicative and additive errors.

3.6.5 Imperfect quantization

The effect of the possible imperfect quantization of the QHE elements can be analyzed by defining the QHE elements of figure 3.3 as

$$R_1 = R_H(1 + x_1), \quad (3.19)$$

$$R_2 = R_H(1 + x_2), \quad (3.20)$$

$$R_3 = R_H(1 + x_3), \quad (3.21)$$

where x_1 , x_2 and x_3 are the relative deviations of the resistances from R_H , representing the quantization errors. The voltages V , V_2 , V_3 and V_x of (3.5) are thus

$$V = R_H(1 + x_1)I_x, \quad (3.22)$$

$$V_2 = R_H(1 + x_2)(I - I_x), \quad (3.23)$$

$$V_3 = R_H(1 + x_3)(I - I_x), \quad (3.24)$$

$$V_x = R_H(1 + x)I_x. \quad (3.25)$$

By substituting the above expressions into (3.5) and simplifying, we obtain

$$R_H(I - I_x)(x_2 - x_3) + R_H I_x(x - x_1) + 2V_D = 0. \quad (3.26)$$

Since all terms in (3.26) are at first order in x , x_1 , x_2 and x_3 , the currents I_x and $(I - I_x)$ can be approximated at the zeroth order, that is,

$$R_H(I - I_x) \approx R_H I_x \approx V. \quad (3.27)$$

Therefore, with this assumption, we obtain the relationship

$$x = -2\frac{V_D}{V} - \Delta x^{\text{quant}} \quad (3.28)$$

with

$$\Delta x^{\text{quant}} = -x_1 + x_2 - x_3. \quad (3.29)$$

3.7 Measurement procedure and model

The discussions of the previous section and, in particular, the approach employed to minimize the leakage resistances effect, yield the here listed measurement procedure for a single measurement (all readings are obtained by periodically reversing the excitation current I according to the pattern $- + + -$):

1. Ground at the low terminal of the current source.
2. Acquisition of repeated readings of V_D and calculation of their average $V_D^{\text{read,low}}$.
3. Acquisition of repeated readings of V and calculation of their average $V^{\text{read,low}}$.
4. Ground at the high terminal of the current source.
5. Acquisition of repeated readings of V_D and calculation of their average $V_D^{\text{read,high}}$.
6. Acquisition of repeated readings of V and calculation of their average $V^{\text{read,high}}$.
7. Calculation of the averages $V_D^{\text{read}} = (V_D^{\text{read,low}} + V_D^{\text{read,high}})/2$, $V^{\text{read}} = (V^{\text{read,low}} + V^{\text{read,high}})/2$ and of the bridge reading $x^{\text{read}} = -2V_D^{\text{read}}/V^{\text{read}}$.

The above steps are then repeated for multiple measurements.

The combination of the results reported in section 3.6 yields the complete measurement model

$$x = -2\frac{V_D}{V} - \Delta x^{\text{leads}} - \Delta x^{\text{leak}} - \Delta x^{\text{quant}}, \quad (3.30)$$

$$= -2\frac{(1 + g_D)V_D^{\text{read}} - \Delta V_D}{(1 + g)V^{\text{read}} - \Delta V} - \Delta x^{\text{leads}} - \Delta x^{\text{leak}} - \Delta x^{\text{quant}}, \quad (3.31)$$

assuming that the nonlinearity errors ΔV_D and ΔV are the same for the grounded-low and grounded-high readings. This model can be simplified by considering that g_D , g , $\Delta V_D/V^{\text{read}}$ and $\Delta V/V^{\text{read}}$ are all small quantities with respect to one. The resulting measuring model is thus

$$x = \left(1 + g_D - g + \frac{\Delta V}{V^{\text{read}}}\right) x^{\text{read}} - 2\frac{\Delta V_D}{V^{\text{read}}} - \Delta x^{\text{leads}} - \Delta x^{\text{leak}} - \Delta x^{\text{quant}}. \quad (3.32)$$

3.8 Results

The quantum Hall Kelvin bridge was validated by means of the procedure schematically represented in figure 3.14. First, the NIST SP036 resistance standard is calibrated directly against the graphene QHR with the quantum Hall Kelvin bridge, obtaining x from (3.32). Then, the same NIST SP036 resistance standard

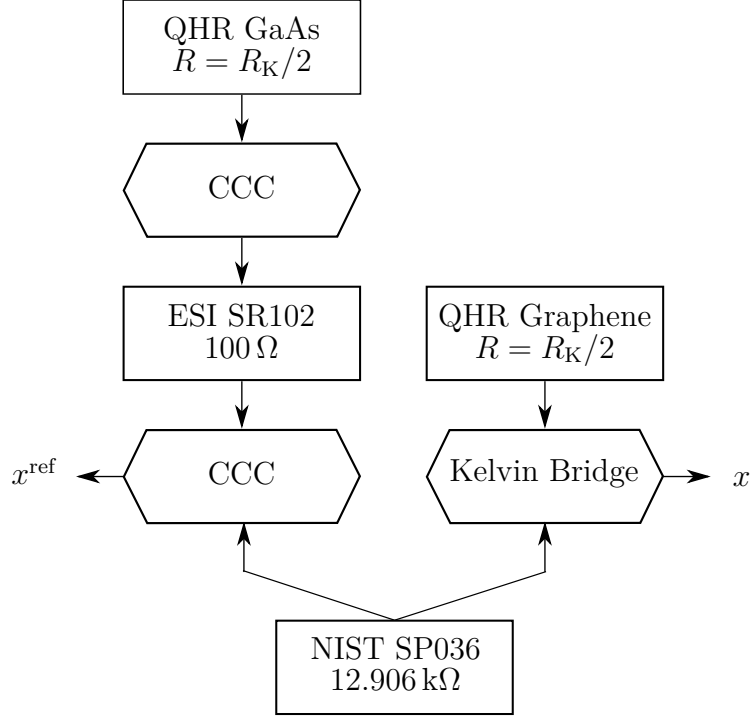


Figure 3.14: Diagram representing the procedure adopted to compare the calibration of the NIST SP036 resistance standard performed with the quantum Hall Kelvin bridge and that performed with the CCC.

is calibrated with a commercially available CCC [113] against a 100 Ω resistance standard (ESI SR102), in turn calibrated with the CCC against a GaAs QHR. The result of this calibration is x^{ref} , that is, the reference relative deviation of R_x from R_H . At last, the result of the comparison is δ , the difference between the calibration performed with the quantum Hall Kelvin bridge and that with the CCC, that is,

$$\delta = x - x^{\text{ref}} \quad (3.33)$$

$$= \left(1 + g_D - g + \frac{\Delta V}{V^{\text{read}}} \right) x^{\text{read}} - 2 \frac{\Delta V_D}{V^{\text{read}}} - \Delta x^{\text{leads}} - \Delta x^{\text{leak}} - \Delta x^{\text{quant}} - x^{\text{ref}} \quad (3.34)$$

$$= \left(1 + g_D - g + \frac{\Delta V}{V^{\text{read}}} \right) x^{\text{read}} - 2 \frac{\Delta V_D}{V^{\text{read}}} - \Delta x^{\text{leads}} - \Delta x^{\text{leak}} + x_1 - x_2 + x_3 - x^{\text{ref}}. \quad (3.35)$$

Table 3.1 on page 78 reports the uncertainty budget for δ of an example comparison performed with $I \approx 150 \mu\text{A}$, so that the current in the QHE elements is $I_x \approx I/2 \approx 75 \mu\text{A}$.

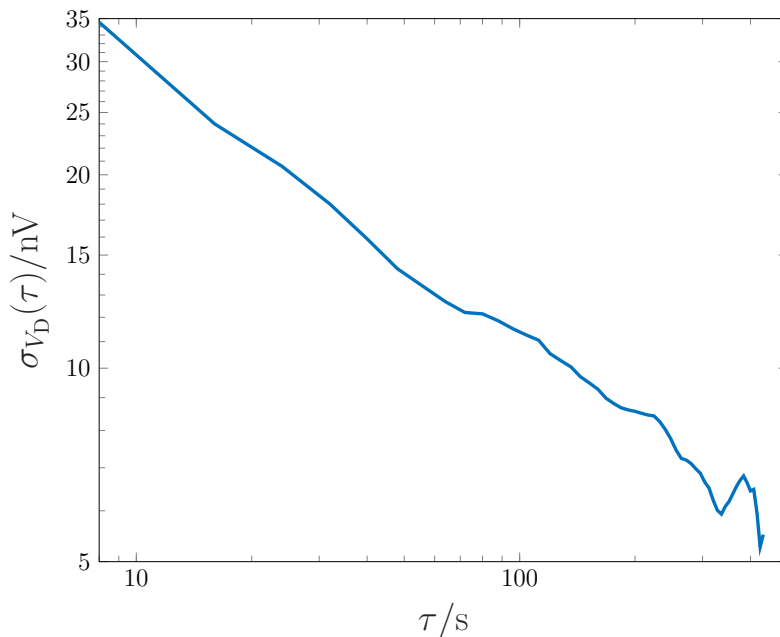


Figure 3.15: Allan deviation $\sigma_{V_D}(\tau)$ of the bridge unbalance voltage with respect to the integration time τ for an example measurement. Reproduced with permission from Marzano et al. [4] ©IOP Publishing. All rights reserved.

The uncertainty component 1 is the type A uncertainty of the bridge reading x^{read} . The reported example measurement represents 4 repeated cycles, as described in section 3.7. Since there is a dead time between the readings, the overall measurement time was about 3 h. An example Allan deviation $\sigma_{V_D}(\tau)$ of the bridge unbalance voltage V_D is reported in figure 3.15, as a function of the effective integration time τ . The slope of the Allan deviation in the log-log plot is about $-1/2$, which means that the dominant noise process is white [217]. The type A uncertainty reported in table 3.1 on page 78 was evaluated accordingly.

The uncertainty components from 2 to 5 are the type B uncertainties of the nanovoltmeter for V_D and V measurements, considering both gain and nonlinearity as described in section 3.6. The ranges of 1 mV and 1 V are adopted to measure V_D and V , respectively. By considering uniform probability distributions for the errors, the uncertainty components were obtained from the instrument specifications. The uncertainty components associated with V are virtually negligible.

Uncertainty component 6 is the correction for the lead resistances, obtained from (3.16) with the measurements of the lead resistances $r_1 \approx 1.43 \Omega$, $r_4 \approx 2.30 \Omega$, $r_a \approx 0.888 \Omega$, $r_b \approx 0.888 \Omega$, $r_c \approx 0.892 \Omega$ and $r_d \approx 0.894 \Omega$, considering a relative uncertainty of 1%. The values of r_1 and r_4 are typical of the cryogenic systems usually employed in the QHE experiments and cannot be easily reduced. The main component of the resistances, in fact, is due to the required small cross section of the

wires composing the cryogenic probe cabling that reduces the heat exchange with the environment. The values of r_a , r_b , r_c and r_d are large in this particular bridge implementation because of the location of the NIST SP036 resistance standard that is, in a different laboratory. The lead resistance values of the here presented implementation yield an error $\Delta x^{\text{leads}} = 1.42 \times 10^{-8}$ that needs to be corrected. Generally, the values of r_a , r_b , r_c and r_d can be reduced by either a more compact bridge implementation or by reducing the values of r_a and r_d connecting nodes 2, 3, 8 and 11 directly to the current terminals of the resistance standard.

Uncertainty component 7 is the correction for the leakage resistances, obtained from (3.18), with the instrument specifications and with the measurements of the leakage resistance of the bridge network. Since R_{CL} , R_{CH} and R_{D} are greater than $10 \text{ G}\Omega$, this uncertainty component is negligible.

Uncertainty component 8 is the correction for the imperfect quantization of the QHARS employed in the bridge, estimated from (3.29) considering the device characterization reported in section 3.4. The resulting error $\Delta x^{\text{quant}} = -3.71 \times 10^{-8}$ is a combination of the quantization errors of all three QHE elements. This error depends on the specific prototype device employed in the bridge implementation and on the current dependence of the QHRs: a recent work has shown that by tuning the fabrication process such devices can reach an accuracy level of 10^{-9} [98].

Uncertainty component 9 is the reference relative deviation of R_x from R_{H} obtained by calibrating the NIST SP036 resistance standard with the CCC.

Uncertainty components 8 and 9 are separated from the other components of the uncertainty budget because they are partially correlated, since both of them are obtained from a CCC calibration against the same ESI SR102 100Ω resistance standard. By referring to (3.29), their correlated part actually cancels in (3.35), so that the remaining uncertainty components are only those associated to the type A uncertainty.

The result of the example comparison is estimated from (3.33) and is the difference $\delta = (2.7 \pm 5.6) \times 10^{-9}$ between the calibration of the NIST SP036 resistance standard performed with the quantum Hall Kelvin bridge and that with the CCC. This is compatible with zero, showing the agreement between the two calibrations of the resistance standard. The uncertainty budget in table 3.1 shows that the type A component of the bridge reading dominates the quantum Hall Kelvin bridge uncertainty.

The final results of δ of four comparisons, performed as described in figure 3.14, are presented in figure 3.16. The uncertainty bars represent the expanded uncertainties with coverage factor $k = 2$. The black triangle in the figure identifies the measurement whose uncertainty budget is presented in table 3.1. One of the reported results refers to a measurement performed with a current $I_x = 37.5 \mu\text{A}$. Since the type A uncertainty is the dominant component of the uncertainty, different measurement times results in different uncertainties among the measurements. Overall, a good agreement between the calibrations performed with the quantum

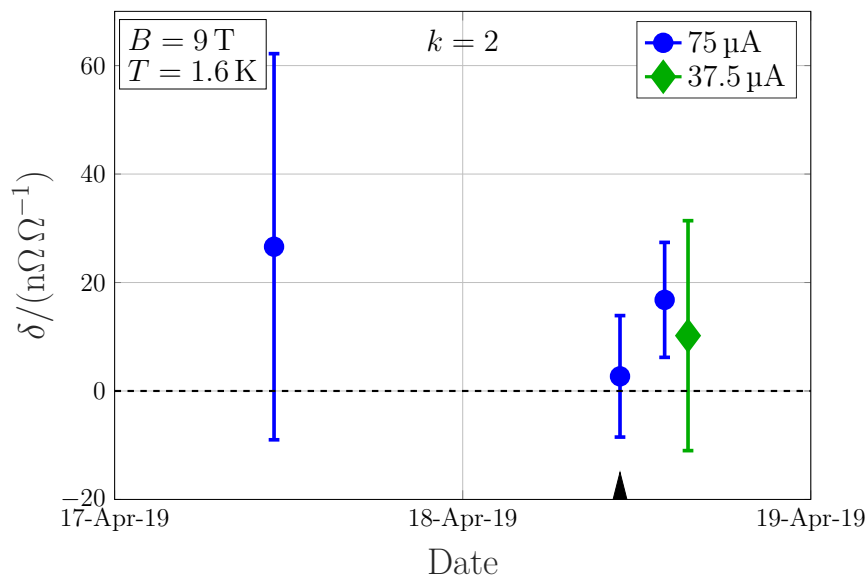


Figure 3.16: Summary plot of the final results of δ of four comparisons as described in figure 3.14. δ is estimated from (3.33) and represents the difference between the calibration performed with the quantum Hall Kelvin bridge and that with the CCC. The uncertainty bars represent the expanded uncertainties with coverage factor $k = 2$. Reproduced with permission from Marzano et al. [4] ©IOP Publishing. All rights reserved.

Hall Kelvin bridge and the CCC is shown by figure 3.16. The single non-compatible measurement and the fact that all the deviations are positive may be likely ascribed to the characterization of the imperfect quantization of the Hall bars, in particular that of U_2 . In fact, as described in section 3.4, U_2 was characterized through an arrangement which differs from that of operation.

By assuming a perfect device quantization, and thus considering in the evaluation of the uncertainty presented in table 3.1 on the following page only the uncertainty components from 1 to 7, the quantum Hall Kelvin bridge uncertainty is at the level of a few parts in 10^9 , comparable to that of a CCC calibration and mainly limited by the type A uncertainty.

Table 3.1: Uncertainty budget for δ of an example comparison at $I \approx 150 \mu\text{A}$. Each input quantity is identified by the index i , its name and the symbol x_i . $c_i = \partial\delta/\partial x_i$ is the sensitivity coefficient of δ with respect to x_i . RSS denotes the root sum of squares.

i	Quantity name	Quantity	x_i	$u(x_i)$	Type	c_i	$u_i(x) = c_i u(x_i)$
1	Bridge reading ($\approx 3\text{h}$)	x^{read}	-3.4567×10^{-6}	5.5×10^{-9}	A	1.0	5.5×10^{-9}
2	Nanovoltmeter gain (V_D)	gD	0	2.9×10^{-5}	B	-3.5×10^{-6}	0.1×10^{-9}
3	Nanovoltmeter gain (V)	g	0	2.0×10^{-5}	B	3.5×10^{-6}	$< 0.1 \times 10^{-9}$
4	Nanovoltmeter nonlinearity (V_D)	ΔV_D	0	0.3 nV	B	-2.1V^{-1}	0.6×10^{-9}
5	Nanovoltmeter nonlinearity (V)	ΔV	0	740 nV	B	$-3.6 \times 10^{-6} \text{V}^{-1}$	$< 0.1 \times 10^{-9}$
6	Lead resistances	Δx^{leads}	1.42×10^{-8}	0.2×10^{-9}	B	-1	0.2×10^{-9}
7	Leakage resistances	Δx^{leak}	$< 10^{-11}$	$< 10^{-11}$	B	-1	$< 0.1 \times 10^{-9}$
8	Imperfect quantization	Δx^{quant}	-3.71×10^{-8}	0.7×10^{-9}	B	-1	0.7×10^{-9}
9	CCC calibration	x^{ref}	-3.4366×10^{-6}	0.4×10^{-9}	B	-1	0.4×10^{-9}
	δ		2.7×10^{-9}		RSS		5.6×10^{-9}

3.9 Further developments

The quantum Hall Kelvin bridge-on-a-chip can be modified to directly calibrate resistance standards with nominal values different from R_H , for instance, with the decadal values widely employed in metrology. This is achievable by replacing a QHE element with a QHARS in one or more arms of the bridge.

The employment of a QHARS for each bridge arm may also reduce the number of the required QHE elements with respect to a resistance comparison with a single QHARS. For instance, $R_x \approx 1 \text{ M}\Omega$ is a resistance value obtainable, with good approximation, with a QHARS composed of 88 QHE elements as $(10150/131)R_H$ [88, 90]. By considering figure 3.3, the bridge balance equation yields

$$R_x \approx \frac{10150}{131}R_H = \frac{R_1 R_3}{R_2}, \quad (3.36)$$

which, with a further decomposition, becomes

$$\frac{10150}{131}R_H = \frac{10R_H \times 5R_H}{\frac{131}{203}R_H} = \frac{R_1 R_3}{R_2}. \quad (3.37)$$

Therefore, a quantum Hall Kelvin bridge with $R_1 = 10R_H$ (10 QHE elements), $R_2 = (131/203)R_H$ (12) and $R_3 = 5R_H$ (5), that is, implemented with just 27 QHE elements, can be employed to calibrate a $1 \text{ M}\Omega$ resistance standard.

More generally, if p_1, p_2, p_3, q_1, q_2 and q_3 are suitable integer factors of the integers p and q , a bridge with $R_1 = (p_1/q_1)R_H$, $R_2 = (q_2/p_2)R_H$ and $R_3 = (p_3/q_3)R_H$ can be employed to calibrate the resistance

$$R_x \approx \frac{p}{q}R_H = \frac{p_1 p_2 p_3}{q_1 q_2 q_3}R_H = \frac{R_1 R_3}{R_2}, \quad (3.38)$$

This configuration requires fewer QHE elements than those of a QHARS with resistance $(p/q)R_H$ and allows the effect of the lead resistances to be minimized by adjusting the combining network composed of r_1 and r_4 .

Chapter 4

Four-terminal-pair fully-digital impedance bridge

The SI units of electrical impedance ohm and farad are linked by the relation $1\ \Omega = 1\ \text{F}^{-1}\text{s}$ (section 1.2.1). To realize the farad, the SI brochure [16] suggests to employ a quadrature bridge, that is, a double product impedance bridge [218] [6, Sec. 4.6.5] that compares two resistors R_1, R_2 and two capacitors C_1, C_2 at a properly chosen fixed angular frequency ω .

The standard implementation of the quadrature bridge principle [114, 168–170, 219] is a very complex electrical network, composed of many electromagnetic components, requiring skillfull operations to perform the whole balance procedure. The automation of the quadrature bridge is possible, but not straightforward [171, 220]. Digitally-assisted quadrature bridge implementations [125, 144], employed at IN-RIM in the traceability chain for the realization of the farad from the DC QHE (section 1.4.2), reduce the network complexity and allow for partial automation. Moreover, since the quadrature bridge calibrates only the product $C_1 C_2$, an additional measurement with a ratio bridge is necessary to factor out the two separate values C_1 and C_2 .

The resistors R_1 and R_2 should be either resistance standards traceable to the DC QHR and with a calculable frequency dependence [117, 125, 172], or AC QHRs themselves [51, 219], of which the parasitic effects must be carefully considered [52, 183], as introduced in section 1.3.3. It is worth noting that, worldwide, only one quadrature bridge with two QHE devices in a single cryostat is permanently operating [51], resulting in a complex and massive experiment filling an entire laboratory.

As introduced in section 1.4.2, a single resistor R and a single capacitor C can be compared by means of fully-digital bridges [135, 140, 163, 221, 222], which are much simpler bridge networks allowing automation and thus employable in the industrial production. Together with the increasing availability of graphene QHRs, which, as discussed in section 1.3.1, require a simpler experimental environment [75], the fully-digital approach allows a quantum realisation of the farad unit that can be

employed by more metrology institutions and calibration centers in the industry.

This section presents a four-terminal-pair fully-digital bridge for the accurate comparison of a single capacitance standard C , having nominal value 8 nF, with a single resistance standard R , of nominal value $R_H = R_K/2 = 12\,906\,\Omega$. The comparison is performed at frequency $f \approx 1541$ Hz, so that the relationship $\omega RC = 1$ is fulfilled. The integer value $C = 8\text{ nF} = 2^3\text{ nF}$ allows the efficient scaling to the decadal values, interesting for dissemination. The frequency $f = 1541$ Hz is close to $1592\text{ Hz} \approx 10/(2\pi)$ krad, a *de facto* standard frequency for capacitance dissemination and intercomparisons [223]. This bridge is thus suitable for the realisation of the farad. The integration of an AC QHR system is under development and is not here reported.

This section is focused on the bridge description and measurement capabilities. The principle of operation of the bridge is presented in section 4.1. The implementation of the bridge, presented in section 4.2, is a very simple network, based on a multi-channel polyphase digital sinusoidal waveform generator [224]; the bridge balance procedure is semi-automated, and the duration of an individual measurement is in the order of 20 minutes. Section 4.3 discusses the uncertainty sources and reports the uncertainty budget. The resulting transfer uncertainty is 1.9×10^{-7} . A validation of the bridge performance is presented in section 4.4, based on the comparison between the capacitor calibration performed with the four-terminal-pair fully-digital bridge and that performed with the traceability chain of the Italian national standard of capacitance [125] reported in 1.4.2. The two methods yielded compatible results.

For this reason, the traceability chain presented in figure 4.1, composed of the fully-digital bridge and a graphene AC QHR system, is intended to replace the current traceability chain.

4.1 Principle of operation

Figure 4.2 shows the principle schematic of a four-terminal-pair voltage-ratio fully-digital impedance bridge. The coaxial shield and terminal pairs, and a number of auxiliary components are here omitted for simplicity (the complete schematic is reported in section 4.2).

A polyphase digital sinusoidal waveform generator operating at frequency f synthesizes the driving voltages and currents E_1, E_2, E_0, E_L, I_1 and I_2 , each one corresponding to an output channel of the generator, which can be individually adjusted both in magnitude and phase¹. E_1 and E_2 are the bridge main voltages; E_L, I_1 and I_2 are auxiliary sources that realize the impedance definition; and the

¹In the following, quantity symbols represent complex phasors associated to real voltage and current signals, or complex impedances.

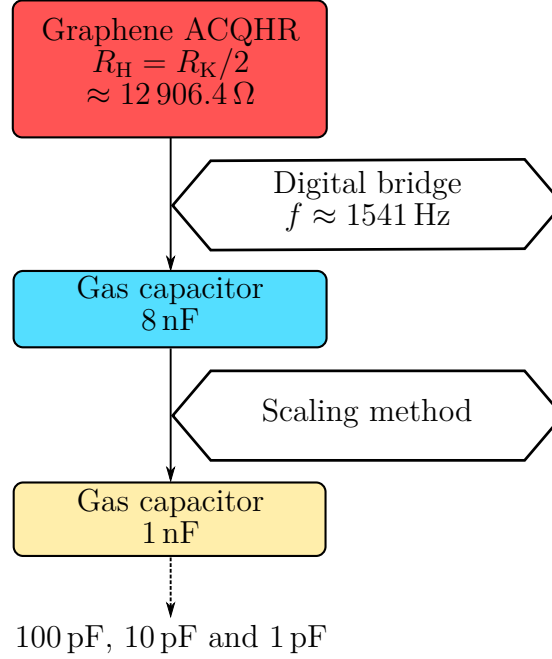


Figure 4.1: Diagram of the traceability chain of the farad intended to replace the current one at INRIM. A four-terminal-pair fully-digital impedance bridge allows the direct calibration of an 8 nF gas capacitor against a graphene AC QHR with nominal value $R_H = R_K/2 \approx 12\,906\ \Omega$ at a frequency $f = 1541\ \text{Hz}$.

auxiliary injection voltage E_0 , together with the injection impedance Z_0 , is used to fine-tune the bridge balance.

Z_1 and Z_2 are the impedances under comparison, with terminals HC1, HP1, LC1 and LP1, and with terminals HC2, HP2, LC2 and LP2, respectively. In the implementation herewith described, Z_1 is the reference impedance, which can be either a QHR with resistance R_H or a calibrated standard resistor with nominal resistance R_H , such that $Z_1 \approx R_H$; Z_2 is a capacitor with capacitance C , such that $Z_2 \approx 1/(j2\pi fC)$; and f is chosen so that $2\pi fR_H C \approx 1$ (that is, $Z_1/Z_2 \approx j$).

By adjusting E_2 (or E_1), E_0 , E_L , I_1 and I_2 , the bridge can be balanced to have $V_{LP1} = V_{LP2} = 0$ and $I_{HP1} = I_{HP2} = 0$. The balance is checked by cycling the synchronous detector D, referenced at the frequency f , through the terminals LP1, LP2, HP1 and HP2. This sequence detects the voltages V_{LP1} and V_{LP2} , and the currents I_{HP1} and I_{HP2} through the current transformers CT₁ and CT₂. The details of the balance procedure are discussed in section 4.2.

When the bridge is balanced, the impedance ratio Z_1/Z_2 is directly compared with the voltage ratio E_1/E_2 , as described by the following balance equation:

$$W = \frac{Z_1}{Z_2} = -\frac{E_1}{E_2} \left(1 + \frac{E_0/Z_0}{E_1/Z_1} \right). \quad (4.1)$$

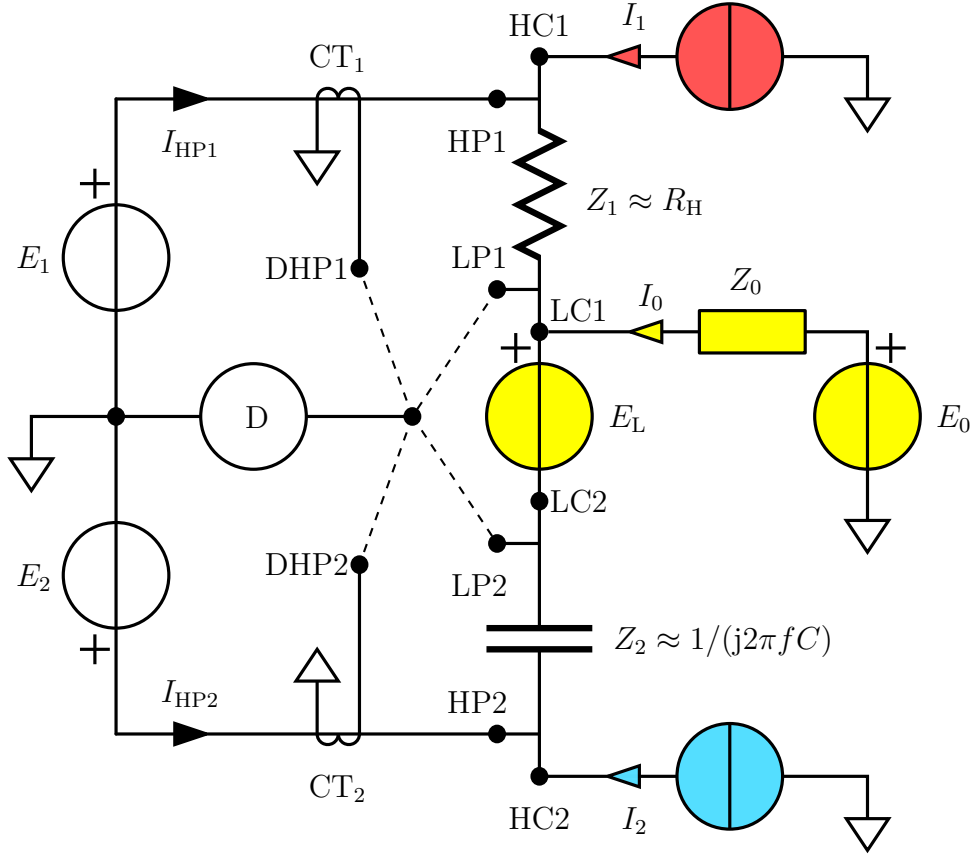


Figure 4.2: Simplified principle schematic of the bridge. $Z_1 \approx R_H$ and $Z_2 \approx 1/(j2\pi fC)$ are the impedances under comparison; f is the bridge operating frequency, chosen so that $2\pi fR_H C \approx 1$; E_1 and E_2 are the main voltages of the bridge; I_1 and I_2 are the current sources used to balance I_{HP1} and I_{HP2} ; E_L is the voltage source used to balance the difference $V_{LP1} - V_{LP2}$; $CT1$ and $CT2$ are current transformers used to measure the currents I_{HP1} and I_{HP2} , respectively; the voltage source E_0 , together with the impedance Z_0 , constitutes an auxiliary injection arm used to fine-tune the bridge balance; and D is a synchronous detector connected, in turn, to the detection terminals $LP1$, $LP2$, $DHP1$ and $DHP2$.

Alternatively, for the admittances $Y_1 = 1/Z_1$, $Y_2 = 1/Z_2$ and $Y_0 = 1/Z_0$, the balance equation is

$$W = \frac{Y_2}{Y_1} = -\frac{E_1}{E_2} \left(1 + \frac{E_0 Y_0}{E_1 Y_1} \right). \quad (4.2)$$

The above equations mean that by choosing $|Z_0| \gg |Z_1|$, the bridge balance can be fine-tuned around the ratio $-E_1/E_2$ by adjusting the voltage E_0 . This procedure allows to achieve the highest measurement accuracy, as described below.

The readings E_1^{read} and E_2^{read} corresponding to the voltage phasors E_1 and E_2 can be obtained from the fundamental components at frequency f of the Fourier series representing the samples used to synthesize the two waveforms.

The readings are affected by the generator gain and nonlinearity errors, such that the actual voltages are $E_k = [1 + g_k(E_k^{\text{read}})]E_k^{\text{read}}$, $k = 1, 2$, being $g_k(E_k^{\text{read}})$ the possibly voltage-dependent complex gain error (for magnitude and phase errors). This is actually the main source of error in fully-digital bridges [135, 225].

The error described above can be completely eliminated by performing two measurements, imposing that the samples used to generate E_1 and E_2 are *exactly* the same in the two configurations, at most shifted in time. In the first measurement (*forward* configuration) the impedances are connected as shown in figure 4.2; in the second measurement (*reverse* configuration) the position of the two impedances is reversed. As introduced at the beginning of this section, the magnitude of the impedance ratio has to be about 1 in both the forward and reverse configurations, so that $|Z_2/Z_1| \approx |Z_1/Z_2| \approx 1$, and the phase change has to be about 180° , because $\arg(Z_2/Z_1) = -\arg(Z_1/Z_2) \approx 90^\circ$. In the reverse configuration, the bridge can be thus balanced by simply changing the sign of all the samples of either E_1 or E_2 , and by adjusting the injection voltage E_0 .

By writing the balance equations for the forward (F subscript) and reverse (R subscript) configurations as

$$W = W_F = -\frac{E_{1F}}{E_{2F}} \left(1 + \frac{E_{0F}Y_0}{E_{1F}Y_1} \right), \quad (4.3)$$

$$W = W_R = -\frac{E_{2R}}{E_{1R}} \left(1 + \frac{E_{0R}Y_0}{E_{2R}Y_1} \right), \quad (4.4)$$

the impedance ratio is

$$W = \sqrt{W_F W_R}. \quad (4.5)$$

The complex square root in (4.5) should be determined with a positive imaginary part because $W \approx j$.

This means that $E_{1R}/E_{2R} = -E_{1F}/E_{2F}$, *exactly*, by construction of the waveform samples, and thus, from (4.3)–(4.5),

$$W = j \sqrt{\left(1 + \frac{E_{0F}Y_0}{E_{1F}Y_1} \right) \left(1 + \frac{E_{0R}Y_0}{E_{2R}Y_1} \right)}. \quad (4.6)$$

Therefore, this procedure completely cancels the main source of error due to the generator nonlinearity (other sources of error are discussed in section 4.3).

The capacitance C is finally determined, from W and the impedance Z_1 , as

$$C = \frac{1}{2\pi f} \operatorname{Im} \frac{W}{Z_1} = \frac{1}{2\pi f} \operatorname{Im}(WY_1), \quad (4.7)$$

being Im the imaginary part of its argument.

4.2 Implementation

Figure 4.3 shows the coaxial schematic of the bridge.

The implementation of the bridge, as shown in figure 4.4, is based on an adjustable polyphase digital sine wave generator ² [227] (UZG signal source). This digital signal source is composed of 18 bit digital-to-analogue converters (DACs) with selectable ranges of 1 V, 2.5 V, 5 V and 10 V, and isolated precision filter/buffer output stages [228]. The relative amplitude and phase stability for this source is of the order of 10^{-7} h^{-1} . A National Instruments NI-DAQ 6541 Board generates the digital samples.

The clock of the UZG digital source is locked to the INRIM 10 MHz atomic frequency standard.

The bridge can be implemented with the seven independent output channels provided by the UZG digital source. Two channels generate the voltages E_1 and E_2 , which are necessary to obtain the reference voltage ratio against which the impedance ratio is compared. Three channels generate the voltages E_3 , E_4 and E_L , composing the auxiliary circuits used to realize the four terminal-pair impedance definition. The currents I_1 and I_2 , generated by E_3 and E_4 through two 100Ω series S102 Vishay resistances, are adjusted to null the currents I_{HP1} and I_{HP2} , measured at the positions V_{DHP1} and V_{DHP2} through the 1 : 200 feedthrough transformers CT_1 and CT_2 , respectively. The voltage E_L , obtained from the voltage E_5 through a 200 : 1 feedthrough injection voltage transformer, is adjusted to null the voltages V_{LP1} and V_{LP2} . One channel generates the voltage E_0 , providing, together with the $C_0 = 1 \text{ pF}$ capacitor, the auxiliary injection for the minimization of the uncertainty in the 1:1 ratio configuration. One last channel generates the signal adopted as a reference by the detector.

To isolate the source outputs E_1 and E_2 from the capacitive loads and avoid possible high-frequency oscillations, two 10Ω resistors are series-connected to the outputs. Furthermore, to ensure a symmetric loading of the source channels in both forward and reverse configurations, two dummy load impedances $C_L \approx C$ and $R_L \approx R_H$ are added at the HC terminals of Z_1 and Z_2 .

The phase-sensitive detector employed for the bridge implementation is a Stanford Research SR830 lock-in amplifier, which is manually switched across the positions V_{DHP1} , V_{DHP2} , V_{LP1} and V_{LP2} .

A software was purpose-coded in the LabWindows environment, based on the balancing algorithm described in [131], to control the UZG digital source and the detector. The bridge balance procedure can be thus semi-automatically carried out in about 20 min.

²This is a bespoke generator developed by Janusz Kaczmarek and Ryszard Rybski, University of Zielona Góra UZG, Poland, in the framework of the European project EMRP SIB53 AIM QuTE, *Automated impedance metrology extending the quantum toolbox for electricity* [226]

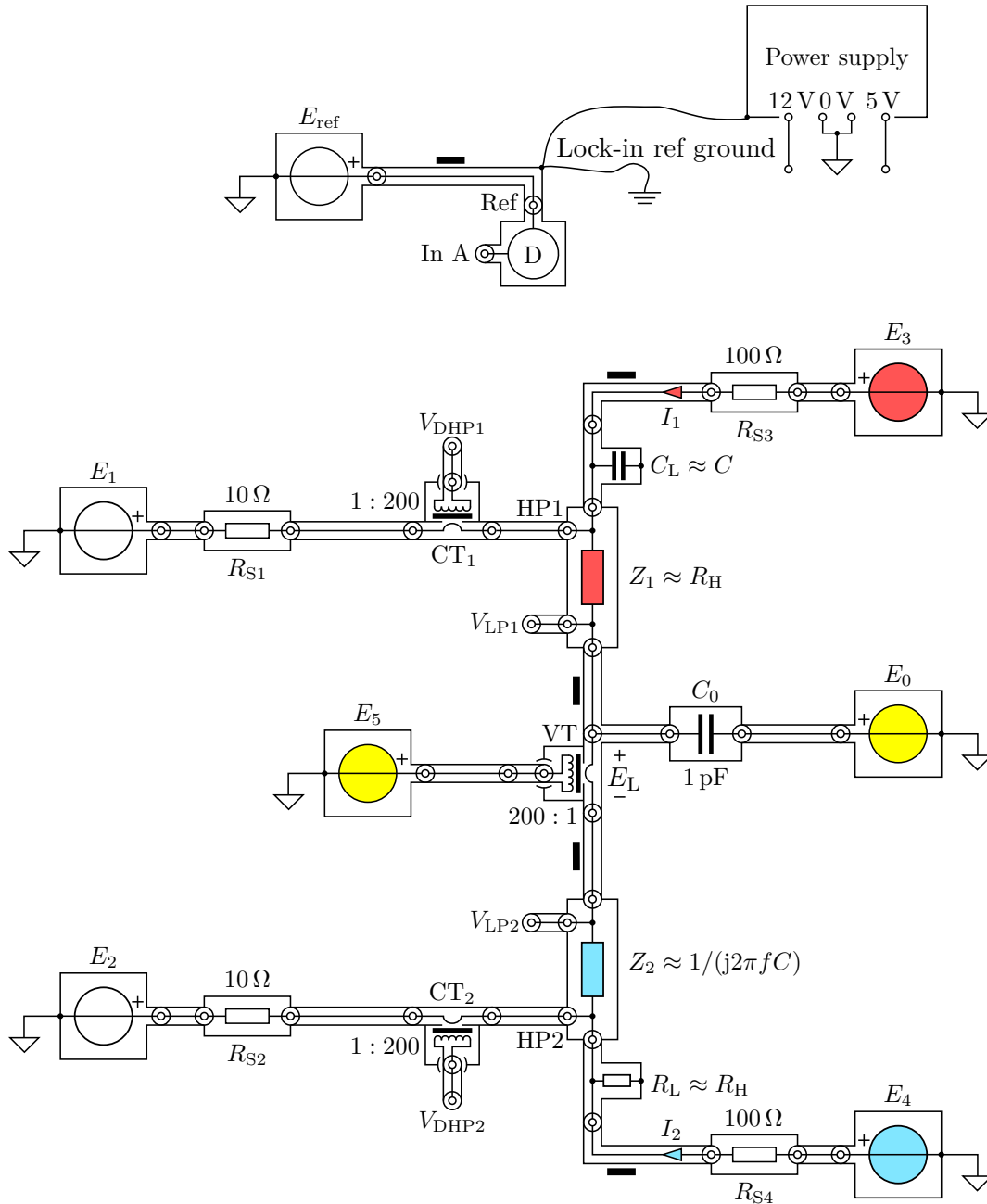


Figure 4.3: Coaxial implementation of the corresponding principle schematic of figure 4.2. The generation of E_L and the detection of V_{DHP1} and V_{DHP2} are carried out by the injection/detection transformers VT, CT1 and CT2. The black rectangles along the arms connecting the two impedances Z_1 and Z_2 between each other and with E_3 and E_4 represent four coaxial equalizers.

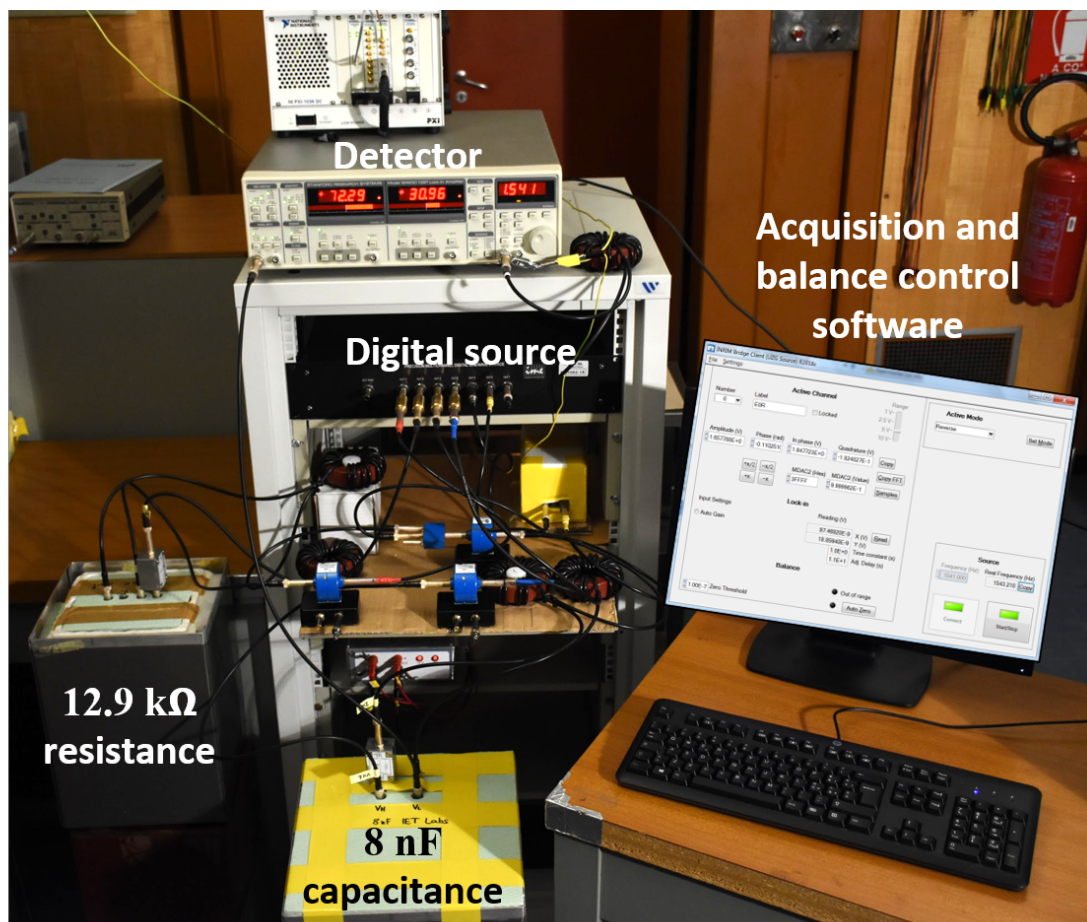


Figure 4.4: Photograph of the bridge implementation. The standards are normally kept in a temperature-controlled chamber not shown in the picture.

The auxiliary injections E_0 can be minimized by presetting the main voltages E_1 and E_2 in the following way:

1. Disconnect E_3 and E_4 from the bridge.
2. Set $E_0 = E_5 = 0$, and E_1 to the operating value of interest.
3. In the forward configuration, connect the detector to V_{LP1} and adjust E_2 to null the detector reading. Once achieved the balance, record the voltage reading E_{2F}^{read} .
4. In the reverse configuration, connect the detector to V_{LP1} and adjust E_2 to null the detector reading. Once achieved the balance, record the voltage reading E_{2R}^{read} .
5. In the forward configuration, set E_2 to the average $E_2 = (E_{2F}^{\text{read}} - E_{2R}^{\text{read}})/2$.

6. Reconnect E_3 and E_4 .

The measurement procedure consists then of the following steps:

1. Set the bridge in the forward configuration.
2. Ground the two ports V_{LP1} and V_{LP2} .
3. Connect the detector to V_{DHP1} and adjust E_3 to null the detector reading.
4. Connect the detector to V_{DHP2} and adjust E_4 to null the detector reading.
5. Leave V_{LP1} grounded and open V_{LP2} . Connect the detector to V_{LP2} and adjust E_5 to null the detector reading.
6. Open V_{LP1} and V_{LP2} . Connect the detector to V_{LP1} and adjust E_0 to null the detector reading.
7. Connect again the detector to the voltage ports V_{DHP1} , V_{DHP2} , V_{LP1} and V_{LP2} to check the voltage readings. If the voltage readings are not all null repeat the steps 2-6 until all the voltages are balanced.
8. Set the bridge in the reverse configuration and reverse the sign of E_2 .
9. Ground the two ports V_{LP1} and V_{LP2} .
10. Connect the detector to V_{DHP1} and adjust E_3 to null the detector reading.
11. Connect the detector to V_{DHP2} and adjust E_4 to null the detector reading.
12. Leave V_{LP1} grounded and open V_{LP2} . Connect the detector to V_{LP2} and adjust E_5 to null the detector reading.
13. Open V_{LP1} and V_{LP2} . Connect the detector to V_{LP1} and adjust E_0 to null the detector reading.
14. Connect again the detector to the voltage ports V_{DHP1} , V_{DHP2} , V_{LP1} and V_{LP2} to check the voltage readings. If the voltage readings are not all null repeat the steps 2-6 until all the voltages are balanced.
15. Calculate W from the balance equations (4.3)–(4.5).
16. The capacitance C is finally determined, from W and the impedance Z_1 , as (4.7).

4.3 Uncertainty sources and budget

The evaluation of the uncertainty for the ratio $W = Z_1/Z_2$, defined by (4.5), is here described by analysing separately all the uncertainty sources, which are then combined in a complete measurement model reported in the uncertainty budget.

From the balance equations (4.3)–(4.5), it is possible to write the bridge readings³

$$W_F^{\text{read}} = -\frac{E_{1F}^{\text{read}}}{E_{2F}^{\text{read}}} \left(1 + \frac{E_{0F}^{\text{read}} Y_0}{E_{1F}^{\text{read}} Y_1} \right), \quad (4.8)$$

$$W_R^{\text{read}} = -\frac{E_{2R}^{\text{read}}}{E_{1R}^{\text{read}}} \left(1 + \frac{E_{0R}^{\text{read}} Y_0}{E_{2R}^{\text{read}} Y_1} \right) \quad (4.9)$$

so that

$$W^{\text{read}} = \sqrt{W_F^{\text{read}} W_R^{\text{read}}}. \quad (4.10)$$

4.3.1 Crosstalk

By considering the crosstalk, that is, the coupling of the voltage generated by one channel on that generated by another channel, the voltages E_1 and E_2 can be written as

$$E_1 = E_1^{\text{read}} + a_{12} E_2^{\text{read}} + a_{10} E_0^{\text{read}}, \quad (4.11)$$

$$E_2 = E_2^{\text{read}} + a_{21} E_1^{\text{read}} + a_{20} E_0^{\text{read}}, \quad (4.12)$$

being a_{ij} the coupling coefficient from channel j to channel i , and considering only the channels that may induce significant variations when switching between the forward and reverse configurations.

Because of the crosstalk phenomenon, the relationship $E_{1R}/E_{2R} = -E_{1F}/E_{2F}$ is affected by an error. By combining (4.11) and (4.12) with (4.3)–(4.5), and simplifying, it results that, at the first order in the coupling coefficients,

$$W = W^{\text{read}} - \Delta W^{\text{CT}} \quad (4.13)$$

being ΔW^{CT} the crosstalk error

$$\begin{aligned} \frac{\Delta W^{\text{CT}}}{W^{\text{read}}} \approx & -\frac{1}{2} \left[a_{12} \left(\frac{E_{2F}^{\text{read}}}{E_{1F}^{\text{read}}} - \frac{E_{2R}^{\text{read}}}{E_{1R}^{\text{read}}} \right) - a_{21} \left(\frac{E_{1F}^{\text{read}}}{E_{2F}^{\text{read}}} - \frac{E_{1R}^{\text{read}}}{E_{2R}^{\text{read}}} \right) \right. \\ & \left. + a_{10} \left(\frac{E_{0F}^{\text{read}}}{E_{1F}^{\text{read}}} - \frac{E_{0R}^{\text{read}}}{E_{1R}^{\text{read}}} \right) - a_{20} \left(\frac{E_{0F}^{\text{read}}}{E_{2F}^{\text{read}}} - \frac{E_{0R}^{\text{read}}}{E_{2R}^{\text{read}}} \right) \right]. \quad (4.14) \end{aligned}$$

³In the following, as introduced in section 4.1, the subscripts “F” and “R” designate quantity values obtained in the forward and reverse configurations, respectively; the superscript “read” designates quantity values read off the generator settings, as described in section 4.1.

4.3.2 High and low balances

A measurement error occurs when the four-terminal-pair impedance definition is not perfectly fulfilled. When the currents at the ports HP1 and HP2 are not perfectly compensated by adjusting I_1 and I_2 , a measurement error is caused by the voltages across R_{S1} and R_{S2} , so that

$$W = W^{\text{read}} - \Delta W^{\text{HB}}. \quad (4.15)$$

The measurement error ΔW^{HB} is

$$\frac{\Delta W^{\text{HB}}}{W^{\text{read}}} \approx \frac{1}{2} \left[\frac{R_{S1}}{Z_m} \left(\frac{V_{\text{DHP1F}}}{E_{1F}^{\text{read}}} - \frac{V_{\text{DHP1R}}}{E_{1R}^{\text{read}}} \right) - \frac{R_{S2}}{Z_m} \left(\frac{V_{\text{DHP2F}}}{E_{2F}^{\text{read}}} - \frac{V_{\text{DHP2R}}}{E_{2R}^{\text{read}}} \right) \right], \quad (4.16)$$

being Z_m the mutual impedance of the transformers CT1 and CT2, and V_{DHP1F} , V_{DHP1R} , V_{DHP2F} and V_{DHP2R} the residual voltages at the secondary windings of CT1 and CT2 at the end of the balance procedures for the forward and reverse configurations.

When the voltages V_{LP1} and V_{LP2} are not perfectly nulled, the voltages across the impedances Z_1 and Z_2 do not coincide with E_1 and E_2 and a leakage current due to the stray capacitance C_L flows from the low ports toward ground (including C_0). This causes a measurement error such that, since $V_{\text{LP}} = (V_{\text{LP1}} + V_{\text{LP2}})/2$, $\Delta V_{\text{LP}} = V_{\text{LP1}} - V_{\text{LP2}}$ and $Y_L = j2\pi f C_L$,

$$W = W^{\text{read}} - \Delta W^{\text{LB}} \quad (4.17)$$

being the measurement error ΔW^{LB} given by

$$\begin{aligned} \frac{\Delta W^{\text{LB}}}{W^{\text{read}}} \approx & \frac{1}{2} \left[\left(1 + \frac{Y_2}{Y_1} + \frac{Y_L}{Y_1} \right) \left(\frac{V_{\text{LPF}}}{E_{1F}^{\text{read}}} + \frac{V_{\text{LPR}}}{E_{2R}^{\text{read}}} \right) \right. \\ & \left. + \left(1 - \frac{Y_2}{Y_1} \right) \left(\frac{\Delta V_{\text{LPF}}}{2E_{1F}^{\text{read}}} - \frac{\Delta V_{\text{LPR}}}{E_{2R}^{\text{read}}} \right) \right]. \end{aligned} \quad (4.18)$$

The balance procedure, described in section 4.2, corresponds to the common component V_{LP} and the differential component ΔV_{LP} resulting from the decomposition of V_{LP1} and V_{LP2} .

4.3.3 Injection

The voltage ratios E_{0F}/E_{1F} , E_{0R}/E_{2R} composing, together with the impedances Y_0 and Y_1 , the injection terms of (4.3) and (4.4), can be written as

$$\frac{E_{0F}}{E_{1F}} = (1 + g_{01}) \frac{E_{0F}^{\text{read}}}{E_{1F}^{\text{read}}} \quad (4.19)$$

and

$$\frac{E_{0R}}{E_{2R}} = (1 + g_{02}) \frac{E_{0R}^{\text{read}}}{E_{2R}^{\text{read}}}. \quad (4.20)$$

The complex error terms g_{01} and g_{02} represent the generator nonlinearity introduced in section 4.1.

The uncertainty contributions of the impedances Y_0 and Y_1 are typically negligible.

4.3.4 Measurement model and uncertainty budget

By combining all the obtained uncertainty components with (4.6), the complete measurement model is

$$W = j \sqrt{\left[1 + (1 + g_{01}) \frac{E_{0F}^{\text{read}} Y_0}{E_{1F} Y_1} \right] \left[1 + (1 + g_{02}) \frac{E_{0R}^{\text{read}} Y_0}{E_{2R} Y_1} \right] - \Delta W^{\text{CT}} - \Delta W^{\text{LB}} - \Delta W^{\text{HB}}}. \quad (4.21)$$

An example of a preliminary uncertainty budget for the quantity $V = \text{Im } W - 1$ (because $W \approx j$) is reported in table 4.1⁴.

Table 4.1: Preliminary uncertainty budget for $V = \text{Im } W - 1$.

i	Quantity	Type	$u_i(V)$
1	Bridge reading ($n = 10$)	A	0.5×10^{-7}
2	Crosstalk (ΔW^{CT})	B	1.7×10^{-7}
3	Low balance (ΔW^{LB})	B	0.7×10^{-7}
4	High balance (ΔW^{HB})	B	0.2×10^{-7}
5	Injection	B	0.1×10^{-7}
RSS			1.9×10^{-7}

The first uncertainty component is that associated to the bridge reading, consisting of $n = 10$ measurements in both forward and reverse configurations. The total measurement time is of about 200 min and the type A uncertainty component is 5×10^{-8} .

The second uncertainty component, associated to the crosstalk term ΔW^{CT} , is the most significant component and can be evaluated from (4.14). The measured coupling coefficients between the different channels of the polyphase generator are of

⁴The uncertainty budget is calculated by means of the measurement uncertainty calculator METAS UncLib [229].

about -140 dB in magnitude, with a rather high phase uncertainty, conservatively rounded off to 2π .

The third and fourth uncertainty components, associated to ΔW^{LB} and ΔW^{HB} , are evaluated from (4.18) and (4.16). The thresholds applied to stop the balance procedure at the various detection points were set to 50 nV for V_{LP} and ΔV_{LP} , 200 nV for V_{DHP1} and V_{DHP2} . The measured mutual impedance of the current transformers is $Z_{\text{m}} \approx (145 - 190i) \Omega$.

The combined uncertainty is $u(V) \approx 1.9 \times 10^{-7}$, which is competitive for the primary realization of the unit of capacitance.

4.4 Comparison with a transformer ratio bridge

A preliminary validation of the bridge performance was obtained by comparing the 8 nF capacitor calibration at $f \approx 1541$ Hz performed with the four-terminal-pair fully-digital bridge C^{fd} with that performed with the traceability chain of the Italian national standard of capacitance [125] C^{ref} (reported in 1.4.2).

4.4.1 Experimental set-up

Figure 4.5 shows the measurement chain adopted in the preliminary validation process.

The calibration result C^{ref} is obtained by means of the traceability chain of figure 1.20 currently employed to calibrate the 1 nF Italian national standard of capacitance against a $12\,906 \Omega$ quadrifilar resistance standard, in turn calibrated against the DC QHR. The quadrifilar resistor usually employed is here substituted by the resistance standard of nominal value $R_{\text{H}} = R_{\text{K}}/2 \approx 12\,906 \Omega$ employed in the calibration with the four-terminal-pair fully-digital bridge. The typical calibration procedure is then performed. A 8 : 1 transformer-based resistance ratio bridge is employed to calibrate two resistance standards of nominal value $R \approx 8R_{\text{H}} \approx 103.251 \text{ k}\Omega$ against the $12\,906 \Omega$ resistance standard. These resistance standards are then employed in a transformer-based quadrature bridge to calibrate the product of two 1 nF capacitance standards. The calibration of a single 1 nF capacitance standard is then obtained by means of a capacitance ratio bridge. The resulting calibration of a 1 nF capacitor is then scaled to the 8 nF is performed by means of a 1 : 8 transformer-based ratio bridge.

During the measurement procedure, the 8 nF capacitance standard is kept in a temperature-controlled chamber (Kambič TK-190 US) with a temperature stability better than 4 mK [230]. Since the temperature coefficient of the capacitance standard is $(4 \pm 6) \times 10^{-6} \text{ }^\circ\text{C}^{-1}$ [231], the maximum effect due to temperature dependence is about 4×10^{-8} and can be considered virtually negligible with respect to the other uncertainty components.

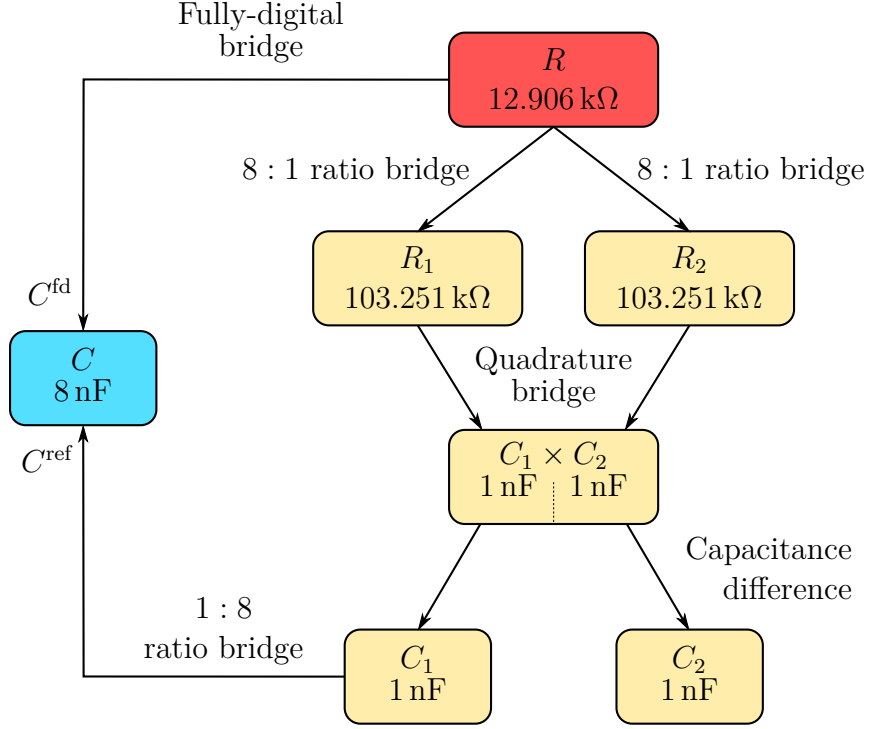


Figure 4.5: Diagram representing the procedure adopted to compare the calibration of the 8 nF capacitance standard performed with the four-terminal-pair fully-digital bridge and that performed with the traceability chain of the Italian national standard of capacitance.

The calibration result C^{fd} is obtained by means of the four-terminal-pair fully-digital bridge, of which the measurement procedure is described in section 4.2.

4.4.2 Results

The result of the comparison between the two calibration methods is δ , the relative difference between C^{fd} and C^{ref} , that is,

$$\delta = \frac{C^{\text{fd}} - C^{\text{ref}}}{C^{\text{ref}}} = \frac{\text{Im } W^{\text{fd}} - \text{Im } W^{\text{ref}}}{\text{Im } W^{\text{ref}}}. \quad (4.22)$$

The final results of δ of three comparisons, performed as described in figure 4.5, are represented in figure 4.6. The driving rms voltages $|E_1| = |E_2| \approx 0.25 \text{ V}$ are chosen so that, in both calibration methods, the same driving current flows in the resistance standard.

The uncertainty bars represent the expanded uncertainties with coverage factor $k = 2$.

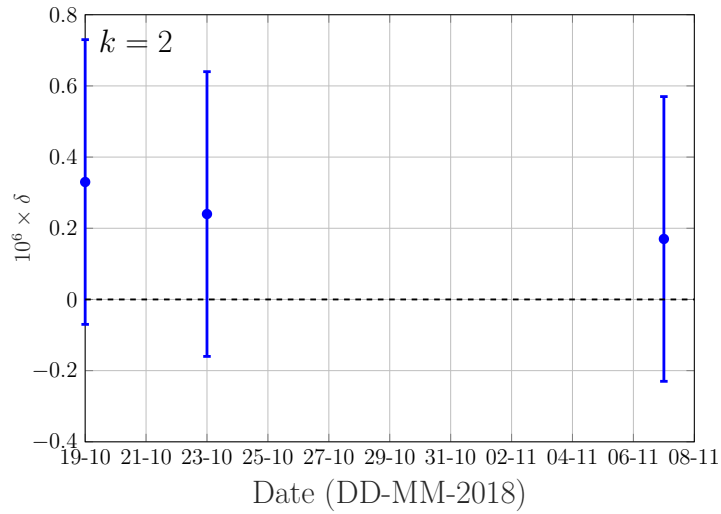


Figure 4.6: Summary plot of the final results δ of three comparisons, performed as described in figure 4.5. δ is estimated from (4.22) and represents the difference between the calibration performed with the four-terminal-pair fully-digital bridge and that performed with the traceability chain of the Italian national standard of capacitance. The uncertainty bars represent the expanded uncertainties with coverage factor $k = 2$.

Figure 4.6 shows that the two methods yield results compatible within a few parts in 10^7 , which is the uncertainty level of both the calibration systems.

For this reason, the fully-digital bridge is a good candidate to replace the transformer-based impedance bridges currently employed in the traceability chain of farad.

Chapter 5

Conclusions

This dissertation reported my work on some theoretical and experimental methods of interest for the field of resistance and impedance metrology. The work on this methods is still ongoing and I shortly present here some possible future directions of research.

In chapter 2, a general method to analyze complex measuring circuits is applied to the simulation of interconnected networks of QHE elements, such as QHARS. The method is implemented as a Mathematica application, the `QHARSmachine`, which estimates the error of a QHARS as a probability distribution simulated with a Monte Carlo analysis on the basis of the layout of the circuit network and the set of stray resistances of all interconnections. As example, the `QHARSmachine` is applied to an existing $1\text{ M}\Omega$ QHARS fabricated by the NMIJ [1]. The result of the simulation predicts a deviation from the nominal value of practical negligible magnitude. The application is distributed under the GNU General Public License in the online repository [191].

The `QHARSmachine` can be extended to simulate other networks, such as QHE voltage dividers or bridges, or can be employed already in the design phase, to optimize the connection layout. As example, an analytical version of the `QHARSmachine` (reported in appendix A.2) was developed to analyze the quantum Hall Kelvin bridge to evaluate the effect of the major lead and contact resistances of the bridge [3]. The `QHARSmachine` can be also extended to analyze circuits in the AC regime, both analytically and numerically.

The `QHARSmachine` (and its extensions) and the SPICE macro-model of a QHE element (see section 2.5) can be employed for different types of analyses.

For example, SPICE QHE elements macro-models can be employed to perform SPICE simulations of pn-junction graphene QHARS [2], reducing the measurement time and simplifying the procedure needed to characterize the devices.

The macro-models can be also employed to simulate the effect of the stray impedances of a QHE device interconnected to a measuring system in the AC regime. Different designs can be investigated, to understand the best configurations

which minimize the stray parameters effect.

A part of the project EMPIR 18SIB07 GIQS, *Graphene impedance quantum standard* is focused on the extension of the models to real QHE elements, taking into account its nonlinearities and stray parameters, such as the longitudinal resistance, the stray impedances and the effect of frequency in the AC regime.

Chapter 3 presents the design and implementation of a DC quantum Hall effect Kelvin resistance bridge for the direct calibration of four-terminal resistance standards operating at room temperature [3, 4]. The bridge-on-a-chip implementation, based on a graphene QHARS fabricated at NIST, is simple and robust. The system requires only few leads to connect the room temperature standard resistor and the measuring electronics. Moreover, with this method, only two room temperature electronic instruments of standard accuracy are necessary for the calibration of four-terminal resistance standards operating at room temperature. The calibration accuracy of an artefact standard resistor with nominal value R_H is at the level of a few parts in 10^9 (standard uncertainty). The calibration results are compatible within a few parts in 10^9 with that of the state-of-the-art calibration bridge, the CCC.

With respect to a calibration performed with a CCC against a QHR, the quantum Hall Kelvin bridge operates in a single cryogenic environment. The bridge can thus operate in a dry cryocooler, even of small size when graphene is adopted for the QHE elements. Moreover, depending on the voltmeter, the noise rejection is expected to be significantly higher than that of the DCC or CCC instruments.

The usage of QHARS can extend the operation of the quantum Hall Kelvin bridge to resistance standards of arbitrary nominal value.

Resistance standards with nominal values different from R_H (for instance, equal to decadal values) can be directly calibrated by modifying the quantum Hall Kelvin bridge-on-a-chip. A QHE element can thus be replaced by a QHARS in one or more arms of the bridge. If a QHARS is employed in each bridge arm, the number of the required QHE elements is reduced with respect to a resistance comparison with a single QHARS.

Chapter 4 presents a four terminal-pair fully-digital impedance bridge operating in a 1 : 1 ratio configuration for the direct calibration of an 8 nF standard capacitor against a QHR standard at 1541 Hz. The evaluated uncertainty is of about 2×10^{-7} . The current Italian traceability chain for the farad employs transformer-based impedance bridges and requires thus long time and trained personnel to operate. The uncertainty of the system is about 2×10^{-7} . The bridge performance is preliminarily validated by comparing the 8 nF capacitance standard calibration performed with the four-terminal-pair fully-digital impedance bridge and that performed with the transformer-based impedance bridges currently employed in the traceability chain of farad at INRIM. The two systems result to be compatible within few parts in 10^7 .

The four-terminal-pair fully-digital impedance bridge ensure a semi-automated

balance procedure, reducing the time and the experience required to calibrate a standard. The purpose-coded software that balance the bridge semi-automatically is developed from that developed in the framework of the project EMPIR 17RPT04 VersICaL, *A versatile electrical impedance calibration laboratory based on digital impedance bridges*.

The obtained result is a further proof that digital bridges are mature for primary impedance metrology and, in particular, that the 1 : 1 ratio four-terminal-pair fully-digital impedance bridge here presented is suitable for the realization of the farad from the AC QHR. The bridge is implemented in the framework of the project EMPIR 18SIB07 GIQS, *Graphene impedance quantum standard*, as a possible new Italian traceability chain of the farad. The traceability chain will implement a graphene ACQHR experiment, which is being developed at INRIM.

Appendix A

Mathematica notebooks

A.1 QHARSmachine

The complete Mathematica notebook QHARSmachine [1], available in the online repository [191], is reported below. It is based on the DC analysis method presented in section 2.2 and on the workflow of the modelling procedure of figures 2.1 and 2.2.

A.1.1 Initialization

At first, the notebook is initialized, according to the code presented in figure A.1. This clears the notebook parameters and defines the functions constructing the indefinite admittance matrices \bar{Y}_i for the cw and ccw ideal QHE elements (2.4) and (2.5), respectively. It also defines a few useful matrix manipulation functions.

```
ClearAll[file, n, m, l, A, AT, rQn, a, b, c, d, s, wp, rightCirculantMatrix, qheCwIdeal, qheCcwIdeal, takeOperator,
  complementaryIndices, wp, yi, rnSign, epsilonLim, deltaLim, epsilon, delta, result, D, g, Y, Yn, gn, tau, meanResult,
  stdDevResult, h, qheType];

(*The function below is useful for the following definitions*)
rightCirculantMatrix[L_List?VectorQ] := NestList[RotateRight, RotateRight[L], Length[L] - 1]

(*These operators define the Yi IAM matrices of an ideal QHE element (clockwise and counterclockwise)*)
qheCwIdeal[x_Integer] := rightCirculantMatrix[PadLeft[{-1, 1}, x]] /; x >= 2
qheCcwIdeal[x_Integer] := rightCirculantMatrix[Join[{-1}, ConstantArray[0, x - 2], {1}]] /; x >= 2

(* The operators below are taken from http://stackoverflow.com/a/5300892/2522705 *)
takeOperator[w_?MatrixQ, rows_List, cols_List] := w[[rows, cols]]
dropOperator[w_?MatrixQ, rows_List, cols_List] := w[[##]] &@@complementaryIndices[w, rows, cols]
complementaryIndices[w_?MatrixQ, rows_List, cols_List] := Complement@@@Transpose@{Range/@Dimensions@w, {rows, cols}}
```

Figure A.1: Initialization of the QHARSmachine Mathematica notebook.

A.1.2 Converter

The electrical LTspice schematic of the QHARS (see figure 2.3 for an example), saved in a file, is imported by the QHARSMachine, by means of the commands shown in figure A.2. The converter, as described in section 2.3.1, extracts the parameters a, b, c, d and p/q from the comment line of the LTspice schematic, derives the parameters N, M and L , and constructs the interconnection matrix \mathbf{A} (for the corresponding code, see figure A.3). The program requires the user to insert the sample size S and the working precision wp , which are set as $S = 1$ and $wp = 4MachinePrecision$ by default.

```
Module[{fileNetlist = "",
  qharsSchematic = "",
  qharsList = "",
  qharsNetlist = "",
  qheNodes = {},
  resistorNodes = {},
  qharsNodes = {},
  rows = 0},
  Button["Load QHARS Schematic",
    n = 0;
    m = 0;
    l = 0;
    s = {};
    rQn = 1/1;
    wp = 4 MachinePrecision;
    s = 1;
    a = 0;
    b = 0;
    c = 0;
    d = 0;
    file = SystemDialogInput["FileOpen", {NotebookDirectory[], {"LTspice schematic" -> {"*.asc"}, "All files" -> {"*.*"}},
      WindowTitle -> "Choose the QHARS schematic"];
    If[file != $Canceled,
      qharsSchematic = Import[file, "Text"]; (*The program imports the QHARS schematic.*)
      (*The program extracts the parameters a,b (volage nodes) and c,d (current nodes),
      and p/q (nominal resistance value normalized to RH) from the schematic.*)
      ToExpression[StringReplace[StringCases[qharsSchematic, RegularExpression["p/q\\s*=-.+|a\\s*=-.+|b\\s*=-.+|c\\s*=-.+|d\\s*=-.+"],
        {"p/q" -> "rQn"}]];
      (*The program runs LTspice XVIIx64 (in both Windows or Unix OS) and imports the LTspice netlist.*)
      Switch[$OperatingSystem, "Windows", RunProcess[{"XVIIx64.exe", "-netlist", file}], "Unix",
        RunProcess[{"wine", "XVIIx64.exe", "-netlist", TemplateApply["StandardOutput", RunProcess[{"winepath", "-w", file}]} // StringTrim]];
      fileNetlist = FileNameJoin[{FileNameDrop[file], FileBaseName[file] <> ".net"}];
      qharsNetlist = Import[fileNetlist, "Text"];
```

Figure A.2: First portion of the converter. The electrical LTspice schematic of the QHARS (see figure 2.3 for an example), saved in a file, is imported by the QHARSMachine.

A.1.3 Import of the stray parameters spreadsheet

The spreadsheet containing the experimental stray parameters distributions (example portions of the spreadsheet are shown in figure 2.6) is imported, as shown in

```
(+The program extracts the list of the QHE element and resistance nodes. The type of the QHE element (CW or CCW) is
also taken into account.+)
qharsList =
SortBy[ToExpression@StringSplit[StringReplace[StringCases[qharsNetlist, StartOfLine ~~ RegularExpression["XU{^\\n}+\\n"}],
{"qhecw" -> "N0", "qheccw" -> "N1"}], {"XU", Whitespace ~~ "N"}], First][[All, 2 ;;]];
qheType = qharsList[[All, -1]];
qheNodes = qharsList[[All, 1 ;; -2]];
resistorNodes =
SortBy[ToExpression@StringSplit[StringCases[qharsNetlist, StartOfLine ~~ RegularExpression["R{^\\n}+\\n"}], {"R", Whitespace ~~ "N"}][[
All, 1 ;; -2]], First][[All, 2 ;;]];

n = Dimensions[qheNodes][[1]]; (*The number of QHE elements in the QHARS.+)
m = Dimensions[qheNodes][[2]]; (*The number of the QHE element terminals.+)
l = Dimensions[resistorNodes][[1]]; (*The number of resistances in the QHARS.+)
qharsNodes = Join[qheNodes, resistorNodes]; (*The list of the QHARS nodes.+)
rows = n m + 2 l; (*The number of nodes.+)

(+The program creates the interconnection A matrix.+)
A = ConstantArray[0, {rows, Max[qharsNodes]}];
Table[A[[k]][[Flatten[qharsNodes][[k]]]] = 1, {k, rows}];

CreateWindow[CreateDialog[{
Column[{
Row[{"sample size ", InputField[Dynamic[s], Number, ImageSize -> 70]}],
Row[{"working precision ", InputField[Dynamic[wp], ImageSize -> 150]}]
}], CancelButton["OK", DialogReturn[], ImageSize -> 100]
}], WindowFloating -> True, WindowSize -> Fit, WindowTitle -> "Choose the parameters"
1],
ImageSize -> 180, Background -> Orange, BaseStyle -> {14, Bold, White},
Method -> "Queued"]]
```

Figure A.3: Second portion of the converter. The parameters a, b, c, d and p/q are extracted from the comment line of the LTspice schematic, the parameters N, M and L are derived, and the interconnection matrix \mathbf{A} is constructed. The sample size S and the working precision wp can be input.

the code portion of figure A.4.

A.1.4 Solver

The solver implements the analysis method developed in section 2.2 to perform a Monte Carlo simulation of the probability distribution of the deviation $\Delta R_{ab,cd}^Q = R_{ab,cd}^Q - R_{nom}^Q$, as shown in detail in figure 2.2 and described in section 2.3.2. Figure A.5 shows the implementation of the solver in the QHARSmachine Mathematica notebook.

The Monte Carlo subblock generates a random sample of length S (composed of the $\{\epsilon_{nm;s}\}_{s=1,\dots,S}$ and $\{\delta_{l;s}\}$ sequences) extracted from an $(NM + L)$ -dimensional multivariate uniform distribution of the experimental stray parameters, defined as uniform distributions with the endpoints $[\epsilon_{nm}^{\min}, \epsilon_{nm}^{\max}], [\delta_l^{\min}, \delta_l^{\max}]$ imported from the spreadsheet. The multivariate random sample of the NM terminal resistances and of the L lead resistances are thus obtained. The sequences of matrices $\{\bar{\mathbf{Y}}_s\}$ and $\{\bar{\mathbf{Y}}_s^Q\}$, and the sequence of deviations $\{\Delta R_{ab,cd;s}^Q\}$ (representing the simulated probability distribution of $\Delta R_{ab,cd}^Q$) are constructed, according to (2.12), (2.14) and (2.15).

```

Module[{fileExcel = "", epsilonLimits = "", epsilonLimitsDropped = "", deltaLimits = ""},
Button["Load stray parameters Excel spreadsheet",
 $\mathcal{Y}_i = \text{Table}[\text{If}[\text{qheType}[i] == 0, \text{qheCwIdeal}[m], \text{qheCcwIdeal}[m]], \{i, n\}];$  (*The IAM matrix of the N QHE elements.*)
 $\mathcal{A}^T = \mathcal{A}^T;$  (*Transpose of the matrix  $\mathcal{A}$ .*)
rnSign = Sign[c - d] Sign[a - b] (-1)^(1 + 1 + c + d + a + b); (*The sign operator is calculated from the parameters a,b,c and d.*)

(*The program imports the Excel spreadsheet composed of the endpoint of the stray parameter distributions.*)
fileExcel = SystemDialogInput["FileOpen", {DirectoryName[file], {"Excel Files" -> {"*.xlsx"}, "All files" -> {"*.*"}},
WindowTitle -> "Choose the Stray parameters Excel spreadsheet"];

(*The program creates a list of the endpoints of the NxM terminal resistances extracted from the data imported,
by distinguishing the voltage and current terminals.*)
If[fileExcel != $Canceled, epsilonLimits = SetPrecision[Import[fileExcel, {"Data", 2, All, {4, 5}}], wp]];
epsilonLimitsDropped = Drop[epsilonLimits, 1];
epsilonLim =
Flatten[
Table[epsilonLim = List[epsilonLimitsDropped[[1]], epsilonLimitsDropped[[2]], epsilonLimitsDropped[[3]],
epsilonLimitsDropped[[2]], epsilonLimitsDropped[[1]], epsilonLimitsDropped[[2]], epsilonLimitsDropped[[3]],
epsilonLimitsDropped[[2]]], {i, n}], 1];

(*The program creates a list of the endpoints of the L wire resistances extracted from the data imported. *)
If[fileExcel != $Canceled, deltaLimits = SetPrecision[Import[fileExcel, {"Data", 1, All, {6, 7}}], wp]];
deltaLim = Drop[deltaLimits, 1],

ImageSize -> 190, Background -> RGBColor[0.16, 0.58, 0.07], BaseStyle -> {14, Bold, White},
Method -> "Queued"]]

```

Figure A.4: Import of the spreadsheet containing the experimental stray parameters distributions.

As shown in figure A.6, the obtained distribution is plotted as a histogram, which is exported in the same directory of the circuit schematic together with the obtained data (saved in a .wl file) and a copy of the notebook (saved in a .nb file).

A.2 Quantum Hall Kelvin bridge analysis

An analytical version of the QHARSmachine application [1], introduced in section 2 and reported in appendix A.1, analyses the quantum Hall Kelvin bridge with the method described in [9] to evaluate the effect of the major lead and contact resistances of the bridge (see figure 3.12) [1]. The result of the analysis is the relationship (3.15), where the leads error is defined by (3.16).

The Mathematica notebook is reported below.

A.2.1 Initialization

At first, the notebook is initialized, according to the code presented in figure A.7. This clears the notebook parameters and defines the functions constructing the indefinite admittance matrices $\bar{\mathbf{Y}}_i$ for the cw and ccw ideal QHE elements (2.4) and (2.5), respectively. It also defines a few useful matrix manipulation functions.


```

Module[{epsilonRandom = "", deltaRandom = "", e = "", delta = ""}, Button["Run the QHARS machine",
  τ = Timing[(*The time needed to evaluate the script.*)
  result = Table[

    (*The program extracts a random value from each uniform distribution identified by the endpoints.*)
    epsilonRandom = Table[RandomReal[{epsilonLim[[v, 1]], epsilonLim[[v, 2]]}, WorkingPrecision → wp], {v, n * m}];
    deltaRandom = Table[RandomReal[{deltaLim[[w, 1]], deltaLim[[w, 2]]}, WorkingPrecision → wp], {w, 1}];
    epsilon = Flatten[Table[e[[j, k]] → epsilonRandom[[ (j - 1) * m + k]], {j, n}, {k, m}]];
    delta = Table[δ[[w]] → deltaRandom[[w]], {w, 1}];

    (*The program creates the matrix D that identify the terminal resistances.*)
    D = Table[If[qheType[[i]] == 0, RotateLeft[PadLeft[{-e[[i, Mod[j - 1, m] + 1] / 2, 1 + e[[i, j + 1] / 2}], m], m - 1 - j],
      RotateLeft[PadLeft[{1 + e[[i, j + 1] / 2, -e[[i, Mod[j + 1, m] + 1] / 2}], m], m - 2 - j]], {i, 1, n}, {j, 0, m - 1}] /. epsilon];

    (*The program creates the matrix g that identify the wire resistances.*)
    g = Table[{2 / δ[[i]], -2 / δ[[i]], {-2 / δ[[i]], 2 / δ[[i]]}, {i, 1, 1}] /. delta;

    (*The program creates the IAM Y of the N QHE elements, that includes the terminal resistances,
    and the wire resistances. This is a block diagonal matrix and each block represents an element of the QHARS.*)
    Y = DiagonalMatrix[Hold /@ Join[Table[Inverse[D[[i]]].Yi[[i]], {i, 1, n}], g] // ReleaseHold // ArrayFlatten;
    Yn = Y.Y.g; (*Calculate the QHARS IAM Yn.*)

    (*Evaluate the 4-terminal resistance corresponding to the a,b voltage nodes and c,d current nodes,
    and the relative deviation from the nominal value.*)
    rn = rnSign Det[dropOperator[Yn, {c, d}, {a, b}]] / Det[dropOperator[Yn, {1}, {1}]];
    rn N[Denominator[rQn] / Numerator[rQn], wp] - 1,
    {h, s}]; (*The procedure is repeated S times (S is the sample size of the Monte Carlo analysis),
    so that the result is a list of the S relative deviations obtained.*)
  ];
  meanResult = Mean[result]; (*Mean value of the relative variation distribution*)
  stdDevResult = If[s > 1, StandardDeviation[result], Infinity]; (*Standard deviation of the distribution*)

```

Figure A.5: Implementation of the solver in the QHARSmachine Mathematica notebook.

A.2.2 Converter

The electrical LTspice schematic of the bridge (see figure 3.12), saved in a file, is imported by the application, by means of the commands shown in figure A.8. The converter extracts the parameters a, b (voltage terminals of V_D), c, d (current terminals), and e, f (voltage terminals of V) from the comment line of the LTspice schematic, derives the parameters N, M and L , and constructs the interconnection matrix \mathbf{A} , by means of the commands shown in figure A.9. The working precision wp is set as $wp = 4MachinePrecision$ by default.

A.2.3 Solver

The solver implements the analysis method developed in section 2.2 to analytically evaluate the leads error Δx^{leads} that affect the quantum Hall Kelvin bridge.

```
(*The program saves a .wl file .the containing the data obtained. The file is saved in the same directory of
the schematic and is named "schematicName_data_YearMonthDayHourMinute.wl". It can be recalled with the
command Get[file name] (or << file name). A copy of the notebook is saved in the same directory with the
name of the schematic (.nb).*)
Save[
  FileNameJoin[
    {FileNameDrop[file], FileBaseName[file] <> "_data_" <> DateString[{"Year", "Month", "Day", "T", "Hour", "Minute"}] <> ".wl"}],
    "Global`";
  NotebookSave[EvaluationNotebook[],
    FileNameJoin[{FileNameDrop[file], FileBaseName[file] <> DateString[{"Year", "Month", "Day", "T", "Hour", "Minute"}] <>
      ".nb"}]];

(*The distribution is plotted as an histogram. It is exported in the same directory of the circuit schematic.*)
MantExpMean = MantissaExponent[meanResult];
MantExpResult = MantissaExponent[result];
ExpMean = MantExpMean[2] - 1;
MantResult = result * 10^(-ExpMean);
h = Labeled[Histogram[MantResult, ChartStyle -> Blue], {StringTemplate["x 10^a ΔR0ab,cd"] [ <|"a" -> -ExpMean|>], "counts"},
  {Bottom, Left}, RotateLabel -> True];
Export[
  FileNameJoin[{FileNameDrop[file], FileBaseName[file] <> DateString[{"Year", "Month", "Day", "T", "Hour", "Minute"}] <>
    "_plot.png"}], h, ImageResolution -> 600];
Print[h, ImageSize -> 180, Background -> Red, BaseStyle -> {14, White, Bold},
  Method -> "Queued"]]
```

Figure A.6: Export of the obtained data as a histogram plot, a data file and a Mathematica notebook.

```
ClearAll[file, n, m, l, A, AT, rQN, a, b, c, d, e, f, s, wp, tList, fileAnnotated, fileLog, rightCirculantMatrix, qheCwIdeal,
  qheCcwIdeal, takeOperator, complementaryIndices, wp, Yi, rnSign, epsilonLim, deltaLim, epsilon, delta, result, D, g,
  Y, Yn, gn, err, τ, mean, standDev, h, qharsLog, δRQList, tPlot, qheType, ra, rDeltaV, rV, rapp];

(*The function below is useful for the following definitions*)
rightCirculantMatrix[L_List?VectorQ] := NestList[RotateRight, RotateRight[L], Length[L] - 1]

(*These operators define the Yi IAM matrices of an ideal QHE element (clockwise and counterclockwise)*)
qheCwIdeal[x_Integer] := rightCirculantMatrix[PadLeft[{-1, 1}, x]] /; x ≥ 2
qheCcwIdeal[x_Integer] := rightCirculantMatrix[Join[{-1}, ConstantArray[0, x - 2], {1}]] /; x ≥ 2

(* The operators below are taken from http://stackoverflow.com/a/5300892/2522705 *)
takeOperator[w_?MatrixQ, rows_List, cols_List] := w[[rows, cols]]
dropOperator[w_?MatrixQ, rows_List, cols_List] := w[[##]] & @@ complementaryIndices[w, rows, cols]
complementaryIndices[w_?MatrixQ, rows_List, cols_List] := Complement[##, Transpose@{Range /@ Dimensions@w, {rows, cols}}]
```

Figure A.7: Initialization of the Mathematica notebook for the quantum Hall Kelvin bridge analysis.

Figure A.10 shows the implementation of the solver in the Mathematica notebook.

The indefinite admittance matrix \bar{Y}^Q of the network is constructed, according to (2.14). The ratio between V_D and V is calculated as

$$\frac{V_D}{V} = \frac{V_{ab}}{V_{ef}} = \frac{V_{ab}/I_{cd}}{V_{ef}/I_{cd}} = \frac{R_{ab,cd}}{R_{ef,cd}}. \tag{A.1}$$

```

Module[{fileNetlist = "",
  qharsSchematic = "",
  qharsList = "",
  qharsNetlist = "",
  qheNodes = {},
  resistorNodes = {},
  qharsNodes = {},
  rows = 0},
Button["Load QHARS Schematic",
  n = 0;
  m = 0;
  l = 0;
  A = {};
  wp = 4 MachinePrecision;
  a = 0;
  b = 0;
  c = 0;
  d = 0;
  e = 0;
  f = 0;
  file = SystemDialogInput["FileOpen", {NotebookDirectory[], {"LTspice schematic" -> {"*.asc"}, "All files" -> {"*.*"}}},
    WindowTitle -> "Choose the QHARS schematic"];
  If[file != $Canceled,
    qharsSchematic = Import[file, "Text"]; (*The program imports the QHARS schematic.*)
    (*The program extracts the parameters c,d (current nodes), a,b (volage nodes of VD) and e,
    f (voltage nodes of V) from the schematic.*)
    ToExpression[StringCases[qharsSchematic, RegularExpression["a\\s*.*+|b\\s*.*+|c\\s*.*+|d\\s*.*+|e\\s*.*+|f\\s*.*."]]];
    (*The program runs LTspice XVIIx64 (in both Windows or Unix OS) and imports the LTspice netlist.*)
    Switch[$OperatingSystem, "Windows", RunProcess[{"XVIIx64.exe", "-netlist", file}], "Unix",
      RunProcess[{"wine", "XVIIx64.exe", "-netlist", TemplateApply["`StandardOutput`", RunProcess[{"winepath", "-w", file}]}] //
        StringTrim]];
    fileNetlist = FileNameJoin[{FileNameDrop[file], FileNameBaseName[file] <> ".net"}];
    qharsNetlist = Import[fileNetlist, "Text"];

```

Figure A.8: First portion of the converter of the application, which imports the electrical LTspice schematic of the bridge.

```
(*The program extracts the list of the QHE element and resistance nodes. The type of the QHE element (CW or CCW)
is also taken into account.*)
qharsList =
SortBy[ToExpression@StringSplit[StringReplace[StringCases[qharsNetlist, StartOfLine ~~ RegularExpression["XU{^n}+\\n"]],
{"qhecw" -> "N0", "qheccw" -> "N1"}], {"XU", Whitespace ~~ "N"}], First][[All, 2 ;;]];
qheType = qharsList[[All, -1]];
qheNodes = qharsList[[All, 1 ;; -2]];
resistorNodes =
SortBy[ToExpression@StringSplit[StringCases[qharsNetlist, StartOfLine ~~ RegularExpression["R{^n}+\\n"]],
{"R", Whitespace ~~ "N"}][[All, 1 ;; -2]], First][[All, 2 ;;]];

n = Dimensions[qheNodes][[1]]; (*The number of QHE elements in the QHARS.*)
m = Dimensions[qheNodes][[2]]; (*The number of the QHE element terminals.*)
l = Dimensions[resistorNodes][[1]]; (*The number of resistances in the QHARS.*)
qharsNodes = Join[qheNodes, resistorNodes]; (*The list of the QHARS nodes.*)
rows = n m + 2 l; (*The number of nodes.*)

(*The program creates the interconnection A matrix.*)
A = ConstantArray[0, {rows, Max[qharsNodes]}];
Table[A[[k]][[Flatten[qharsNodes][[k]]]] = 1, {k, rows}];
```

Figure A.9: Second portion of the converter of the application imports the electrical LTspice schematic of the bridge. The parameters a, b (voltage terminals of V_D), c, d (current terminals), and e, f (voltage terminals of V) are extracted from the comment line of the LTspice schematic, the parameters N, M and L are derived, and the interconnection matrix \mathbf{A} is constructed.

```
Yi = Table[If[qheType[[i]] == 0, qheCwIdeal[m], qheCcwIdeal[m]], {i, n}]; (*The IAM matrix of the N QHE elements.*)
AT = AT'; (*Transpose of the matrix A.*)
rnSign1 = Sign[c - d] Sign[a - b] (-1)^(1 + 1 + c + d + a + b); (*The sign operator is calculated from the parameters a,b,c and d.*)
rnSign2 = Sign[c - d] Sign[e - f] (-1)^(1 + 1 + c + d + e + f); (*The sign operator is calculated from the parameters c,d,e and f.*)

(*The program creates the matrix g that identify the wire resistances.*)
g = Table[{{2 / (delta[i] t), -2 / (delta[i] t)}, {-2 / (delta[i] t), 2 / (delta[i] t)}}, {i, 1, l}];

(*The program creates the IAM Y of the N QHE elements and the wire resistances. This is a block diagonal matrix
and each block represents an element of the QHARS.*)
Y = DiagonalMatrix[Hold /@ Join[Table[Yi[[i]], {i, 1, n}], g]] // ReleaseHold // ArrayFlatten;
Yn = AT.Y.A; (*Calculate the QHARS IAM Yn.*)

(*Evaluate the 4-terminal resistance corresponding to the a,b voltage nodes and c,d current nodes,
and the one corresponding to e,f voltage nodes and c,d current nodes.*)
rDeltaV = rnSign1 Series[Det[dropOperator[Yn, {c, d}, {a, b}]] / Det[dropOperator[Yn, {1}, {1}], {t, 0, 2}];
rDeltaVs = Normal[rDeltaV] /. {t -> 1};

rV = rnSign2 Series[Det[dropOperator[Yn, {c, d}, {e, f}]] / Det[dropOperator[Yn, {1}, {1}], {t, 0, 2}];
rVs = Normal[rV] /. {t -> 1};

(*Evaluate the ratio between the two 4-terminal resistances.*)
rapp = Normal[rDeltaV / rV] /. {t -> 1};
], ImageSize -> 180, Background -> Orange, BaseStyle -> {14, Bold, White},
Method -> "Queued"]]
```

Figure A.10: Implementation of the solver in the Mathematica notebook.

Bibliography

- [1] M. Marzano et al. “Error modelling of Quantum Hall array resistance standards”. In: *Metrologia* 55 (2018), pp. 167–174. [DOI].
- [2] A. F. Rigosi et al. “Atypical quantized resistances in millimeter-scale epitaxial graphene p-n junctions”. In: *Carbon* 154 (Dec. 2019), pp. 230–237. [DOI].
- [3] M. Marzano, L. Callegaro, and M. Ortolano. “A quantum Hall effect Kelvin bridge for resistance calibration”. In: *2018 Conference on Precision Electromagnetic Measurements (CPEM 2018)*. ISSN 2160-0171. Paris, France: IEEE, July 2018, pp. 1–2. [DOI].
- [4] M. Marzano et al. “Implementation of a graphene quantum Hall Kelvin bridge-on-a-chip for resistance calibrations”. In: *Metrologia* (2019). in press. [DOI].
- [5] M. Marzano et al. “A 1:1 fully digital bridge for the realization of the farad from the quantum Hall effect”. In: *Metrologia* (2019). in preparation.
- [6] L. Callegaro. *Electrical impedance: principles, measurement, and applications*. Series in Sensors. CRC Press, 2013. ISBN: 9781439849101.
- [7] F. Overney and B. Jeanneret. “Impedance bridges: from Wheatstone to Josephson”. In: *Metrologia* 55 (2018), S119–S134. [DOI]. [URL].
- [8] L. O. Chua, C. A. Desoer, and E. S. Kuh. *Linear and nonlinear circuits*. New York: McGraw-Hill, 1987.
- [9] M. Ortolano and L. Callegaro. “Matrix method analysis of quantum Hall effect device connections”. In: *Metrologia* 49.1 (2012), pp. 1–7. ISSN: 0026-1394. [DOI]. [URL].
- [10] J. Shekel. “Voltage reference node — its transformations in nodal analysis”. In: *Wireless Engineer* 31 (1954), pp. 6–10.
- [11] L. A. Zadeh. “Multipole analysis of active networks”. In: *IRE Transactions on Circuit Theory* 4 (1957), pp. 97–105.
- [12] G. E. Sharpe. “On the solution of networks by means of the equicofactor matrix”. In: *IRE Transactions on Circuit Theory* 7 (1960), pp. 230–239.

- [13] W. Chen. *Active network analysis*. 2nd. Singapore: World Scientific Publishing Co., 2017.
- [14] E. O. Göbel and U. Siegner. *The New International System of Units (SI): Quantum Metrology and Quantum Standards*. Wiley-VCH, 2019. ISBN: 978-3-527-34459-8.
- [15] I. M. Mills et al. “Redefinition of the kilogram: a decision whose time has come”. In: *Metrologia* 42.2 (Mar. 2005), pp. 71–80. [DOI].
- [16] BIPM. *9th SI Brochure*. 2019. [URL].
- [17] J. Fischer and J. Ullrich. “The new system of units”. In: *Nature Physics* 12.1 (Jan. 2016), pp. 4–7. [DOI].
- [18] I. M. Mills et al. “Redefinition of the kilogram, ampere, kelvin and mole: a proposed approach to implementing CIPM recommendation 1 (CI-2005)”. In: *Metrologia* 43.3 (Apr. 2006), pp. 227–246. [DOI]. [URL].
- [19] M. Stock et al. “The revision of the SI—the result of three decades of progress in metrology”. In: *Metrologia* 56.2 (Feb. 2019), p. 022001. [DOI]. [URL].
- [20] BIPM. *Resolution 1 of the 26th CGPM*. 2018. [URL].
- [21] P. J. Mohr et al. “Data and analysis for the CODATA 2017 special fundamental constants adjustment”. In: *Metrologia* 55.1 (Jan. 2018), pp. 125–146. [DOI]. [URL].
- [22] D. B. Newell et al. “The CODATA 2017 values of h , e , k , and N_A for the revision of the SI”. In: *Metrologia* 55.1 (Jan. 2018), pp. L13–L16. [DOI]. [URL].
- [23] K. v. Klitzing, G. Dorda, and M. Pepper. “New Method for High-Accuracy Determination of the Fine-Structure Constant Based on Quantized Hall Resistance”. In: *Phys. Rev. Lett.* 45.6 (Aug. 1980), pp. 494–497. [DOI].
- [24] R. B. Laughlin. “Quantized Hall conductivity in two dimensions”. In: *Phys. Rev. B* 23.10 (May 1981), pp. 5632–5633. [DOI].
- [25] Q. Niu, D. J. Thouless, and Y.-S. Wu. “Quantized Hall conductance as a topological invariant”. In: *Phys. Rev. B* 31.6 (Mar. 1985), pp. 3372–3377. [DOI].
- [26] D. J. Thouless. “Topological interpretations of quantum Hall conductance”. In: *J. Math. Phys.* 35.10 (Oct. 1994), pp. 5362–5372. [DOI].
- [27] F. Schopfer and W. Poirier. “Testing universality of the quantum Hall effect by means of the Wheatstone bridge”. In: *J. Appl. Phys.* 102.5 (Sept. 2007), p. 054903. [DOI].
- [28] F. Schopfer and W. Poirier. “Quantum resistance standard accuracy close to the zero-dissipation state”. In: *J. Appl. Phys.* 114.6 (Aug. 2013), p. 064508. [DOI].

- [29] A. Hartland et al. “Direct comparison of the quantized Hall resistance in gallium arsenide and silicon”. In: *Phys. Rev. Lett.* 66.8 (Feb. 1991), pp. 969–973. [DOI].
- [30] B. Jeckelmann, A. D. Inglis, and B. Jeanneret. “Material, device, and step independence of the quantized Hall resistance”. In: *IEEE Trans. Instrum. Meas.* 44.2 (Apr. 1995), pp. 269–272. [DOI].
- [31] B. Jeckelmann and B. Jeanneret. “The quantum Hall effect as an electrical resistance standard”. In: *Rep. Prog. Phys.* 64.12 (Nov. 2001), pp. 1603–1655. [DOI].
- [32] T. J. B. M. Janssen et al. “Graphene, universality of the quantum Hall effect and redefinition of the SI system”. In: *New J. Phys.* 13.9 (Sept. 2011), p. 093026. [DOI].
- [33] R. Ribeiro-Palau et al. “Quantum Hall resistance standard in graphene devices under relaxed experimental conditions”. In: *Nat. Nanotechnol.* 10.11 (Sept. 2015), pp. 965–971. [DOI].
- [34] B. Jeckelmann, B. Jeanneret, and D. Inglis. “High-precision measurements of the quantized Hall resistance: Experimental conditions for universality”. In: *Phys. Rev. B* 55.19 (May 1997), pp. 13124–13134. [DOI].
- [35] B. Jeckelmann et al. “Optimization of QHE-devices for metrological applications”. In: *IEEE Trans. Instrum. Meas.* 50.2 (2001), pp. 218–222. ISSN: 00189456. [DOI]. [URL].
- [36] F. Delahaye and B. Jeckelmann. “Revised technical guidelines for reliable dc measurements of the quantized Hall resistance”. In: *Metrologia* 40.5 (Sept. 2003), pp. 217–223. [DOI].
- [37] C. W. J. Beenakker and H. van Houten. “Quantum Transport in Semiconductor Nanostructures”. In: *Semiconductor Heterostructures and Nanostructures*. Elsevier, 1991, pp. 1–228. [DOI].
- [38] K. von Klitzing. “A personal view on the discovery. Physics and application of this quantum effect”. In: *Séminaire Poincaré 2: 25 Years of Quantum Hall Effect (QHE)*. 2004, p. 1.
- [39] B. Douçot and V. Pasquier. “Physics in strong magnetic field”. In: *Séminaire Poincaré 2: 25 years of Quantum Hall Effect (QHE)*. 2004, p. 17.
- [40] M. Büttiker and S. E. Nigg. “Role of coherence in resistance quantization”. In: *The European Physical Journal Special Topics* 172.1 (June 2009), pp. 247–255. [DOI].
- [41] M. Janßen et al. *Introduction to the Theory of the Integer Quantum Hall Effect*. Wiley-VCH, 1994. ISBN: 3527292098. [URL].

- [42] S. M. Girvin. “The Quantum Hall Effect: Novel Excitations And Broken Symmetries”. In: *Topological aspects of low dimensional systems*. Springer Berlin Heidelberg, 1999, pp. 53–175. [DOI].
- [43] D. Yoshioka. *The quantum Hall effect*. Springer, 2002. [DOI].
- [44] M. O. Goerbig and P. Lederer. “Lecture Notes: Introduction to the Quantum Hall Effects”. In: (2006). University of Paris. eprint: [arXivpreprintarXiv:0909.1998](https://arxiv.org/abs/0909.1998).
- [45] T. Ihn. *Semiconductor nanostructures*. Oxford University Press, 2010. ISBN: 9780199534425. [DOI].
- [46] D. K. Ferry, S. M. Goodnick, and J. Bird. *Transport in Nanostructures*. Cambridge University Press, 2009. [DOI].
- [47] M. Büttiker. “Absence of backscattering in the quantum Hall effect in multi-probe conductors”. In: *Physical Review B* 38.14 (Nov. 1988), pp. 9375–9389. [DOI].
- [48] G. Nachtwei. “Breakdown of the quantum Hall effect”. In: *Physica E: Low-dimensional Systems and Nanostructures* 4.2 (Apr. 1999), pp. 79–101. [DOI].
- [49] G. Eber et al. “Two-dimensional magneto-quantum transport on GaAs-AlxGa1-xAs heterostructures under non-ohmic conditions”. In: *Journal of Physics C: Solid State Physics* 16.28 (Oct. 1983), pp. 5441–5448. [DOI].
- [50] B. Jeanneret et al. “Influence of the device-width on the accuracy of quantization in the integer quantum Hall effect”. In: *Proceedings of Conference on Precision Electromagnetic Measurements Digest*. IEEE. [DOI].
- [51] J. Schurr, V. Bürkel, and B. P. Kibble. “Realizing the farad from two ac quantum Hall resistances”. In: *Metrologia* 46.6 (2009), pp. 619–628. ISSN: 0026-1394. [DOI]. [URL].
- [52] J. Schurr et al. “The quantum Hall impedance standard”. In: *Metrologia* 48.1 (2011), pp. 47–57. ISSN: 0026-1394. [DOI]. [URL].
- [53] H. Kroemer. “A proposed class of hetero-junction injection lasers”. In: *Proceedings of the IEEE* 51.12 (Dec. 1963), pp. 1782–1783. [DOI].
- [54] A. Y. Cho and J. R. Arthur. “Molecular beam epitaxy”. In: *Prog. Solid State Chem.* 10 (Jan. 1975), pp. 157–191. [DOI].
- [55] R. Dingle et al. “Electron mobilities in modulation-doped semiconductor heterojunction superlattices”. In: *Appl. Phys. Lett.* 33.7 (Oct. 1978), pp. 665–667. [DOI].
- [56] W. Poirier et al. “The ampere and the electrical units in the quantum era”. In: *Comptes Rendus Physique* 20.1 (2019), pp. 92–128. ISSN: 1631-0705. [DOI].

- [57] K. S. Novoselov. “Electric Field Effect in Atomically Thin Carbon Films”. In: *Science* 306.5696 (Oct. 2004), pp. 666–669. [DOI].
- [58] K. S. Novoselov et al. “Two-dimensional gas of massless Dirac fermions in graphene”. In: *Nature* 438.7065 (Nov. 2005), pp. 197–200. [DOI].
- [59] Y. Zhang et al. “Experimental observation of the quantum Hall effect and Berry’s phase in graphene”. In: *Nature* 438.7065 (Nov. 2005), pp. 201–204. [DOI].
- [60] A. H. C. Neto et al. “The electronic properties of graphene”. In: *Rev. Mod. Phys.* 81.1 (Jan. 2009), pp. 109–162. [DOI].
- [61] B. Gharekhanlou and S. Khorasani. “An overview of tight-binding method for two-dimensional carbon structures”. In: *Graphene: Properties, Synthesis & Applications*. Nova Science Publishers Inc, 2011, pp. 1–37. ISBN: 1614709491. [URL].
- [62] T. J. B. M. Janssen et al. “Quantum resistance metrology using graphene”. In: *Rep. Prog. Phys.* 76.10 (Oct. 2013), p. 104501. [DOI].
- [63] J. A. Alexander-Webber et al. “Phase Space for the Breakdown of the Quantum Hall Effect in Epitaxial Graphene”. In: *Phys. Rev. Lett.* 111.9 (Aug. 2013). [DOI].
- [64] K. S. Kim et al. “Large-scale pattern growth of graphene films for stretchable transparent electrodes”. In: *Nature* 457.7230 (Jan. 2009), pp. 706–710. [DOI].
- [65] C. Berger et al. “Ultrathin Epitaxial Graphite: 2D Electron Gas Properties and a Route toward Graphene-based Nanoelectronics”. In: *J. Phys. Chem. B* 108.52 (Dec. 2004), pp. 19912–19916. [DOI].
- [66] M. Kruskopf et al. “Epitaxial graphene on SiC: modification of structural and electron transport properties by substrate pretreatment”. In: *J. Phys.: Condens. Matter* 27.18 (Apr. 2015), p. 185303. [DOI].
- [67] K. V. Emtsev et al. “Interaction, growth, and ordering of epitaxial graphene on SiC{0001} surfaces: A comparative photoelectron spectroscopy study”. In: *Phys. Rev. B* 77.15 (Apr. 2008). [DOI].
- [68] K. V. Emtsev et al. “Towards wafer-size graphene layers by atmospheric pressure graphitization of silicon carbide”. In: *Nat. Mater.* 8.3 (Feb. 2009), pp. 203–207. [DOI].
- [69] M. A. Real et al. “Graphene Epitaxial Growth on SiC(0001) for Resistance Standards”. In: *IEEE Trans. Instrum. Meas.* 62.6 (June 2013), pp. 1454–1460. [DOI].
- [70] T. Schumann et al. “Anisotropic quantum Hall effect in epitaxial graphene on stepped SiC surfaces”. In: *Phys. Rev. B* 85.23 (June 2012). [DOI].

- [71] M. Kruskopf et al. “Comeback of epitaxial graphene for electronics: large-area growth of bilayer-free graphene on SiC”. In: *2D Mater.* 3.4 (Sept. 2016), p. 041002. [\[DOI\]](#).
- [72] S. Lara-Avila et al. “Non-Volatile Photochemical Gating of an Epitaxial Graphene/Polymer Heterostructure”. In: *Adv. Mater.* 23.7 (Jan. 2011), pp. 878–882. [\[DOI\]](#).
- [73] A. Lartsev et al. “Tuning carrier density across Dirac point in epitaxial graphene on SiC by corona discharge”. In: *Appl. Phys. Lett.* 105.6 (Aug. 2014), p. 063106. [\[DOI\]](#).
- [74] A. F. Rigosi et al. “Gateless and reversible Carrier density tunability in epitaxial graphene devices functionalized with chromium tricarbonyl”. In: *Carbon* 142 (Feb. 2019), pp. 468–474. [\[DOI\]](#).
- [75] M. Kruskopf and R. E. Elmquist. “Epitaxial graphene for quantum resistance metrology”. In: *Metrologia* 55.4 (July 2018), R27–R36. [\[DOI\]](#).
- [76] M. Woszczyna et al. “Precision quantization of Hall resistance in transferred graphene”. In: *Appl. Phys. Lett.* 100.16 (Apr. 2012), p. 164106. [\[DOI\]](#).
- [77] T. J. B. M. Janssen et al. “Precision comparison of the quantum Hall effect in graphene and gallium arsenide”. In: *Metrologia* 49.3 (Mar. 2012), pp. 294–306. [\[DOI\]](#).
- [78] R. Ribeiro-Palau et al. “Quantum Hall resistance standard in graphene devices under relaxed experimental conditions”. In: *Nature Nanotech.* 10 (2015), pp. 965–971.
- [79] K. S. Novoselov et al. “Room-Temperature Quantum Hall Effect in Graphene”. In: *Science* 315.5817 (Mar. 2007), pp. 1379–1379. [\[DOI\]](#).
- [80] T. J. B. M. Janssen et al. “Operation of graphene quantum Hall resistance standard in a cryogen-free table-top system”. In: *2D Mater.* 2.3 (Aug. 2015), p. 035015. [\[DOI\]](#).
- [81] A. F. Rigosi et al. “Graphene Devices for Tabletop and High-Current Quantized Hall Resistance Standards”. In: *IEEE Transactions on Instrumentation and Measurement* 68.6 (June 2019), pp. 1870–1878. [\[DOI\]](#).
- [82] T. Cusati et al. “Electrical properties of graphene-metal contacts”. In: *Sci. Rep.* 7.1 (July 2017). [\[DOI\]](#).
- [83] J. Knoch, Z. Chen, and J. Appenzeller. “Properties of Metal-Graphene Contacts”. In: *IEEE Trans. Nanotechnol.* 11.3 (May 2012), pp. 513–519. [\[DOI\]](#).
- [84] T. Chu and Z. Chen. “Understanding the Electrical Impact of Edge Contacts in Few-Layer Graphene”. In: *ACS Nano* 8.4 (Mar. 2014), pp. 3584–3589. [\[DOI\]](#).

- [85] M. Kruskopf et al. “Two-terminal and multi-terminal designs for next-generation quantized Hall resistance standards: contact material and geometry”. In: *IEEE Trans. Electron Devices* 66.9 (Sept. 2019), pp. 3973–3977. [DOI].
- [86] F. Delahaye. “Series and parallel connection of multiterminal quantum Hall effect devices”. In: *J. Appl. Phys.* 73.11 (1993), pp. 7914–7920. ISSN: 0021-8979. [DOI]. [URL].
- [87] W. Poirier et al. “A new generation of QHARS: discussion about the technical criteria for quantization”. In: *Metrologia* 41.4 (2004), p. 285.
- [88] T. Oe et al. “Development of 1 M Ω Quantum Hall Array Resistance Standards”. In: *IEEE Trans. Instrum. Meas.* 66.6 (June 2017), pp. 1475–1481. ISSN: 0018-9456. [DOI].
- [89] A. Lartsev et al. “A prototype of $R_K/200$ quantum Hall array resistance standard on epitaxial graphene”. In: *J. Appl. Phys.* 118 (2015), p. 044506.
- [90] M. Ortolano and L. Callegaro. “Circuit models and SPICE macro-models for quantum Hall effect devices”. In: *Meas. Sci. Technol.* 26.8 (2015), p. 085018. ISSN: 0957-0233. [DOI]. [URL].
- [91] S. Novikov et al. “Mini array of quantum Hall devices based on epitaxial graphene”. In: *J. Appl. Phys.* 119 (2016), p. 174504.
- [92] M. E. Cage, A. Jeffery, and R. E. Elmquist. “Suggested triple-series connection measurement tests of the AC quantized Hall resistance and the AC longitudinal resistance”. In: *1998 Conf. Precis. Electromagn. Meas. (CPEM 1998)*. Washington, DC, USA: IEEE, July 1998, pp. 341–342. ISBN: 0-7803-5018-9. [DOI]. [URL].
- [93] W. Poirier and F. Schopfer. “Resistance metrology based on the quantum Hall effect”. In: *Eur. Phys. J. Spec. Top.* 172 (2009), pp. 207–245. [DOI].
- [94] J. Konemann et al. “Magnetic Field Reversible Serial Quantum Hall Arrays”. In: *IEEE Trans. Instrum. Meas.* 60.7 (2011), pp. 2512–2516.
- [95] J. Könemann et al. “Investigation of Serial Quantum Hall arrays as a Quantum Resistance Standard”. In: *J. Phys. Conf. Ser.* 334 (Dec. 2011), p. 012017. [DOI].
- [96] T. Oe et al. “New Design of Quantized Hall Resistance Array Device”. In: *IEEE Trans. Instrum. Meas.* 62.6 (2013), pp. 1755–1759.
- [97] A. Domae et al. “Experimental Demonstration of Current Dependence Evaluation of Voltage Divider Based on Quantized Hall Resistance Voltage Divider”. In: *IEEE Trans. Instrum. Meas.* 66.6 (June 2017), pp. 1237–1242. [DOI].

- [98] M. Kruskopf et al. “Next-generation crossover-free quantum Hall arrays with superconducting interconnections”. In: *Metrologia* 56.6 (Oct. 2019), p. 065002. [\[DOI\]](#).
- [99] F. Kuchar et al. “Microwave Hall conductivity of the two-dimensional electron gas in GaAs-Al_xGa_{1-x}As”. In: *Phys. Rev. B* 33.4 (Feb. 1986), pp. 2965–2967. [\[DOI\]](#).
- [100] O. Viehweger and K. B. Efetov. “Frequency-dependent deformation of the Hall plateaux”. In: *J. Phys.: Condens. Matter* 3.11 (Mar. 1991), pp. 1675–1678. [\[DOI\]](#).
- [101] F. Delahaye. “Accurate AC measurements of the quantized Hall resistance from 1 Hz to 1,6 kHz”. In: *Metrologia* 31.5 (1995), pp. 367–373. ISSN: 0026-1394. [\[DOI\]](#). [\[URL\]](#).
- [102] B. P. Kibble and J. Schurr. “A novel double-shielding technique for ac quantum Hall measurement”. In: *Metrologia* 45.5 (2008), pp. L25–L27. ISSN: 0026-1394. [\[DOI\]](#). [\[URL\]](#).
- [103] F. J. Ahlers et al. “Compendium for precise ac measurements of the quantum Hall resistance”. In: *Metrologia* 46.5 (2009), R1–R11. ISSN: 0026-1394. [\[DOI\]](#). [\[URL\]](#).
- [104] F. Delahaye. “DC and AC Techniques for Resistance and Impedance Measurements”. In: *Metrologia* 29.2 (Jan. 1992), pp. 81–93. [\[DOI\]](#).
- [105] G. M. Reedtz and M. E. Cage. “An automated potentiometric system for precision measurement of the quantized Hall resistance”. In: *J. Res. NBS* 92.5 (1987), pp. 303–310.
- [106] G. W. Small. “Comparison of quantized Hall resistance with a 2-Ω standard”. In: *IEEE Trans. Instrum. Meas.* 32.3 (Sept. 1983), pp. 446–447. [\[DOI\]](#).
- [107] P. Warnecke et al. “High-precision resistance ratio measurements by means of a novel Josephson potentiometer”. In: *IEEE Trans. Instrum. Meas.* IM-36.2 (June 1987), pp. 249–251. [\[DOI\]](#).
- [108] R. Behr et al. “Measuring resistance standards in terms of the quantized Hall resistance with a dual Josephson voltage standard using sinus Josephson arrays”. In: *IEEE Trans. Instrum. Meas.* 52.2 (Apr. 2003), pp. 521–523. [\[DOI\]](#).
- [109] N. L. Kusters, W. J. M. Moore, and P. N. Miljanic. “A current comparator for the precision measurement of D-C ratios”. In: *IEEE Transactions on Communication and Electronics* 83.70 (Jan. 1964), pp. 22–27. [\[DOI\]](#).
- [110] M. P. MacMartin and N. L. Kusters. “A Direct-Current-Comparator Ratio Bridge for Four-Terminal Resistance Measurements”. In: *IEEE Trans. Instrum. Meas.* 15.4 (1966), pp. 212–220. [\[DOI\]](#).

- [111] A. D. Inglis. “A cheaper, simpler quantized Hall resistance standard”. In: *IEEE Trans. Instrum. Meas.* 48.2 (Apr. 1999), pp. 289–292. [DOI].
- [112] J. Williams. “Cryogenic current comparators and their application to electrical metrology”. In: *IET Science, Measurement & Technology* 5 (6 Nov. 2011), pp. 211–224.
- [113] M. Götz and D. Drung. “Stability and Performance of the Binary Compensation Unit for Cryogenic Current Comparator Bridges”. In: *IEEE Trans. Instrum. Meas.* 66.6 (June 2017), pp. 1467–1474. [DOI].
- [114] S. Awan, B. Kibble, and J. Schurr. *Coaxial electrical circuits for interference-free measurements*. Electrical Measurement Series. The Institution of Engineering and Technology, 2011. ISBN: 9781849190695.
- [115] L. Callegaro. *Electrical impedance: principles, measurement, and applications*. in Sensors. ISBN: 978-1-43-984910-1. Boca Raton, FL, USA: CRC press: Taylor & Francis, 2013.
- [116] R. Cutkosky. “Techniques for comparing four-terminal-pair admittance standards”. In: *J. Res. Natl. Bur. Stand.(US) C* 74 (1970), pp. 63–78.
- [117] A. Jeffery et al. “Determination of the von Klitzing constant and the fine-structure constant through a comparison of the quantized Hall resistance and the ohm derived from the NIST calculable capacitor”. In: *Metrologia* 35.2 (Apr. 1998), pp. 83–96. [DOI].
- [118] L. Palafox et al. “AIM QuTE: Automated Impedance Metrology extending the Quantum Toolbox for Electricity”. In: *16th International Congress of Metrology*. EDP Sciences, 2013. [DOI].
- [119] R. D. Cutkosky. “An Automatic High-Precision Audiofrequency Capacitance Bridge”. In: *IEEE Trans. Instrum. Meas.* IM-34.3 (Sept. 1985), pp. 383–389. [DOI].
- [120] S. P. Giblin and J. M. Williams. “Automation of a Coaxial Bridge for Calibration of AC Resistors”. In: *IEEE Trans. Instrum. Meas.* 56.2 (Apr. 2007), pp. 373–377. [DOI].
- [121] A. C. Corney. “A Universal Four-Pair Impedance Bridge”. In: *IEEE Trans. Instrum. Meas.* 28.3 (1979), pp. 211–215. [DOI].
- [122] A. C. Corney. “Digital generator assisted impedance bridge”. In: *IEEE Trans. Instrum. Meas.* 52 (2003), pp. 388–391. [DOI]. [URL].
- [123] K. Musioł, A. Met, and T. Skubis. “Automatic bridge for comparison of inductance standards”. In: *Measurement* 43.10 (Dec. 2010), pp. 1661–1667. [DOI].
- [124] M. Surdu et al. “An automatic bridge for the comparison of the impedance standards”. In: *Measurement* 46.9 (Nov. 2013), pp. 3701–3707. [DOI].

- [125] L. Callegaro, V. D’Elia, and B. Trinchera. “Realization of the farad from the dc quantum Hall effect with digitally assisted impedance bridges”. In: *Metrologia* 47 (2010), pp. 464–472.
- [126] B. Trinchera, V. D’Elia, and L. Callegaro. “A digitally assisted current comparator bridge for impedance scaling at audio frequencies”. In: *IEEE Trans. Instrum. Meas.* 62 (2013), pp. 1771–1775. [DOI]. [URL].
- [127] F. Overney, F. Luond, and B. Jeanneret. “Digitally assisted coaxial bridge for automatic quantum Hall effect measurements at audio frequencies”. In: *2014 Conf. Precis. Electromagn. Meas. (CPEM 2014)*. Rio de Janeiro, Brazil: IEEE, Aug. 2014, pp. 226–227. ISBN: 978-1-4799-2479-0. [DOI]. [URL].
- [128] L. Callegaro et al. “Self-compensating networks for four terminal-pair impedance definition in current comparator bridges”. In: *2015 IEEE Int. Instrum. Meas. Technol. Conf. Proc.* Vol. 2015-July. Pisa, Italy, May 2015, pp. 1658–1661. ISBN: 978-1-4799-6114-6. [DOI]. [URL].
- [129] F. Overney, F. Lüönd, and B. Jeanneret. “Broadband fully automated digitally assisted coaxial bridge for high accuracy impedance ratio measurements”. In: *Metrologia* 53 (2016), pp. 918–926. [DOI]. [URL].
- [130] J. Kučera and J. Kováč. “A reconfigurable four terminal-pair digitally assisted and fully digital impedance ratio bridge”. In: *2017 IEEE Int. Instrum. Meas. Technol. Conf.* Turin, Italy, May 2017, pp. 1–6. ISBN: 978-1-5090-3596-0. [DOI]. [URL].
- [131] L. Callegaro. “On strategies for automatic bridge balancing”. In: *IEEE Trans. Instrum. Meas.* 54 (2005), pp. 529–532. [DOI]. [URL].
- [132] S. Bauer et al. “A novel two-terminal-pair pulse-driven Josephson impedance bridge linking a 10 nF capacitance standard to the quantized Hall resistance”. In: *Metrologia* 54.2 (2017), pp. 152–160. ISSN: 0026-1394. [DOI]. [URL].
- [133] F. Overney et al. “Josephson-based full digital bridge for high-accuracy impedance comparisons”. In: *Metrologia* 53 (2016), pp. 1045–1053. [DOI]. [URL].
- [134] F. Overney et al. “Characterization of a Dual Josephson Impedance Bridge”. In: *2018 Conference on Precision Electromagnetic Measurements (CPEM 2018)*. IEEE, July 2018. [DOI].
- [135] L. Callegaro et al. “Experiences with a two-terminal-pair digital impedance bridge”. In: *IEEE Trans. Instrum. Meas.* 64 (2015), pp. 1460–1465. [DOI]. [URL].
- [136] M. Dutta, A. Rakshit, and S. N. Bhattacharyya. “Development and study of an automatic AC bridge for impedance measurement”. In: *IEEE Trans. Instrum. Meas.* 50 (2001), pp. 1048–1052. [DOI]. [URL].

- [137] W. Helbach, P. Marczinowski, and G. Trenkler. “High-Precision Automatic Digital AC Bridge”. In: *IEEE Trans. Instrum. Meas.* 32.1 (Mar. 1983), pp. 159–162. [DOI].
- [138] A. Muciek. “Digital impedance bridge based on a two-phase generator”. In: *IEEE Trans. Instrum. Meas.* 46 (1997), pp. 467–470. [DOI]. [URL].
- [139] M. Kampik et al. “On the need for development of the highly stable source of digitally synthesized AC voltage with increased bandwidth for metrology and diagnostic applications”. In: *2016 Conference on Diagnostics in Electrical Engineering (Diagnostika)*. IEEE, Sept. 2016. [DOI].
- [140] J. Lan et al. “A digital compensation bridge for R - C comparisons”. In: *Metrologia* 49 (2012), p. 266. [DOI]. [URL].
- [141] G. Ramm. “Impedance Measuring Device Based on an AC Potentiometer”. In: *IEEE Trans. Instrum. Meas.* IM-34.2 (June 1985), pp. 341–344. [DOI].
- [142] F. Cabiati and G. C. Bosco. “ LC comparison system based on a two-phase generator”. In: *IEEE Trans. Instrum. Meas.* IM-34 (1985), pp. 344–349. [DOI]. [URL].
- [143] R. Sedlacek and J. Bohacek. “Bridges for calibrating four-terminal-pair standards of self-inductance at frequencies up to 10 kHz”. In: *Meas. Sci. Technol.* 20.2 (Dec. 2008), p. 025105. [DOI].
- [144] B. Trinchera, L. Callegaro, and V. D’Elia. “Quadrature Bridge for R - C Comparisons Based on Polyphase Digital Synthesis”. In: *IEEE Trans. Instrum. Meas.* 58 (2009), pp. 202–206. [DOI]. [URL].
- [145] L. Callegaro and V. D’Elia. “Automated system for inductance realization traceable to AC resistance with a three-voltmeter method”. In: *IEEE Trans. Instrum. Meas.* 50.6 (2001), pp. 1630–1633. [DOI].
- [146] L. Callegaro, G. Galzerano, and C. Svelto. “A multiphase direct-digital-synthesis sinewave generator for high-accuracy impedance comparison”. In: *IEEE Trans. Instrum. Meas.* 50.4 (2001), pp. 926–929. [DOI].
- [147] L. Callegaro. “Like and unlike impedance comparisons with the same instrument”. In: *XVII IMEKO World Congress: Metrology in the 3rd Millennium Proceedings*. 2003, pp. 757–759.
- [148] L. Callegaro, G. Galzerano, and C. Svelto. “Precision impedance measurements by the three-voltage method with a novel high-stability multiphase DDS generator”. In: *IEEE Trans. Instrum. Meas.* 52.4 (Aug. 2003), pp. 1195–1199. [DOI].
- [149] J. Bohacek and R. Sedlacek. “Calibration of Inductance Standards”. In: *2004 Conference on Precision Electromagnetic Measurements*. IEEE, June 2004. [DOI].

- [150] A. Muciek and F. Cabiati. “Analysis of a three-voltmeter measurement method designed for low-frequency impedance comparisons”. In: 2006.
- [151] R. Rybski, J. Kaczmarek, and K. Kontorski. “Impedance comparison using unbalanced bridge with digital sine wave voltage sources”. In: *IEEE Trans. Instrum. Meas.* 64 (2015), pp. 3380–3386. [DOI]. [URL].
- [152] A. Zekry et al. “Four Voltmeter Vector Impedance Meter Based on Virtual Instrumentation”. In: *MAPAN* 31.3 (Apr. 2016), pp. 159–167. [DOI].
- [153] V. Simovic, T. Alajbeg, and J. Curkovic. “Theoretical and practical challenges of using three ammeter or tree voltmeter methods in teaching”. In: *2017 40th International Convention on Information and Communication Technology, Electronics and Microelectronics (MIPRO)*. IEEE, May 2017. [DOI].
- [154] B. C. Waltrip and N. M. Oldham. “Digital impedance bridge”. In: *IEEE Trans. Instrum. Meas.* 44 (1995), pp. 436–439. [DOI]. [URL].
- [155] G. Ramm and H. Moser. “New Multifrequency Method for the Determination of the Dissipation Factor of Capacitors and of the Time Constant of Resistors”. In: *IEEE Trans. Instrum. Meas.* 54.2 (Apr. 2005), pp. 521–524. [DOI].
- [156] G. Ramm and H. Moser. “From the calculable AC resistor to capacitor dissipation factor determination on the basis of time constants”. In: *IEEE Trans. Instrum. Meas.* 50.2 (Apr. 2001), pp. 286–289. [DOI].
- [157] F. Overney and B. Jeanneret. “Realization of an inductance scale traceable to the quantum Hall effect using an automated synchronous sampling system”. In: *Metrologia* 47 (2010), pp. 690–698. [DOI]. [URL].
- [158] F. Overney and B. Jeanneret. “*RLC* bridge based on an automated synchronous sampling system”. In: *IEEE Trans. Instrum. Meas.* 60 (2011), pp. 2393–2398. [DOI]. [URL].
- [159] H. E. van den Brom, E. F. Dierikx, and L. Jo. “Sampling ratio bridge for impedance measurements down to 1 m Ω ”. In: *2012 Conf. Precis. Electromagn. Meas. (CPEM 2012)*. Washington, DC, USA, July 2012, pp. 588–589. ISBN: 978-1-4673-0442-9. [DOI]. [URL].
- [160] R. Rybski, J. Kaczmarek, and M. Koziol. “A PXI-based calibration system for low-value AC resistors”. In: *IEEE Trans. Instrum. Meas.* 67 (2018), pp. 905–911. [DOI]. [URL].
- [161] E. Houtzager, H. E. van den Brom, and E. Dierikx. “Development of a wide-range sampling impedance ratio bridge”. In: *2014 Conf. Precis. Electromagn. Meas. (CPEM 2014)*. Rio de Janeiro, Brazil, Aug. 2014, pp. 230–231. ISBN: 978-1-4799-2479-0. [DOI]. [URL].

- [162] W. G. Kürten Ihlenfeld and R. T. B. Vasconcellos. “A digital four terminal-pair impedance bridge”. In: *2016 Conf. Precis. Electromagn. Meas. (CPEM 2016)*. Ottawa, Canada, July 2016, pp. 1–2. ISBN: 978-1-4673-9134-4. [DOI]. [URL].
- [163] W. G. Kürten Ihlenfeld and R. T. de Barros e Vasconcellos. “A digital five-terminal impedance bridge”. In: *IEEE Trans. Instrum. Meas.* 66 (2017), pp. 1546–1552. [DOI]. [URL].
- [164] S. Mašláň et al. “Digital sampling setup for measurement of complex voltage ratio”. In: *IEEE Trans. Instrum. Meas.* 66 (2017), pp. 1355–1363. [DOI]. [URL].
- [165] R. Rybski, J. Kaczmarek, and M. Koziol. “A High-Resolution PXI Digitizer for a Low-Value-Resistor Calibration System”. In: *IEEE Trans. Instrum. Meas.* 62.6 (June 2013), pp. 1783–1788. [DOI].
- [166] D. DongXue et al. “Improvement of High-Value Capacitance Measurement”. In: *IEEE Trans. Instrum. Meas.* 62.6 (June 2013), pp. 1795–1800. [DOI].
- [167] Y. Nakamura et al. “A multifrequency quadrature bridge for realization of the capacitance standard at ETL”. In: *IEEE Trans. Instrum. Meas.* 48.2 (Apr. 1999), pp. 351–355. [DOI].
- [168] J. C. Hsu and Y.-s. Ku. “Comparison of capacitance with resistance by IVD-based quadrature bridge at frequencies from 50 Hz to 10 kHz”. In: *Conference on Precision Electromagnetic Measurements. Conference Digest. CPEM 2000 (Cat. No.00CH37031)*. IEEE, 2000. [DOI].
- [169] J. Bohacek. “A multifrequency quadrature bridge”. In: *IMTC 2001. Proceedings of the 18th IEEE Instrumentation and Measurement Technology Conference. Rediscovering Measurement in the Age of Informatics (Cat. No.01CH 37188)*. IEEE, 2001. [DOI].
- [170] G. W. Small, J. R. Fiander, and P. C. Coogan. “A bridge for the comparison of resistance with capacitance at frequencies from 200 Hz to 2 kHz”. In: *Metrologia* 38.4 (Aug. 2001), pp. 363–368. [DOI].
- [171] J. Melcher et al. “The european acqhe project: modular system for the calibration of capacitance standards based on the quantum hall effect”. In: *IEEE Trans. Instrum. Meas.* 52.2 (Apr. 2003), pp. 563–568. [DOI].
- [172] S. A. Awan, R. G. Jones, and B. P. Kibble. “Evaluation of coaxial bridge systems for accurate determination of the SI Farad from the DC quantum Hall effect”. In: *Metrologia* 40.5 (Sept. 2003), pp. 264–270. [DOI].
- [173] A. D. Inglis et al. “Direct determination of capacitance standards using a quadrature bridge and a pair of quantized hall resistors”. In: *IEEE Trans. Instrum. Meas.* 52.2 (Apr. 2003), pp. 559–562. [DOI].

- [174] F. Delahaye and R. Goebel. “Evaluation of the Frequency Dependence of the Resistance and Capacitance Standards in the BIPM Quadrature Bridge”. In: *IEEE Trans. Instrum. Meas.* 54.2 (Apr. 2005), pp. 533–537. [DOI].
- [175] D. L. H. Gibbings. “A design for resistors of calculable a.c./d.c. resistance ratio”. In: *Proc. Inst. Electr. Eng.* 110.2 (1963), p. 335. [DOI].
- [176] F. Overney et al. “The quantized Hall resistance: towards a primary standard of impedance”. In: *Metrologia* 43.5 (2006), pp. 409–413. ISSN: 0026-1394. [DOI]. [URL].
- [177] J. Schurr et al. “The ac quantum Hall effect as a primary standard of impedance”. In: *Metrologia* 44.1 (2007), pp. 15–23. ISSN: 0026-1394. [DOI]. [URL].
- [178] J. Schurr et al. “The ac quantum Hall effect: About gates and image charges”. In: *2008 Conf. Precis. Electromagn. Meas. (CPEM 2008)*. Broomfield, CO, USA: IEEE, June 2008, pp. 328–329. ISBN: 978-1-4244-2399-6. [DOI]. [URL].
- [179] J. Lee et al. “The Josephson two-terminal-pair impedance bridge”. In: *Metrologia* 47.4 (June 2010), pp. 453–459. [DOI].
- [180] L. Palafox et al. “First metrological applications of the PTB 1 V Josephson arbitrary waveform synthesizer”. In: *2016 Conference on Precision Electromagnetic Measurements (CPEM 2016)*. IEEE, July 2016. [DOI].
- [181] A. Jeffery, R. E. Elmquist, and M. E. Cage. “Precision tests of a quantum Hall effect device DC equivalent circuit using double-series and triple-series connections”. In: *J. Res. Natl. Inst. Stand. Technol.* 100 (1995), pp. 677–685.
- [182] B. W. Ricketts and P. C. Kemeny. “Quantum Hall effect devices as circuit elements”. In: *J. Phys. D: Appl. Phys.* 21.3 (1988), p. 483.
- [183] J. Schurr et al. “AC longitudinal and contact resistance measurements of quantum Hall devices”. In: *Metrologia* 43.1 (2006), pp. 163–173. ISSN: 0026-1394. [DOI]. [URL].
- [184] A. Sosso and P. P. Capra. “Electronic simulation of a multiterminal quantum Hall effect device”. In: *Rev. Sci. Instrum.* 70.4 (1999), pp. 2082–2086. [DOI]. [URL].
- [185] M. Ortolano and L. Callegaro. “Circuit models and SPICE macro-models for quantum Hall effect devices”. In: *Meas. Sci. Technol.* 26 (2015), p. 085018.
- [186] L. O. Chua. “Device modeling via basic nonlinear circuit elements”. In: *IEEE Tran. Circuits Syst.* 27 (1980), pp. 1014–1044.
- [187] J. C. Willems. “Terminals and ports”. In: *IEEE Circuits Syst. Mag.* 10 (2010), pp. 8–16.
- [188] V. Belevitch. *Classical network theory*. San Francisco, CA, USA: Holden-Day, 1968.

- [189] W. K. Chen. *Active network analysis*. Singapore: World Scientific Publishing Co., 1991.
- [190] Wolfram. *Mathematica 11*. [URL].
- [191] INRIM. *INRIMQuantumElectricalMetrology*. [URL].
- [192] Linear Technology. *LTspice XVII*. [URL].
- [193] *JCGM 101:2008, Evaluation of measurement data — Supplement 1 to the "Guide to the expression of uncertainty in measurement" – Propagation of distributions using a Monte Carlo method*. 2011. [URL].
- [194] T. Oe et al. "Development of 1 M Ω Quantum Hall Array Resistance Standards". In: *2016 Conference on Precision Electromagnetic Measurements (CPEM 2016)*. Ottawa, Canada, Oct. 2016, pp. 1–2.
- [195] M. Ortolano and L. Callegaro. "Update: On the synthesis of quantum Hall array resistance standards (2015 *Metrologia* **52** 31)". In: *Metrologia* 56.2 (Mar. 2019), p. 022101. [DOI].
- [196] D. Dominguez, K. von Klitzing, and K. Ploog. "Optimization of the Contact Geometry for Accurate Quantized Hall Resistance Measurements". In: *Metrologia* 26 (1989), pp. 197–201.
- [197] R. A. Matula. "Electrical resistivity of copper, gold, palladium, and silver". In: *J. Phys. Chem. Ref. Data* 8.4 (1979), pp. 1147–1298.
- [198] A. B. Pippard. *Magnetoresistance in metals*. Cambridge University Press, 1989.
- [199] J. E. Huffman, M. L. Snodgrass, and F. J. Blatt. "Magnetoresistance of copper, gold, and indium". In: *Phys. Rev. B* 23 (1981), pp. 483–488.
- [200] R. G. Chambers. "Magneto-Resistance Effects in the Group I Metals at High Fields". In: *Proc. Royal Soc. A* 238 (1957), pp. 344–357.
- [201] D.-H. Chae et al. "Direct comparison of 1 M Ω quantized Hall array resistance and quantum Hall resistance standard". In: *Metrologia* 55 (2018), p. 645. [DOI].
- [202] *The SPICE page*. Online. [URL].
- [203] M. B. Steer. *SPICE: User's guide and reference*. Online. 2007. [URL].
- [204] A. Hartland et al. "AC measurements of the quantized Hall resistance". In: *IEEE Trans. Instrum. Meas.* 44.2 (1995), pp. 245–248. ISSN: 00189456. [DOI]. [URL].
- [205] S. W. Chua, B. P. Kibble, and A. Hartland. "Comparison of capacitance with AC quantized Hall resistance". In: *IEEE Trans. Instrum. Meas.* 48.2 (1999), pp. 342–345. ISSN: 00189456. [DOI]. [URL].

- [206] A. Sosso. “Derivation of an electronic equivalent of QHE devices”. In: *IEEE Trans. Instrum. Meas.* 50.2 (Apr. 2001), pp. 223–226.
- [207] J. Schurr, F. Ahlers, and K. Pierz. “Magnetocapacitance and loss factor of GaAs quantum Hall effect devices”. In: *Metrologia* 51 (2014), pp. 235–242.
- [208] C. McAndrew et al. “Correlated Noise Modeling and Simulation”. In: *Technical Proceedings of the 2005 Workshop on Compact Modeling*. Anaheim, CA, US, 2005, pp. 40–45.
- [209] M. H. Rashid and H. M. Rashid. *SPICE for Power Electronics and Electric Power*. 2nd. Boca Raton, FL, USA: CRC Press, 2006.
- [210] A. R. Panna et al. “Uncertainty of the Ohm Using Cryogenic and Non-Cryogenic Bridges”. In: *2018 Conference on Precision Electromagnetic Measurements (CPEM 2018)*. Paris, France, July 2018, pp. 1–2.
- [211] F. P. M. Piquemal et al. “A first attempt to realize (multiple-QHE devices)-series array resistance standards”. In: *IEEE Trans. Instrum. Meas.* 48.2 (1999), pp. 296–300.
- [212] A. Domae et al. “Development of a one-chip quantized Hall resistance voltage divider”. In: *Meas. Sci. Technol.* 23.12 (2012), p. 124008.
- [213] V. Panchal et al. “Confocal laser scanning microscopy for rapid optical characterization of graphene”. In: *Communications Physics* 1.1 (Nov. 2018). [\[DOI\]](#).
- [214] Y. Yang et al. “Epitaxial graphene homogeneity and quantum Hall effect in millimeter-scale devices”. In: *Carbon* 115 (May 2017), pp. 229–236. [\[DOI\]](#).
- [215] C. M. Sutton and M. T. Clarkson. “A general approach to comparisons in the presence of drift”. In: *Metrologia* 30 (1994), pp. 487–493. [\[DOI\]](#).
- [216] H. E. Swanson and S. Schlamming. “Removal of zero-point drift from AB data and the statistical cost”. In: *Meas. Sci. Technol.* 21 (2010), p. 115104. [\[DOI\]](#).
- [217] J. A. Barnes et al. “Characterization of frequency stability”. In: *IEEE Trans. Instrum. Meas.* IM-20 (1971), pp. 105–120. [\[DOI\]](#).
- [218] A. Millea and P. Ilie. “A Class of Double-Balance Quadrature Bridges for the Intercomparison of Three-Terminal Resistance, Inductance and Capacitance Standards”. In: *Metrologia* 5.1 (1969), pp. 14–20.
- [219] S. W. Chua, B. P. Kibble, and A. Hartland. “Comparison of capacitance with AC quantized Hall resistance”. In: *IEEE Trans. Instrum. Meas.* 48.2 (Apr. 1999), pp. 342–345.
- [220] PTB et al. *Modular System for the Calibration of Capacitance Standards Based on the Quantum Hall Effect. Documentation and Operating Manual*. Eur. Project SMT4–CT98–2231 Final Rep. 2001.

- [221] G. Ramm and H. Moser. “Calibration of electronic capacitance and dissipation factor bridges”. In: *IEEE Trans. Instrum. Meas.* 52 (2003), pp. 396–399. [DOI]. [URL].
- [222] J. Kučera and J. Kováč. “A reconfigurable four terminal-pair digitally assisted and fully digital impedance ratio bridge”. In: *IEEE Trans. Instrum. Meas.* 67 (2018), pp. 1199–1206. [DOI]. [URL].
- [223] P. Gournay et al. “Comparison CCEM-K4.2017 of 10 pF and 100 pF capacitance standards”. In: *Metrologia* 56.1A (Nov. 2018), pp. 01001–01001.
- [224] M. Koziół, J. Kaczmarek, and R. Rybski. “Characterization of PXI-based generators for impedance measurement setups”. In: *2018 Conf. Precis. Electromagn. Meas. (CPEM 2018)*. Paris, France, July 2018, pp. 1–2. ISBN: 978-1-5386-0974-3. [DOI]. [URL].
- [225] M. Ortolano et al. “Error analysis of fully-digital impedance bridges”. In: (). In preparation.
- [226] M. Ortolano et al. “An international comparison of phase angle standards between the novel impedance bridges of CMI, INRIM and METAS”. In: *Metrologia* 55 (2018), pp. 499–512. [DOI]. [URL].
- [227] J. Kaczmarek, R. Rybski, and M. Koziół. “The polyphase ac voltage source for digital impedance bridges”. In: *Final dissemination workshop of EMRP projects AIM QuTE, GraphOhm and Q-WAVE*. Prague, May 2016. [URL].
- [228] M. Kampik et al. “Comparison of two buffers for impedance metrology”. In: *Meas. Autom. Monit.* 61 (2015), pp. 127–131.
- [229] METAS. *METAS UncLib*. [URL].
- [230] Kambič. *Air bath TK-190 US data sheet*.
- [231] I. Labs. *1404 Series Primary Standard Capacitor Datasheet*.

This Ph.D. thesis has been typeset by means of the T_EX-system facilities. The typesetting engine was pdfL^AT_EX. The document class was `toptesi`, by Claudio Beccari, with option `tipotesi=scudo`. This class is available in every up-to-date and complete T_EX-system installation.